

Abstract

Improving the Quality of Heisenberg Back-Action of Qubit Measurements made with Parametric Amplifiers

Katrina Sliwa

2016

The quantum back-action of the measurement apparatus arising from the Heisenberg uncertainty principle is both a fascinating phenomenon and a powerful way to apply operations on quantum systems. Unfortunately, there are other effects which may overwhelm the Heisenberg back-action. This thesis focuses on two effects arising in the dispersive measurement of superconducting qubits made with two ultra-low-noise parametric amplifiers, the Josephson bifurcation amplifier (JBA) and the Josephson parametric converter (JPC). The first effect is qubit dephasing due to excess photons in the cavity coming from rogue radiation emitted by the first amplifier stage toward the system under study. This problem arises primarily in measurements made with the JBA, where a strong resonant pump tone is traditionally used to provide the energy for amplification. Replacing the single strong pump tone with two detuned pump tones minimized this dephasing to the point where the Heisenberg back-action of measurements made with the JBA could be observed.

The second effect is reduced measurement efficiency arising from losses between the qubit and the parametric amplifier. Most commonly used parametric amplifiers operate in reflection, requiring additional lossy, magnetic elements known as circulators both to separate input from output, and to protect the qubits from dephasing due to the amplified reflected signal. This work presents two alternative directional elements, the Josephson circulator, which is both theoretically loss-less and does not rely upon the strong magnetic fields needed for traditional circulators, and the Josephson directional amplifier which does not send any amplified signal back toward the qubit. Both of these elements achieve directionality by interfering multiple parametric processes inside a single JPC, allowing for in-situ switching between the two modes of operation. This brings valuable experimental flexibility, and also makes these devices strong candidates for ‘on-chip’ integration, which

would in turn eliminate loss between the qubit and parametric amplifier as a dominant source of reduced measurement efficiency.

Improving the Quality of Heisenberg Back-Action
of Qubit Measurements made with Parametric
Amplifiers

A Dissertation
Presented to the Faculty of the Graduate School
of
Yale University
in Candidacy for the Degree of
Doctor of Philosophy

by
Katrina Sliwa

Dissertation Director: Michel Devoret

May, 2016

Copyright © 2016 by Katrina Sliwa
All rights reserved.

Contents

Acknowledgments	vi
List of Figures	vii
List of Symbols	x
List of Acronyms	xviii
Glossary	xx
1 Introduction	1
1.1 Back-Action in Quantum and Classical Systems	1
1.2 Superconducting Qubits	6
1.2.1 Amplification of Quantum Signals	9
1.3 Double-Pumping the JBA	15
1.4 Quantum Operations	18
1.5 The Josephson Circulator	22
1.6 The Josephson Directional Amplifier	25
1.7 Perspectives	29
2 Coherent Amplification and Conversion with Josephson Parametric De-	
vices	30
2.1 Classification of Parametric Devices	31
2.1.1 Non-Degenerate vs Degenerate	31
2.1.2 Phase-sensitive vs Phase-preserving	32
2.1.3 Reflection vs Through Amplifier	37
2.2 Four-Wave vs Three-Wave Mixing	38

2.2.1	Four-Wave Mixing	38
2.2.2	Three-Wave Mixing	41
2.3	Parametric Amplification with the JBA	45
2.4	Parametric Amplification and Coherent Conversion with the JPC	48
3	Double Pumping the JBA	55
3.1	Derivation of Double-Pumped Gain	55
3.2	Pump Stiffness in the JBA	59
3.2.1	Pump Dynamics in the Single-Pumped JBA	59
3.2.2	Pump Dynamics in the Double-Pumped JBA	61
3.3	Experimental Characterization	62
3.3.1	Device Description	62
3.3.2	Biasing Protocol	64
3.4	Comparison Between Single and Double-Pumping Amplifier Characteristics	66
3.4.1	Gain	66
3.4.2	Added Noise	67
3.4.3	Saturation Power	68
3.5	Comparison of Qubit Dephasing with the Single and Double-Pumped JBA .	70
4	Quantum Operations with Parametric Amplifiers	76
4.1	Heisenberg Back-Action of Phase-Sensitive Amplification Along the I Quadra- ture	77
4.2	Heisenberg Back-Action of Phase-Sensitive Amplification Along the Q Quadra- ture	80
4.3	Heisenberg Back-Action of Phase-Preserving Amplification	83
4.4	Measurement of the Heisenberg Back-Action	85
4.4.1	Experimental Setup	85
4.4.2	Results of Measurement of Phase-Sensitive Back-Action	89
4.4.3	Results of Measurement of Phase-Preserving Back-Action	91
4.5	Characterizing Measurement Efficiency by the Measurement of Heisenberg Back-Action	93

5	Josephson Circulator	97
5.1	Microwave Circulators	97
5.2	Non-Reciprocity with the JPC	98
5.3	Experimental implementation	105
6	Josephson Directional Amplifier	113
6.1	Overview of Low-Noise Directional Parametric Amplifiers	113
6.2	Derivation of Gain in the JDA	115
6.2.1	Effects of Mismatched Parametric Processes	118
6.3	Experimental Implementation and Characterization	120
6.3.1	Added Noise	123
6.3.2	Performance vs Conversion Coefficient	124
7	Conclusions and Perspectives	126

Acknowledgments

This work would not have been possible without the help and support of several people. First and foremost I would like to thank my advisor Michel Devoret both for the chance to work in his group, and for all that he has taught me. He was always willing to discuss everything from physics, to the etymology of language, to the importance of whitespace. No student could ask for a better mentor or role model. I would also like to thank my committee members, Luigi Frunzio, Dan Prober, Doug Stone and Robert Schoelkopf for all of the help and support over the years, and for being willing to read my thesis.

In addition to those mentioned above I would like to thank everyone I have worked with on the fourth floor. It is an amazing place with an amazing group of people. In particular I would like to thank Michael Hatridge and Shyam Shankar, who taught me a lot of what I know about conducting experiments, and who were always willing to answer silly questions or push me in the right direction. I would also like to thank Chad Rigetti, Baleegh Abdo, Flavius Schackert, Anirudh Narla, Ananda Roy, Archanal Kamal, Laszlo Szocs, Evan Zalys-Geller, and Nicholas Frattini, all of whom I have worked closely with on various parametric amplifier projects.

Lastly I would like to thank my family and all of the great friends I have met here at Yale. Without their love and support none of this would have been possible. I would particularly like to thank Brad Hayes, Taylor Brown, Danielle Krasner, Dan Winograd-Cort, Pam Corcoran and Shu-Chun Weng for introducing me to many new things and making my time here more fun than I ever could have imagined.

List of Figures

1.1	Different Types of Measurement Back-Action	4
1.2	Entanglement via Heisenberg Back-Action	5
1.3	Cavity QED Schematic with Fresnell lollipops	8
1.4	Cavity QED Measurement with a HEMT	10
1.5	Cavity QED Measurement with a Parametric Amplifier	11
1.6	Schematic and Photograph of the JPC	12
1.7	Cavity QED Measurement with a JPC	13
1.8	Schematic and SEM Image of the JBA	14
1.9	Cavity QED Measurement with a JBA	14
1.10	Frequency Landscape of a Single and Double-Pumped JBA	16
1.11	Measured Single and Double-Pumped JBA Gain Responses	17
1.12	Ramsey Dephasing Time with a Single-Pumped JBA	17
1.13	Ramsey Dephasing Time with a Double-Pumped JBA	17
1.14	Logical Schematic of a Quantum Operation on a Qubit	18
1.15	Schematic of the Heisenberg Back-Action of the DP-JBA	20
1.16	Measured Heisenberg Back-Action of the DP-JBA	21
1.17	Photograph of a Pamtech Commercial Circulator	22
1.18	Unity Photon Gain Conversion in the JPC	23
1.19	Pump Configuration and Graphical Scattering Matrix for the Josephson Circulator	24
1.20	Measured Josephson Circulator Scattering Parameters	25
1.21	Schematic of the use of an On-Chip Directional Amplifier	26

1.22 Schematic of Pump Configuration and Graphical Scattering Matrix for the Josephson Directional Amplifier	28
1.23 Measured Scattering Parameters for the Josephson Directional Amplifier	28
2.1 Degenerate and Non-Degenerate Parametric Amplifiers	32
2.2 Fresnel Plane Before and After Ideal Phase-Sensitive Amplification	36
2.3 Fresnel Plane Before and After Ideal Phase-Preserving Amplification	37
2.4 Schematic of the JBA	46
2.5 Measured Reflection Gain from the JBA	47
2.6 Schematic of the JRM	49
2.7 Normal Modes of the JRM	49
2.8 Schematic of the JPC	51
2.9 Measured Reflection Gain and Trans-Gain Curves from the JPC	52
2.10 Measured Conversion Curves from the JPC	53
2.11 SEM Image of the JRM and Optical Image of the Full JPC	54
3.1 Frequency Landscape of a Single and Double-Pumped JBA (Reproduced from 1.10)	58
3.2 Experimental Setup for DP-JBA Characterization	63
3.3 Measured 2D Gain Plot for the DP-JBA	65
3.4 Measured DP-JBA Gain Curves for Multiple Effective Pump Powers	66
3.5 Measured Single and Double-Pumped 20 dB Gain Curves	67
3.6 Measured NVR for the Single and Double-Pumped JBA	68
3.7 Measured Saturation Power for the Single and Double-Pumped JBA	69
3.8 Experimental Setup for Measuring a Qubit with a Single-Pumped JBA	72
3.9 Experimental Setup for Measuring a Qubit with a Double-Pumped JBA	73
3.10 Ramsey Dephasing Time with a Single-Pumped JBA (Reproduced from Fig. 1.12)	74
3.11 Ramsey Dephasing Time with a Double-Pumped JBA (Reproduced from Fig. 1.13)	75

4.1	Schematic of the Heisenberg Back-Action of Phase-Sensitive Amplification (Reproduced from Fig. 1.15)	83
4.2	Schematic of the Heisenberg Back-Action of Phase-Preserving Amplification	85
4.3	Pulse Sequence for Measuring Heisenberg Back-Action	87
4.4	Angle Calibration for Phase-Sensitive Amplification	88
4.5	Measured Histograms of a Qubit Measured with Phase-Sensitive Amplification	88
4.6	Measured Heisenberg Back-Action for Phase-Sensitive Amplification along the I Quadrature	90
4.7	Measured Heisenberg Back-Action for Phase-Sensitive Amplification along the Q Quadrature	91
4.8	Measured Heisenberg Back-Action for Phase-Preserving Amplification . . .	92
4.9	Extraction of Measurement Efficiency from $\langle X \rangle_c$ and $\langle Y \rangle_c$	94
4.10	Extracted Bloch Vectors vs Measurement Strength for Phase-Sensitive and Phase-Preserving Amplification	95
5.1	Schematic of a Microwave Gyrator and Four-Port Circulator	100
5.2	Schematic of the Mode Coupling Options in the JPC	102
5.3	Schematic of the Josephson Circulator	104
5.4	Effect of Conversion Mismatch in the Josephson Circulator (theory)	105
5.5	Experimental Setup for Characterizing the Josephson Circulator and Direc- tional Amplifier	107
5.6	Measured Pairwise Conversion Processes for the Josephson Circulator . . .	108
5.7	Measured Scattering Parameters for the Josephson Circulator	110
5.8	Measured Response of the Josephson Circulator as a Function of Phase . .	111
5.9	Measured Effects of Conversion Mismatch	111
6.1	Pumping Schematic and Graphical Scattering Matrix for the Josephson Di- rectional Amplifier	118
6.2	Effect of Mismatched Conversion in the Josephson Directional Amplifier (the- ory)	120
6.3	Measured Pairwise Parametric Processes in the Josephson Directional Amplifier	121

6.4	Measured Scattering Parameters for the Josephson Directional Amplifier . .	123
6.5	Measured NVR for the Josephson Directional Amplifier	124
6.6	Measured Effect of Mismatched Conversion in the Josephson Directional Amplifier	125

List of Symbols

Symbol	Description
\mathbf{A}, \mathbf{B}	observables
$A_{in,out}(x, t)$	amplitude of incoming/outgoing waves along a transmission line
$\mathcal{A}_{in,out}(x, t)$	incoming/outgoing wave amplitude operator
$\mathbf{a}, \mathbf{a}^\dagger$	photon annihilation/creation operators
$\mathbf{a}_{in,out}$	traveling incoming/outgoing field amplitude
$\mathbf{a}'(t)_{in,out}$	Fourier transform of the field amplitude operator for only positive frequencies
a, b	outcome of a measurement of \mathbf{A}, \mathbf{B}
$\mathbf{b}, \mathbf{b}^\dagger$	photon annihilation/creation operators
$\mathbf{b}_{in,out}$	traveling incoming/outgoing field amplitude
$\mathbf{c}, \mathbf{c}^\dagger$	photon annihilation/creation operators
$\mathbf{c}_{in,out}$	traveling incoming/outgoing field amplitude
C	capacitance, or conversion coefficient, depending on context
C_i	capacitance of mode i
C_{ij}	conversion coefficient linking modes i and j
$\mathbf{d}, \mathbf{d}^\dagger$	photon annihilation/creation operators
$\mathbf{d}_{in,out}$	traveling incoming/outgoing field amplitude
E_J	Josephson energy
E_{JRM}	energy of the JRM
F	farad
f_{drive}	frequency of cavity drive generator

f_p	frequency of pump tone generator
f_{ref}	frequency of reference tone generator for signal demodulation
f_Δ	frequency of pump detuning tone generator for the DP-JBA
G	amplifier gain
G_{ij}	amplifier gain linking modes i and j
G_{tot}	total gain of a measurement chain
G_T	amplifier trans-gain
g_{ij}	three-wave mixing coefficient linking modes i and j
g_3	three-wave mixing coefficient
g_4	four-wave mixing coefficient
$ g\rangle, e\rangle$	ground and excited states of a qubit
\hbar	Plank's constant
H	Hamiltonian
H _{cQED}	cQED Hamiltonian
H _{JBA}	JBA Hamiltonian
H _{JPC}	JPC Hamiltonian
H _{3wave}	three-wave mixing Hamiltonian
H _{4wave}	four-wave mixing Hamiltonian
I, Q	in-phase and quadrature operators
I _{pp} , Q _{pp}	measurement operators for phase-preserving amplification
I	idler port
I, Q	in-phase and quadrature components of a signal, ($\langle \mathbf{I} \rangle$, $\langle \mathbf{Q} \rangle$)
I	current
$I(x, t)$	current along a transmission line
I_{in}, Q_{in}	in-phase and quadrature component of an incoming signal
$\bar{I}_{in}, \bar{Q}_{in}$	center of the distribution for the in-phase and quadrature components of an incoming signal
I_m, Q_m	measured in-phase and quadrature component of a signal
\bar{I}_m, \bar{Q}_m	center of the measured distribution of a signal in phase space

I_{out}, Q_{out}	in-phase and quadrature component of an outgoing signal
$\bar{I}_{out}, \bar{Q}_{out}$	center of the distribution for the in-phase and quadrature components of an outgoing signal
I_0	critical current of a Josephson junction
I_s	critical current of a SQUID
K	environmental coupling matrix
k_B	Boltzmann's constant
$\vec{L} = (l_x, l_y, l_z)$	classical angular momentum vector and its components
$\mathbf{L}_x, \mathbf{L}_y, \mathbf{L}_z$	angular momentum observables
L	inductance
L_i	inductance of mode i
M	mode coupling matrix
$M_{I_m, Q_m, I_m Q_m}$	measurement operator for a phase-sensitive measurement along I , phase-sensitive measurement along Q , or a phase-preserving measurement
m	meter, or wavelet frequency index depending on context
\mathcal{N}_{in}^i	photon spectral density incident on mode i
n	integer, for instance photon number in a cavity
\bar{n}	average number of photons in a coherent state in a cavity
\bar{n}_{tot}	average number of photons in a coherent state in a cavity from all sources
P	pump port
P_{-1dB}	signal power at which the gain of an amplifier drops by 1 dB
P_{ij}^p	pump power applied to couple modes i and j
$P(i)$	probability of getting measurement result i
$\mathbb{P}(i i_m)$	conditional probability a perfect measurement would have yielded result i given that an imperfect measurement yielded i_m
p	wavelet time index

Q	charge
Q_{in}^c, Q_{out}^c	input and output coupling quality factor
$R_{x,y}(\pi/2)$	$\pi/2$ rotation around the x,y axis
$\langle R \rangle$	unconditional Bloch Vector
$\langle R \rangle_c$	conditional Bloch vector
$\vec{S} = (x, y, z)$	Bloch vector and its components
s	scattering matrix
s_{circ}	scattering matrix for the Josephson circulator
s_{da}	scattering matrix for the directional amplifier
s_{ij}	scattering element
T	temperature
T_{amp}	paramp noise temperature
$T_{amp}^{SP,DP}$	single-pumped/double-pumped JBA noise temperature
T_{sys}	system noise temperature
T_m	measurement time
T_1	qubit relaxation time
T_{2R}	Ramsey decoherence time
t	time
U_{amp}	unitary performed by a parametric amplifier
U_{cQED}	CQED unitary
V	vacuum port
$V(x, t)$	voltage across a transmission line
$w_{in,out}^{mp}$	wavelet
$\mathbf{X}, \mathbf{Y}, \mathbf{Z}$	spin operators
$\langle X \rangle_c, \langle Y \rangle_c, \langle Z \rangle_c$	measured average Bloch vector component conditioned on the measurement result (I_m, Q_m)
$x_{i,f}^{I,Q}, y_{i,f}^{I,Q}, z_{i,f}^{I,Q}$	initial and final Bloch vector components after a phase-sensitive measurement along I, Q , or phase preserving measurement (no superscript)

Z_c	Characteristic impedance of a transmission line
Z_i	Characteristic impedance of mode i
α^P	complex amplitude of internal pump field
$\alpha^{(+,-)}$	complex amplitude of the internal pump fields for the two pumps of the DP-JBA
$\alpha_{in,out}^P$	amplitude of incoming/outgoing pump field
α_0^P	complex zeroth order solution to the internal pump amplitude
$\alpha_{in,out}^{(+,-)}$	amplitude of the incoming/outgoing pump fields for the DP-JBA
$\alpha_0^{(+,-)}$	complex zeroth order solution to internal pump amplitudes
$ \alpha\rangle$	coherent state with complex amplitude α
$ \alpha_{g,e}\rangle$	cavity ground and excited state
β_{ij}	cross mode couplings
γ_M	mode normalization factor
$\gamma_{cc}(G, P_{in}^c),$	relations between the internal signal fields and the incoming
$\gamma_{cc^\dagger}(G, P_{in}^c)$	signal fields the DP-JBA
γ_ϕ	measurement induced dephasing rate
Δ	detuning of the two pump tones from the frequency of maximum gain in the DP-JBA
δ_{ii}	self mode couplings
δ_ω	frequency detuning from resonance
η	efficiency of whole measurement chain
θ	angular phase shift of Fresnel lollipop
κ	linewidth of readout cavity
κ_i	linewidth of mode i
Λ	pump dependent four-wave mixing term for the JBA
λ	wavelength
μ_{ij}	dimensionless gain or conversion coupling coefficient
ρ	normalized pump power of the JPC

ρ_{eff}	normalized effective pump power for the JBA
ρ_i, ρ_f	initial and final density matrix
$\sigma_{I,Q}$	measured standard deviation of the Fresnel lollipop along the I or Q quadrature
σ_{Heis}	contribution to the standard deviation of the Fresnell lollipop along the I or Q quadrature due to Heisenberg uncertainty principle
σ_{add}	contribution to the standard deviation of Fresnel lollipop along the I or Q quadrature due to added non-Heisenberg noise
σ_i	standard deviation of measurements of observable i
τ	wavelet pitch in time
Υ	pump dependent frequency shift in the JBA
Φ	flux
Φ_{ext}	external magnetic flux
Φ_i	flux through branch i
$\Phi_{I,II,III,IV}$	node fluxes JRM
ϕ_p	pump phase
ϕ_p^{eff}	effective pump phase for the JBA
ϕ_{p1}, ϕ_{p2}	phase of pump 1 and 2
$\phi_p^{a,b,c}$	phase of pump applied to mode a, b , or c
ϕ_{rel}	relative phase between the cavity drive and the pump generator; phase which determines the amplified quadrature in a phase-sensitive amplification process
ϕ_{tot}^{circ}	total pump phase for the circulator
ϕ_{tot}^{d-a}	total pump phase for the directional amplifier
φ_0	reduced flux quantum
$\varphi_{ext} = \Phi_{ext}/\varphi_0$	reduced external flux
$\varphi_i = \Phi_i/\varphi_0$	reduced flux through mode or branch i
χ	dispersive shift between qubit and cavity

$\Psi = c_g g\rangle + c_e e\rangle$	general quantum state with complex coefficients c_g and c_e
$\psi_{in,out}^{-mp}$	incoming/outgoing photon ladder operator
$ \Psi_{I_m, Q_m, I_m Q_m}\rangle$	eigenstate of the mode after a phase-sensitive measurement along I , Q , or a phase-preserving measurement
ω	angular frequency
$\omega_{a,b,c}$	angular frequency of mode a , b , c
ω_c^g, ω_g^e	angular frequency of cavity when the qubit is in $ g\rangle$ or $ e\rangle$
ω_g	angular frequency of maximal gain in the JBA
ω'_i	unshifted angular frequency of mode i
$\omega_{pump1}, \omega_{pump2}$	pump angular frequency the two pumps of the DP-JBA
ω_q	qubit angular frequency
$\omega_{s,i,p}$	angular frequency of signal, idler, and pump tones
$\omega_{1,2}$	applied tone angular frequency
Ω	ohm
$\omega_p^{a,b,c}$	pump frequency applied to mode a, b , or c
$ 0\rangle$	vacuum state of the cavity

List of Acronyms

AC	alternating current
AWG	arbitrary waveform generator
cavity QED	cavity quantum electrodynamics
cQED	circuit quantum electrodynamics
DC	direct current
DP-JBA	double-pumped JBA
HEMT	high electron mobility transistor
JBA	Josephson bifurcation amplifier
JDA	Josephson directional amplifier
JPC	Josephson parametric converter
JRM	Josephson ring modulator
NVR	noise visibility ratio
MSA	microstrip SQUID amplifier
paramp	parametric amplifier
PC-board	printed circuit board
qubit	quantum bit
RF	radio-frequency
RWA	rotating wave approximation
SEM	scanning electron microscope
SLUG	superconducting undulatory galvanometer
SP-JBA	single-pumped JBA
SQUID	superconducting quantum interference device

TWPA	traveling wave parametric amplifier
VNA	vector network analyzer

Glossary

Coherent frequency conversion: Parametric process in which signal photons are coherently converted into idler photons (and vice versa) through an interaction which is mediated by a pump whose frequency is the difference between that of the signal and the idler photons. In full conversion ($C = 1$) signal and idler photons are exchanged one for one.

Degenerate parametric amplifier: Parametric amplifier in which the signal and idler tones excite the same normal modes of the circuit.

Directional amplifier: Two or more port amplifier which functions like a valve. Signals are amplified from input to output and attenuated from output to input.

Heisenberg back-action: Update of the expectation value and uncertainty of a new measurement outcome of an observable as a result of the outcome of a measurement made on a second observable which does not commute with the first.

Idler: One of the three tones associated with parametric processes. It is the tone that arises due to conservation of phase-space in a multi-mode mixing process. Its frequency is noted by ω_i . In a three-wave mixing process, $\omega_i = \omega_p - \omega_s$ for parametric amplification or $\omega_i = \omega_s - \omega_p$ for coherent conversion, while in a four-wave mixing amplification process $\omega_i = 2\omega_p - \omega_s$.

Incoming/outgoing electromagnetic field operators: Operators associated with the incoming and outgoing amplitudes of the electromagnetic waves applied to a port of a circuit.

Matched amplifier: Amplifier in which all ports are matched.

Matched Port: Port at which no incident signals are reflected.

Measurement efficiency: If measurements of an ensemble of systems prepared with

the same initial state yield a distribution with standard deviation σ_I , and if an ideal set of measurements on the ensemble would yield a distribution with the standard deviation σ_{Heis} , set by the Heisenberg uncertainty principle, then the efficiency of the un-ideal measurement is the ratio $\sigma_{\text{Heis}}^2/\sigma_I^2$.

Meter: Apparatus used to make a measurement.

Non-degenerate parametric amplifier: Parametric amplifier in which the signal and idler tones excite different normal modes of the circuit.

Normal mode: Vector of the basis that simultaneously diagonalizes the matrices of the quadratic forms associated with the kinetic and potential energy terms of the Hamiltonian of a linear system.

Parametric amplification: Amplification process in which pump photons are converted into pairs of signal and idler photons leading to an increase in the amplitude of both the signal and the idler.

Phase-preserving amplification: Mode of operation for a parametric amplifier in which both quadratures of the signal are amplified by the same factor. Necessarily adds half a photon of noise to the signal.

Phase-sensitive amplification: Mode of operation for a parametric amplifier in which one quadrature of the signal is amplified while the other is de-amplified by the same factor. No extra noise needs to be added in this type of amplification process.

Port: Interface between a part of a circuit and a transmission line. Allows for incoming and outgoing waves to be exchanged between the circuit and the environment.

Pump: One of the three tones associated with parametric amplification. This tone provides the energy needed for parametric amplification or coherent frequency conversion. Its frequency is noted by ω_p .

Quadrature operators: Analogs of the position and momentum operators for a temporal mode of an electromagnetic signal: $\mathbf{I}_{in,out} = (\mathbf{a}_{in,out} + \mathbf{a}_{in,out}^\dagger)/2$ and $\mathbf{Q}_{in,out} = (\mathbf{a}_{in,out} - \mathbf{a}_{in,out}^\dagger)/(2i)$ where $\mathbf{a}_{in,out}$ are the incoming and outgoing electromagnetic field operators. Can also be defined for standing waves: $\mathbf{I} = (\mathbf{a} + \mathbf{a}^\dagger)/2$ and $\mathbf{Q} = (\mathbf{a} - \mathbf{a}^\dagger)/(2i)$ where \mathbf{a} (\mathbf{a}^\dagger) is the photon creation (annihilation) operator for the mode.

Reflection amplifier: Parametric amplifier in which signals incident on the input port

are reflected with gain.

Signal: One of the three tones associated with parametric processes. The tone which originates from the system we would like to amplify or convert. Its frequency is noted by ω_s .

Tone: A monochromatic (single frequency) electromagnetic wave traveling along a transmission line and applied to a circuit.

Through amplifier: Two or more port parametric amplifier in which signals are amplified from the input to the output. Signals may also be amplified from the output to the input, but unlike a reflection amplifier, no signals incident on the input are reflected with gain.

Chapter 1

Introduction

1.1 Back-Action in Quantum and Classical Systems

One of the most fundamental relations in quantum mechanics is the Heisenberg uncertainty principle. It states that if we have a system with two non-commuting observables, \mathbf{A} and \mathbf{B} , and if measurements of \mathbf{A} or \mathbf{B} on an ensemble of systems prepared with the same initial state yield two distributions of outcomes characterized by the standard deviations $\sigma_{\mathbf{A}}$ and $\sigma_{\mathbf{B}}$, then there is a minimum uncertainty in the product of the standard deviations given by $\sigma_{\mathbf{A}}\sigma_{\mathbf{B}} \geq \frac{1}{2}|\langle[\mathbf{A}, \mathbf{B}]\rangle|$ [1]. This can be thought of as a limit on how precisely we can know the full set of observables which are possible to measure in our system. More interestingly the principle also enforces a dynamic interaction between the state of a system and the result of a measurement. For example, suppose that \mathbf{B} is measured and yields some outcome b . If $|\langle[\mathbf{A}, \mathbf{B}]\rangle| = \hbar$ and \mathbf{A} is then measured to a particular precision $\sigma_{\mathbf{A}}$, then the outcome of a subsequent measurement of \mathbf{B} will deviate from b by a random amount with standard deviation $\hbar/(2\sigma_{\mathbf{A}})$, as if a ‘kick’ had been given to the variable \mathbf{B} . This kick can be described as the Heisenberg back-action of the measurement.

This Heisenberg, or unavoidable, back-action has some rich and unexpected consequences. To put it in context, suppose we were to make a sequence of perfect classical measurements of a set of observables (that can be repeated), such as the sequence $\mathbf{L}_z, \mathbf{L}_x, \mathbf{L}_z$, where $\mathbf{L}_x, \mathbf{L}_y$, and \mathbf{L}_z are the angular momentum components of a top. Then we would find perfect correlations between the outcomes for the first and second measurements of

\mathbf{L}_z (see Fig. 1.1). Furthermore, we will find the same outcome for repeated measurements of any observable regardless of what other observables are measured in between them. If, instead, we were to make a sequence of perfect quantum measurement on a set of non-commuting observables, for example the sequence of spin components \mathbf{Z} , \mathbf{X} , \mathbf{Z} for a spin $1/2$ system, then the situation would be very different. The outcome of the second measurement of \mathbf{Z} will not have any correlation with the outcome of the first measurement of \mathbf{Z} . The Heisenberg back-action from the measurement of \mathbf{X} effectively erased all information about the previous measurement of \mathbf{Z} , even if the measurement is made perfectly.

Regrettably, there are other ways to lose track of the previous measurement of \mathbf{Z} that are not due to erasure by Heisenberg back-action. The signal-to-noise ratio of the measurement of \mathbf{Z} may not be high enough, leading to a measurement result which is not sufficiently meaningful. There may be classical forms of back-action which would change the outcome of a measurement of \mathbf{Z} : the apparatus used to make the measurement, known as the “meter”, may send a continuous stream of noise back toward the system, which may perturb the state of the system. Or, the act of coupling the system and the meter may directly change the state of the system. For example, if one tries to measure the voltage across a small capacitor with a multi-meter, the coupling between capacitor and the multi-meter will cause the capacitor to discharge. There may also be other quantum, but non-Heisenberg ways to lose track of the previous measurement of \mathbf{Z} . Information about the state of the system may be lost due to measurements made by other observers, or by the environment itself, if the results of such measurements are not reported to us [2].

Sufficiently uncorrupted Heisenberg back-action can provide a powerful way to apply operations on quantum systems. One such application is remotely entangling two quantum systems via measurement (see Fig. 1.2). Recall that if we have two such quantum systems, and measure the \mathbf{Y} component of each one individually, and then measure the \mathbf{ZZ} axis of the joint system, the resulting Heisenberg back-action erases the \mathbf{Y} information of both single qubits, and entangles the two systems. When a measurement is then made on one of the individual quantum systems, the outcomes will then either be perfectly correlated or anti-correlated depending on the outcome of the measurement of \mathbf{ZZ} . Remarkably, this entanglement by measurement can be carried out even if the two qubits cannot be directly

jointly measured. It suffices then to measure two ancillas that have each been deterministically entangled with the qubits [3–9]. In this case no direct interaction between the two remote qubits is ever needed. Entangling operations are both a fascinating feature of quantum mechanics, and also an essential component if one wants to store and manipulate information in quantum systems [1]. The application of such operations using the Heisenberg back-action of measurement requires control over the other effects in our system which cause us to lose track of previous measurement results.

Some detrimental effects, such as the addition of large amounts of classical noise to our delicate quantum signals, can be minimized with improved measurement instruments and protocols. Amplifiers, particularly ultra-low-noise amplifiers, are one of the main tools in fighting these undesired effects. They are essential in raising the level of a quantum signal above the noise level of the classical measurement apparatus, and have already allowed for the observation of purely quantum effects, such as the jumping of a system between eigenstates [10, 11]. Unfortunately, either the amplifiers themselves, or the additional hardware needed to integrate them into an experiment, can cause additional effects which limit our ability to control quantum systems via Heisenberg back-action.

This thesis will present three improvements to our measurement systems which minimize two such deleterious effects: the dephasing of the quantum system due to tones reflected from the amplifier, and energy loss between the quantum system and the amplifier. This chapter will serve to introduce the quantum system we will be measuring, the superconducting qubit, the main effects limiting the manipulation of our qubits by Heisenberg back-action, and the two ultra-low noise parametric amplifiers that form the basis for our measurement apparatuses. The three improvements we have realized are also succinctly described: replacing the single pump tone of one type of amplifier with two spectrally separated pump tones in order to reduce qubit dephasing, replacing the microwave circulators, which are the main source of the loss between the qubit and amplifier, with a theoretically loss-less Josephson circulator, and replacing our current ultra-low-noise amplifiers with a directional version which only operates in transmission. These improvements have key roles in the observation and utilization of Heisenberg measurement back-action.

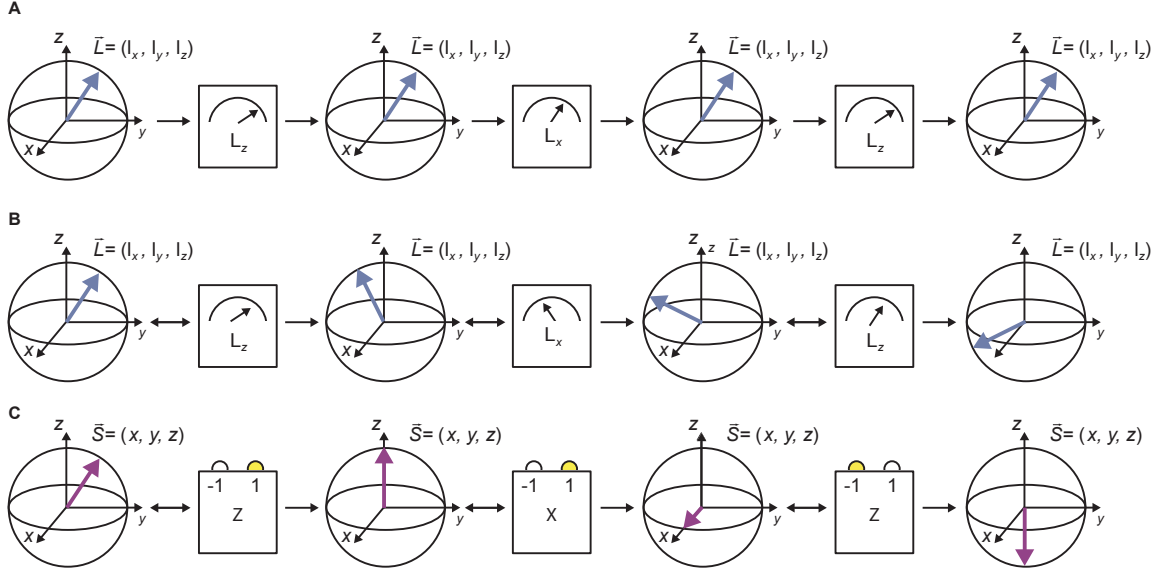


Figure 1.1: Different Types of Measurement Back-Action. A) Ideal classical measurement without any measurement back-action. A classical object such as a top can have a well defined set of observables such as the components of the angular momentum vector \vec{L} . Measurements can be made on any individual component of \vec{L} while leaving \vec{L} unchanged. B) Non-ideal classical measurement with possible back-action induced by the apparatus. In a non-ideal measurement the coupling between the measurement apparatus and the system may induce some unwanted classical back-action. In this case, repeated measurements of the same component of \vec{L} may not give the same result. C) Ideal projective quantum measurement with only Heisenberg back-action. If we instead have a quantum object like a spin 1/2 with a Bloch vector \vec{S} the situation is fundamentally different. Measurement results only take one of two values instead of a continuum, with the value of a component of \vec{S} giving the relative probabilities of the result of a measurement to be ± 1 . As a result of the Heisenberg uncertainty principle, different components of \vec{S} cannot be simultaneously known. This gives rise to an entirely different type of measurement back-action, Heisenberg back-action, where the value of a component, for example z , can be erased by interleaving measurements of a non-commuting component.

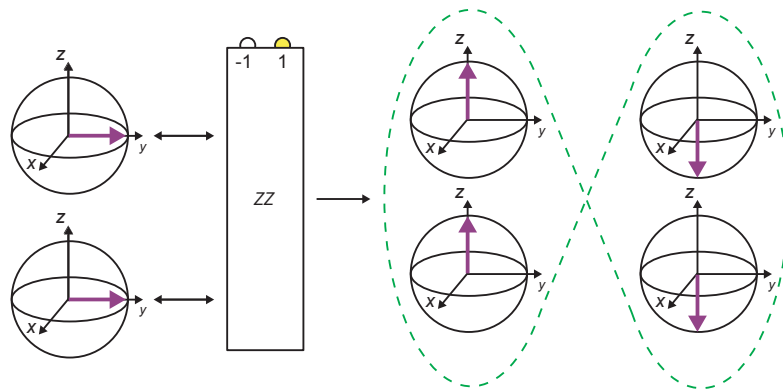


Figure 1.2: Entanglement by Heisenberg back-action. One useful consequence of the erasure nature of measurement due to the Heisenberg uncertainty principle is it that measurement back-action can create desirable correlations. For example, the back-action resulting from measuring the \mathbf{ZZ} component of the joint system of two spins starting with well-defined single-spin \mathbf{Y} components will lead to entanglement between them (represented by the dashed green paths). The back-action of the measurement erases all information about the single qubit spin operators, and instead enforces correlations between the outcomes of the single qubit measurements.

1.2 Superconducting Qubits

We would like to investigate and manipulate, using Heisenberg back-action, a special kind of quantum system known as a qubit. A qubit is a two-level quantum system that can be used to store and manipulate information, that serves as the quantum analog of a classical computer bit, i.e. a two-state classical system that is also used to store and manipulate information. The two levels of a qubit are typically labeled as $|g\rangle$ and $|e\rangle$, but unlike a classical bit, our qubit can be in an arbitrary superposition of these two states given by $\Psi = c_g |g\rangle + c_e |e\rangle$ with the condition that $|c_g|^2 + |c_e|^2 = 1$. Many different physical systems, from real atoms, to certain crystalline structures, to electronic circuits can function as qubits [1], but we chose to focus on qubits made from superconducting electronic circuits.

The simplest such circuits are electromagnetic oscillators composed of capacitors and inductors. In such a system the two main variables are the flux through the inductor $\Phi = LI$, leading to an effective potential energy $\Phi^2/(2L)$, and the charge Q on the capacitor leading to an effective kinetic energy $Q^2/(2C)$. Like the mechanical analog, the energy levels are discrete and equally spaced. When such an oscillator is well separated from its environment, and cooled to a very low temperature, it will settle into its ground state which will serve as the first level of our qubit $|g\rangle$. The first excited state will serve as the second level, $|e\rangle$, but the degeneracy in level spacing prevents us from using these two states exclusively. We can remove the degeneracy in energy level spacing by replacing the inductor, which has a linear current-flux relationship, with a special superconducting circuit element called a Josephson junction, which has a non-linear current-flux relationship given by $I = I_0 \sin(\frac{\Phi}{\varphi_0}) = I_0 \sin(\varphi)$, where I_0 is the critical current of the junction and φ_0 is the reduced flux quantum. This creates an anharmonic oscillator with individually addressable energy levels. If we restrict ourselves to the first two levels of the anharmonic oscillator, then our system can now function as a qubit

We then place our qubits in microwave cavities, which both serve to protect the qubit from broadband noise, and as a convenient way to probe the state of the qubit. The study of atoms interacting with light in a cavity is known as cavity quantum electrodynamics (cavity QED) [12, 13] and has been an active area of research since the 1980s. Many of the

techniques are directly applicable to the study of electronic circuits in microwave cavities, an extension of cavity QED known as circuit quantum electrodynamics (cQED) [14, 15]. In the dispersive limit, where the qubit is strongly detuned from the cavity [14], the Hamiltonian of a qubit in a cavity is given by $\mathbf{H}_{\text{cQED}}/\hbar = \omega_c \mathbf{a}^\dagger \mathbf{a} + \omega_q \mathbf{b}^\dagger \mathbf{b} + \chi \mathbf{a}^\dagger \mathbf{a} \mathbf{b}^\dagger \mathbf{b}$. It depends on the energy of the cavity alone $\hbar\omega_c \mathbf{a}^\dagger \mathbf{a}$, the energy of the qubit alone $\hbar\omega_q \mathbf{b}^\dagger \mathbf{b}$ and the coupling between the cavity and the qubit which is parameterized by the so-called dispersive shift χ . The cavity is then coupled to the outside world which allows manipulation of both the cavity and the qubit states, as well as measurements. This coupling sets the decay rate, κ , of the cavity. As can be seen from the Hamiltonian, a change in the state of the qubit shifts the resonant frequency of the cavity by χ . If we probe the resonator with a coherent state $|\alpha\rangle$, we can detect the change in frequency by looking for a change in either amplitude or phase of the coherent state after leaving the cavity.

Coherent states are most easily visualized in phase-space parameterized by the in-phase, I , and quadrature, Q , components of the state. In this space, a coherent state is represented by a Gaussian distribution with standard deviation $\sigma_I = \sigma_Q = 1/2$ whose center is located at the end of a vector originating at the origin of length given by the square root of the average number of photons in the state $\sqrt{\bar{n}}$, where $\bar{n} = |\alpha|^2$. This shape is nicknamed the Fresnel lollipop. As seen in Fig. 1.3, before the cavity the coherent state is given by a single disk in the I, Q plane. After the cavity the Fresnel lollipop is split in two, with one disk corresponding to the state when the qubit is in $|g\rangle$ and the other corresponding to qubit being in $|e\rangle$, and the angle between them given by $\pm\theta/2 = \arctan(\chi/\kappa)$. The result of an individual measurement of the qubit is a single pair of numbers (I_m, Q_m) . If this point lies in the disk corresponding to $|g\rangle$ ($|e\rangle$), the qubit has been measured to be in the ground (excited) state. If all of our quantum measurements were perfect, all of the measurement results corresponding to $|g\rangle$ would recreate the expected Fresnel lollipop for the qubit in the ground states.

Actual measurements of this quantum system are not perfect, and these imperfections may limit our ability to control our qubits via the Heisenberg back-action of measurement. First, our meter may send photons back toward our cavity. These photons can cause fluctuations in the number of photons in the cavity, which in turn causes fluctuations in

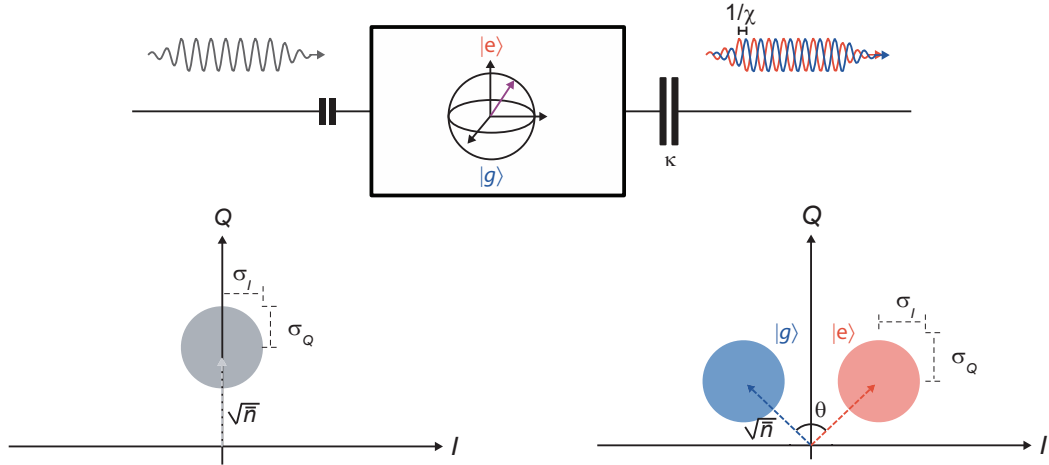


Figure 1.3: Cavity QED Schematic with Fresnell lollipops. A) Cavity QED consists of a two-level quantum system placed in a cavity, both of which can be individually addressed by microwave pulses applied to a weakly coupled port of the cavity. The quantum system and cavity are coupled such that changes in the state of the quantum system, labeled as $|g\rangle$ and $|e\rangle$, shift the frequency of the cavity. This shift can be measured via a phase shift of a coherent state that leaks out of the cavity at rate $1/\kappa$ via the strongly coupled port of the cavity. B) The coherent state cavity drive is represented as a Gaussian disk in I, Q space with standard deviation $\sigma_I = \sigma_Q = 1/2$ and a displacement from the origin given by the square root of average number of photons in the pulse $\sqrt{\bar{n}}$. After traversing the cavity the pulse can be represented as two disks in I, Q space representing the two possible cavity states (red, blue) depending on the state of the qubit $|g\rangle, |e\rangle$. The states after the cavity have the same displacement from the origin and same standard deviation as the coherent state input on the cavity.

the frequency of the qubit [16, 17]. This causes our quantum state to lose phase coherence at a rate $\gamma_\phi = 2\bar{n}_{tot}\kappa \sin^2(\theta/2)$, where \bar{n}_{tot} is the average number of photons in the cavity from all sources. Photons in the cavity can also enhance the relaxation rate between the excited state and the ground state of the qubit. We can quantify this effect by directly measuring the coherence times of the qubit while connected to the active measurement apparatus. Second, our signal may experience losses between the cavity and the meter. This is analogous to the environment learning about the state of the qubit rather than the meter, and takes our qubit out of the space where $|c_g|^2 + |c_e|^2 = 1$. Third, our meter may add a large amount of noise to the signal, making discrimination of the state difficult on a shot by shot basis.

We can quantify the second and third imperfections by looking at how the measurement

affect the standard deviation of the Fresnel lollipop, σ_I and σ_Q . The standard deviation of a perfectly measured coherent state $\sigma_I = \sigma_Q = \sigma_{\text{Heis}} = 1/2$ arise from the non-commutativity of the variables I and Q and thus are representative of Heisenberg back-action. In general, the variance of the Fresnel lollipop along either the I or Q quadrature, $\sigma_{I,Q}^2$, has a contribution from the Heisenberg back-action given by σ_{Heis} , and a contribution from non-Heisenberg added noise, σ_{add} , such that $\sigma_{I,Q}^2 = \sigma_{\text{Heis}}^2 + \sigma_{\text{add}}^2$. We can define a quantity $\eta = \sigma_{\text{Heis}}^2 / \sigma_{I,Q}^2$, known as the measurement efficiency, which gives us a measure of these relative back-actions. For $\eta = 1$ our measurement does not add any additional noise and thus we can easily see quantum effects. For $\eta \ll 1$ added noise will dominate, and will completely obscure the Heisenberg back-action effects we want to explore.

1.2.1 Amplification of Quantum Signals

If we were to make our measurement with the hot, classical meter alone, σ_{add} would dominate to the point that determining the state of the qubit would be impossible. We need an amplifier to boost the signal to the point where we can ‘lay our grubby classical hands’ [18] on the quantum signal. The first amplifiers used in cQED experiments were high electron mobility transistor (HEMT) amplifiers. They typically provide around 40 dB of gain, but also add around 20 photons of noise. Although this is high enough gain and low enough noise to determine the state of a qubit (Fig. 1.4), it is much higher than the Heisenberg contribution alone. The measurement efficiency of such measurement setups is a few percent, which is not nearly high enough to directly explore the Heisenberg effects of the measurement process.

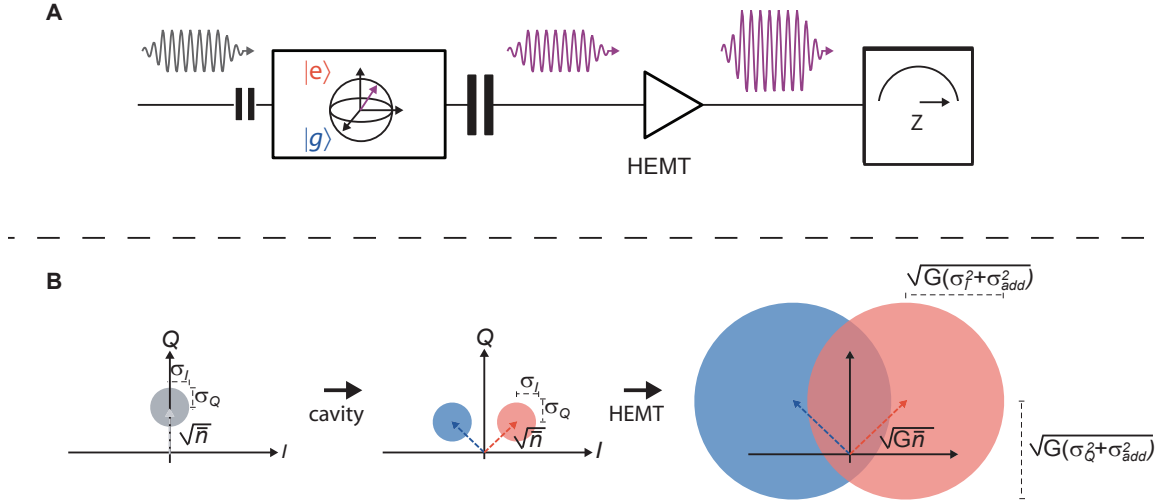


Figure 1.4: Cavity QED Measurement with a HEMT. These amplifiers increase typically provided enough power gain, G , to overcome the enormous amount of noise of room temperature meter, but they also add a large amount of classical noise σ_{add} of their own. This leads to a significant overlap of the two states in I, Q space. A) shows the propagation of signals through such an experimental setup (with the coherent state after the cavity now shown in purple to indicate a superposition of $|\alpha_g\rangle$ and $|\alpha_g\rangle$), while B) shows the effects of each stage on the input coherent state to the cavity.

The next great development came with quantum-limited parametric amplifiers (paramps). A parametric amplifier is a device in which pump photons are converted into pairs of signal photons and idler photons, via an interaction with a non-linearity of the system. A quantum-limited parametric amplifier is one which only adds additional Heisenberg noise [18]. Our paramps typically achieve gains of 20+ dB, which is insufficient to make them the only amplifier used in an experiment and they are typically backed by HEMTs. Fortunately, in a system of cascaded amplifiers, the noise of subsequent amplifiers, parametrized by the system noise temperature T_{sys} , is reduced by a factor of the power gain, G of the first amplifier. If T_{amp} is the noise temperature of the paramp, then the total noise of the measurement chain is given by $T_{\text{amp}} + T_{\text{sys}}/G$. Thus, 20 dB of gain from a quantum limited paramp is enough to ensure the amplified Heisenberg noise from the paramp is the dominant noise contribution. Although quantum limited paramps themselves do not necessarily reduce our measurement efficiency, they may require additional components in the measurement chain which do. The primary example is the microwave circulator, a device which directs

signals between its ports in only one direction, which is essential if the paramp operates in reflection (see. Fig. 1.5). Measurement setups with parametric amplifiers typically have efficiencies around 50% [11, 19–22]. This is high enough to begin to explore the Heisenberg back-action of certain amplification schemes [11], as well as enabling the observation of quantum jumps [10, 11], quantum trajectories [19, 21, 23, 24], and allowing for measurement based feedback [20, 25–27]. It is unfortunately not quite high enough to exploit Heisenberg back-action to perform high fidelity unitary operations such as remote entanglement [28].

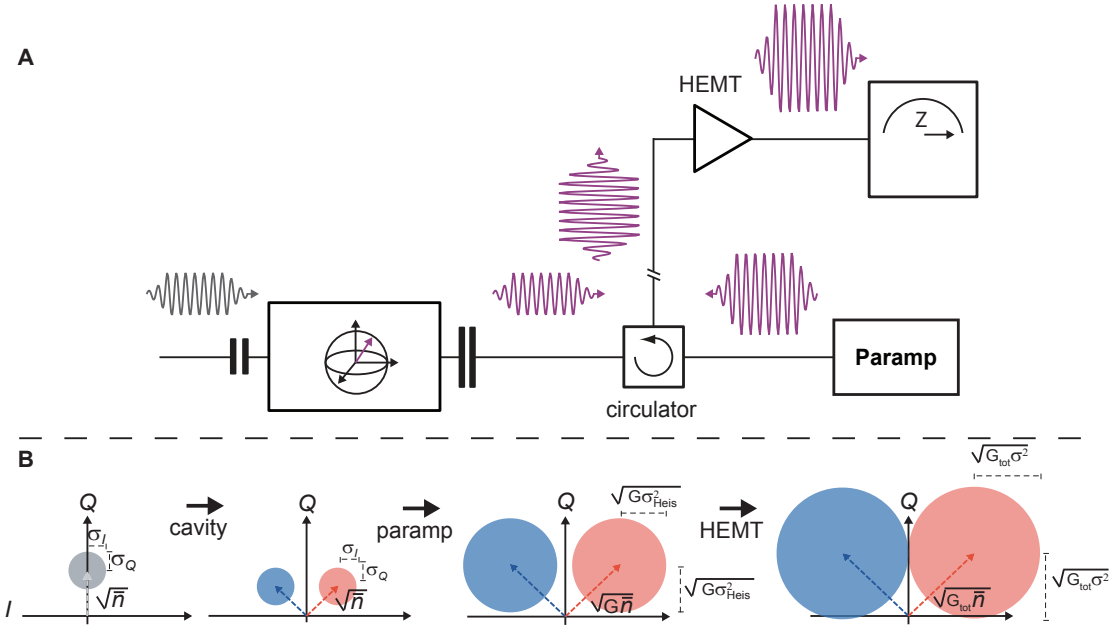


Figure 1.5: Cavity QED Measurement with a Paramp. Quantum-limited paramps are widely used pre-amplifiers to HEMT. The most commonly used paramps operate in reflection, necessitating at least one circulator be included to separate incoming from outgoing signals. Paramps also amplify the signal from a cavity by an factor proportional to their amplitude gain \sqrt{G} . They may add a half-photon of noise to the signal, although this noise also arises from the Heisenberg uncertainty principle and is much lower than that added by the HEMT. A HEMT is included, boosting the amplitude gain of the chain to $\sqrt{G_{\text{tot}}}$. The HEMT still adds some additional noise, σ_{add} resulting in $\sigma^2 = \sigma_{\text{Heis}}^2 + 1/G\sigma_{\text{add}}^2$, but if the gain, of the paramp is sufficiently large, the added noise from the HEMT is small, and the two cavity states are still distinguishable.

The first paramp we will focus on is the Josephson Parametric Converter (JPC). The JPC was originally developed at Yale [29, 30] and further refined at ENS Paris [31, 32] and Yale [33–35]. It is used as a parametric amplifier in superconducting qubit experiments [11, 20, 24, 27, 34, 36–42]. The JPC is composed of the Josephson Ring Modulator (JRM), a

ring of four Josephson junctions shunted by four linear inductors, embedded at the central current antinodes of two crossed $\lambda/2$ -resonators (see Fig. 1.6). The circuit has three modes, **a** and **b** which are excitations of each resonator individually, and **c**, which is a common-mode excitation of both. Each resonator is coupled to a transmission line via a gap coupling capacitor, which sets the linear bandwidth of the modes. The non-linearity of the JRM allows for amplification via a three-wave mixing process, where a single pump photon applied to one mode at $\omega_p = \omega_s + \omega_i$ is converted into a signal photon at frequency ω_s and an idler photon at frequency ω_i . Any of the three modes, **a**, **b** or **c** can support the signal, pump or idler. The JPC amplifies in reflection, necessitating circulators be included in the setup to separate incoming from outgoing signals (see Fig. 1.7).

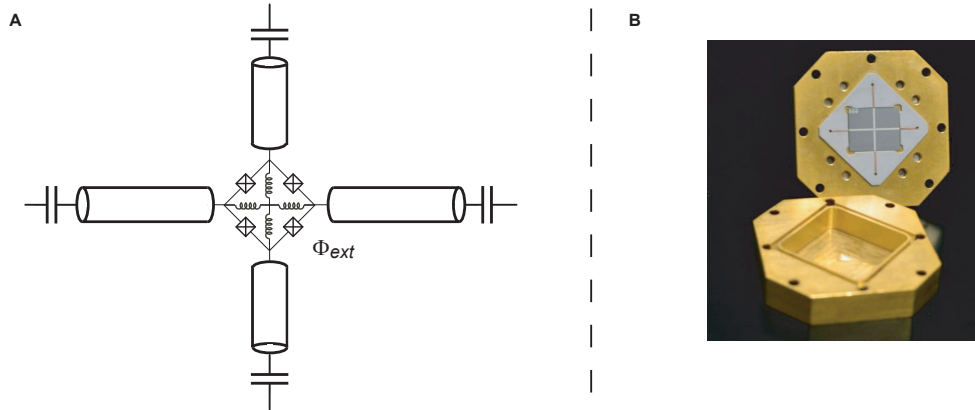


Figure 1.6: Schematic and optical image of the JPC A) The JPC consists of a ring of four Josephson junctions shunted by four larger more linear inductors. This ring is placed at the common current antinode of two intersecting $\lambda/2$ resonators. The resonators are terminated by gap coupling capacitors which set the linear bandwidth of the modes. B) Photograph of the complete amplifier. It shows the JPC chip (dark gray) with the two resonators visible in light gray. Also visible is the PCB board (square, white) whose role is to provide the interface between the chip and the SMA connectors (not visible) located on the back of the gold housing.

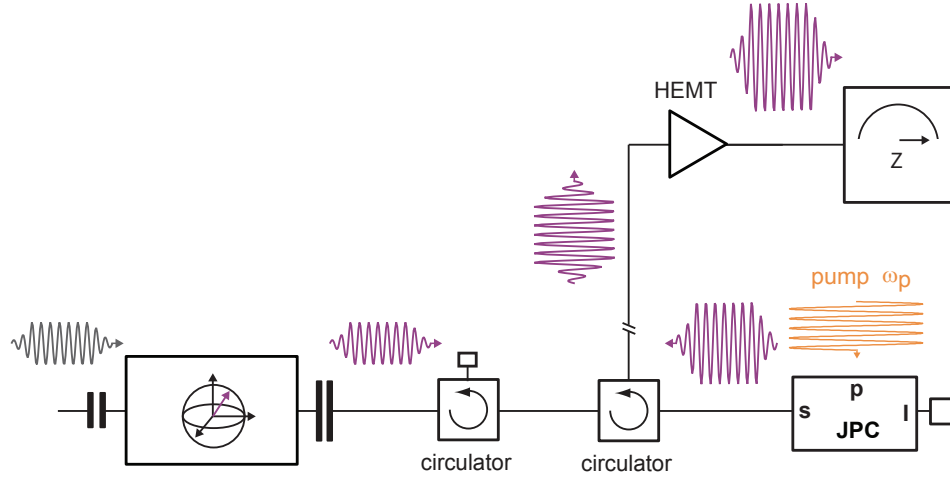


Figure 1.7: Cavity QED measurement with the JPC. The JPC has three spatially and spectrally separated ports: one for the pump, one for the idler which is often terminated in a cold 50Ω load, and one for the signal which is typically matched in frequency to the cavity. The JPC operates in reflection, necessitating at least one circulator to separate input from output, with an additional circulator is typically used in order to avoid dephasing from the finite isolation of the reflected gain. The amplified signal is again directed toward higher stages of amplification from a HEMT before the result is recorded at room temperature.

The second amplifier we will focus on is the Josephson Bifurcation Amplifier (JBA). The JBA was originally developed at Yale [43], and is also used as a parametric amplifier in superconducting qubit experiments (see for example [9, 10, 19, 21, 23, 25, 44–50]), nano-mechanical motion sensor [51, 52] and a dispersive magnetometer [53–55]. It is a single port, single mode device composed of a SQUID, i.e. a pair of Josephson junctions connected in a loop, shunted by a large external capacitor (see Fig. 1.8). The non-linearity of the SQUID allows the JBA to achieve amplification via four-wave mixing, a process where two pump photons at frequency $2\omega_p = \omega_s + \omega_i$ are converted into a signal photon and an idler photon. The JBA also amplifies in reflection (see Fig. 1.9), and requires circulators both to separate input from output and to decrease the amplitude of the strong reflected pump tone. The pump tones used are orders of magnitude larger than that of the signal from the cavity, and it is difficult to provide enough isolation to protect the qubit from dephasing.

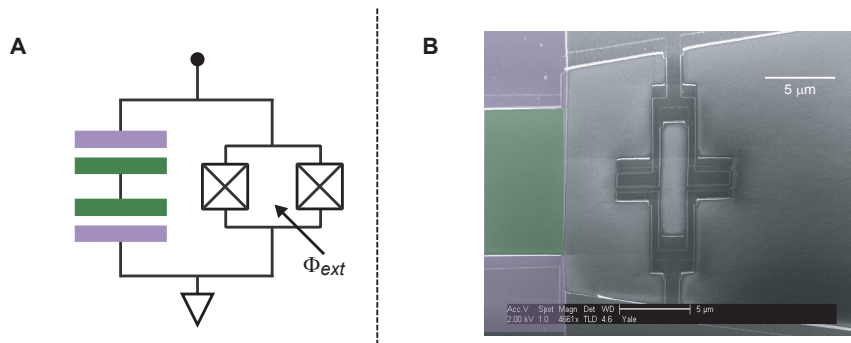


Figure 1.8: Schematic and SEM image of the JBA A) The JBA is a one port device composed of a SQUID shunted by two external capacitors in series. B) SEM image of the JBA SQUID loop. The edges of the two top plates of the shunting capacitors (purple) as well as the shared bottom plate of the capacitor (olive green) can also be seen.

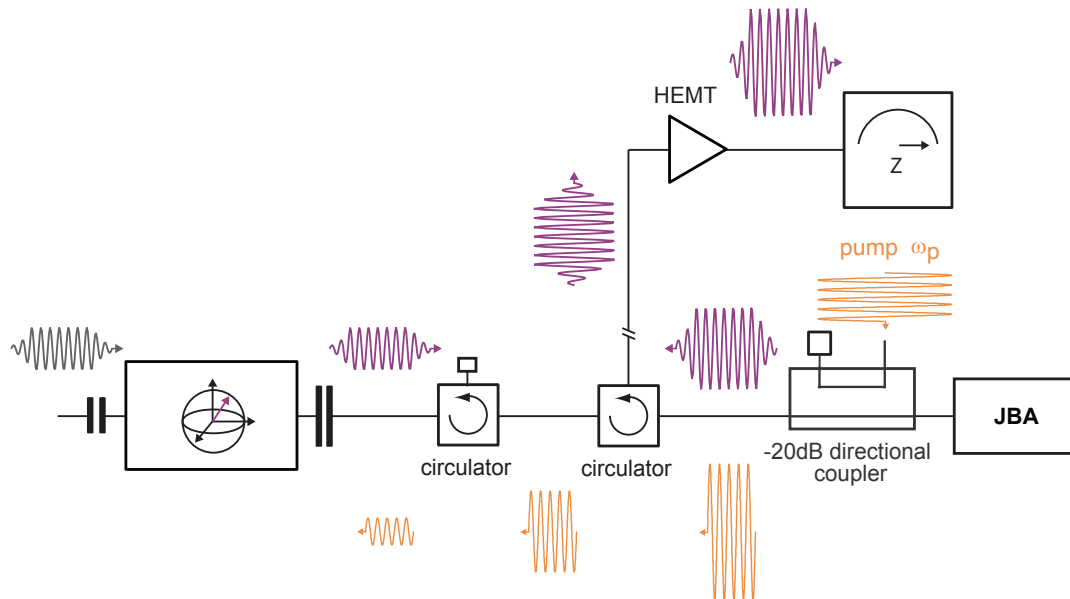


Figure 1.9: CQED Measurement with a JBA. The pump at frequency ω is applied to the JBA via the weakly coupled port of a directional coupler, where it combines with a signal from the cavity and together they enter the signal port of the amplifier. The finite reverse isolation of the circulators reduce the magnitude of the reflected pump, but does not reduce it entirely.

1.3 Double-Pumping the JBA

Removing this large pump tone and minimizing the associated qubit dephasing is the first main contribution of this work. One method for reducing the magnitude of the tone is to add extra circulators, but these circulators also come with additional loss which will further degrade the measurement efficiency. A better solution, which is supported by the four-wave mixing interaction found in the JBA, is to spectrally separate the pump tone from the cavity. The single large pump tone at ω_p can be replaced by two pump tones located at $\omega_{pump1} = \omega_p + \Delta$ and $\omega_{pump2} = \omega_p - \Delta$ (see Fig. 1.10). These pumps act as an effective pump at the so-called ghost frequency, $\omega_g = (\omega_{pump1} + \omega_{pump2})/2$, with an effective pump power which depends equally on the magnitude of both drives [56]. This pumping configuration gives the same amplifier gain, but without the a large reflected pump tone at the center of the gain curve. (see. Fig. 1.11).

If we use a double-pumped JBA as the parametric amplifier for a qubit measurement, the strong reflected pump tones now at ω_{pump1} and ω_{pump2} still propagate back toward the cavity and qubit, but the increased spectral separation means many fewer pump photons enter and contribute to unwanted and uncontrolled qubit dephasing. This can be seen by measuring the Ramsey coherence time of the qubit (See Fig. 1.12 and 1.13). The decrease in amplitude as a function of time is caused by the gradual loss of phase coherence due primarily to excess photons in the cavity. Comparing the decay times when the single-pump JBA is on and off indicates the pump adds 28 additional photons to the cavity population. In contrast, comparing the decay times for the double-pump JBA we find an increase of only 1 additional photon.

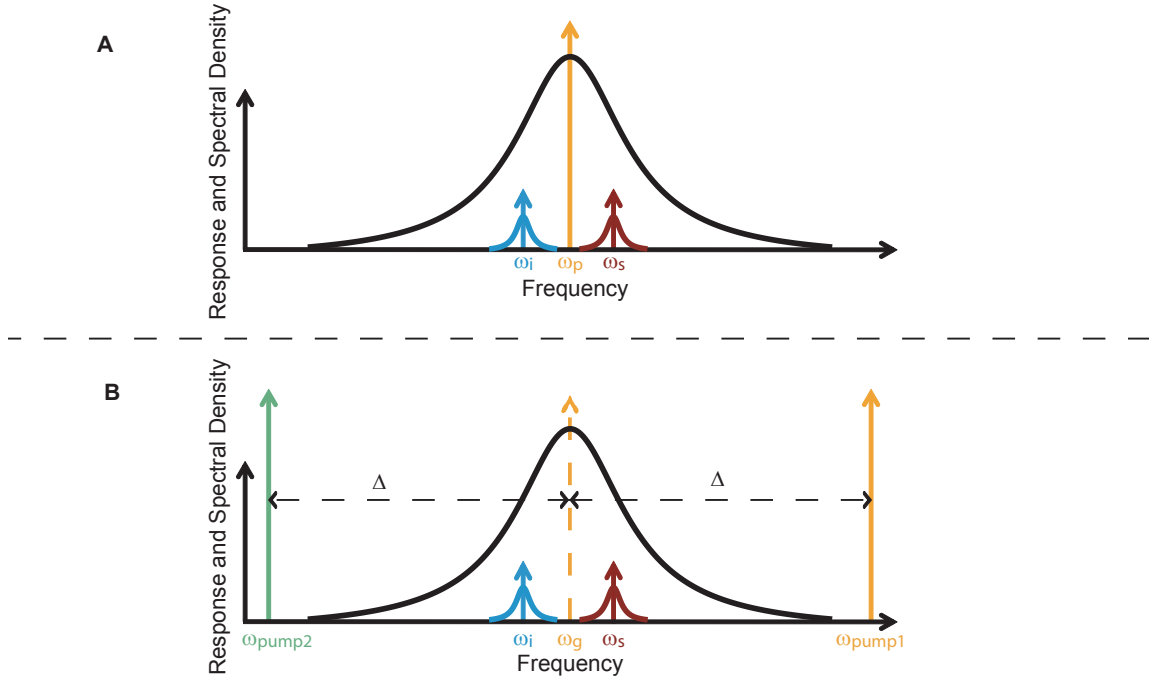


Figure 1.10: Frequency landscape of a single and double-pumped JBA. A) Frequency Schematic of a Single-Pumped JBA. The Lorentzian gain response of the JBA (black) is overlaid on the frequency location of the pump (orange) signal (maroon) and idler (blue) tones. The frequency of the pump, ω_p , corresponds to the frequency of maximum gain. If a small signal (maroon) is applied at the frequency ω_s , it will be amplified in reflection at that frequency (the bandwidth due to the modulation of that signal is represented by the thick maroon response curve) and an additional amplified copy (blue) will be produced at the idler frequency given by $\omega_i = 2\omega_p - \omega_s$. B) Frequency schematic of a double-pumped JBA. The same Lorentzian gain curve can be produced by two pumps at ω_{pump1} and ω_{pump2} . If these two pumps are uniformly detuned from the center of the desired gain curve by an amount Δ , we can think of them as one effective ghost pump (dotted orange arrow) at the center frequency ω_g . If a small signal (maroon) is applied at the frequency ω_s , it will be amplified in reflection at that frequency and an additional amplified copy (blue) will be produced at the idler frequency given by $\omega_i = \omega_{pump1} + \omega_{pump2} - \omega_s$.

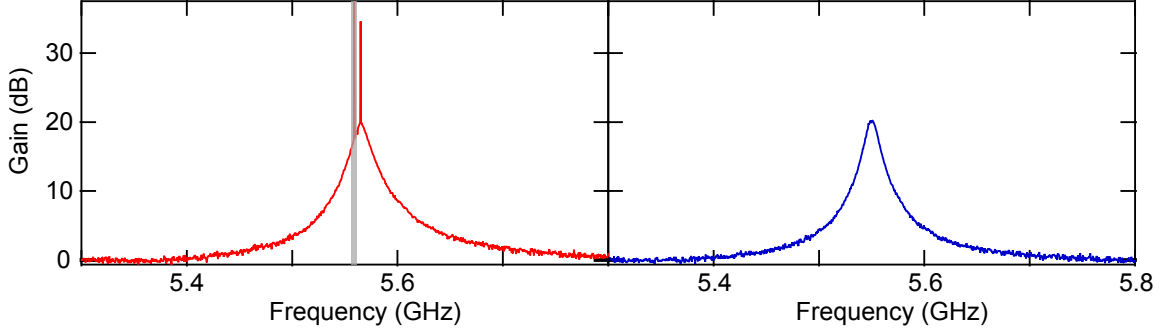


Figure 1.11: Measured 20 dB gain curves from a single-pump (red) and double-pump (blue) JBA. The single pump trace shows the large reflected pump tone at 5.565 GHz, corresponding to the point of maximum gain. The secondary spike (gray) is a mixer artifact from the VNA resulting from the large magnitude of the pump tone. The pumps for the blue trace were at 4.55 GHz and 6.55 GHz, well removed from maximum gain frequency.

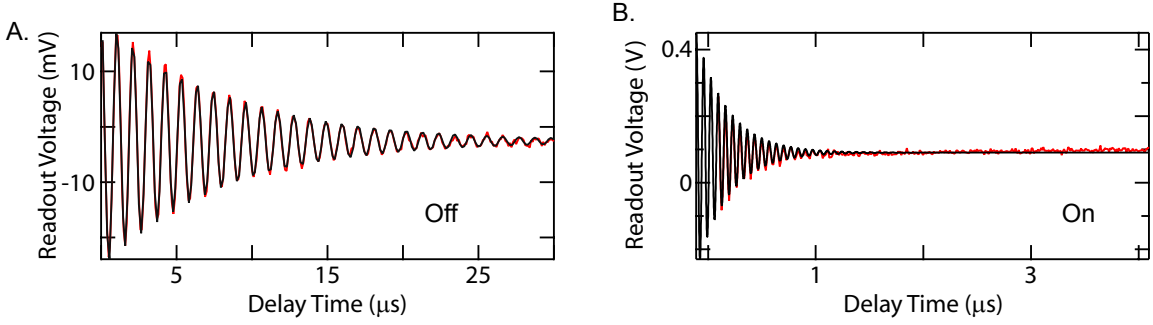


Figure 1.12: Measured Ramsey dephasing time of a qubit when amplified with a single-pumped JBA. The dephasing time without any amplification was $8 \mu\text{s}$. This decreased to 290 ns when the amplifier is turned on, corresponding to an average of 28 photons in the cavity due to the large reflected pump tone.

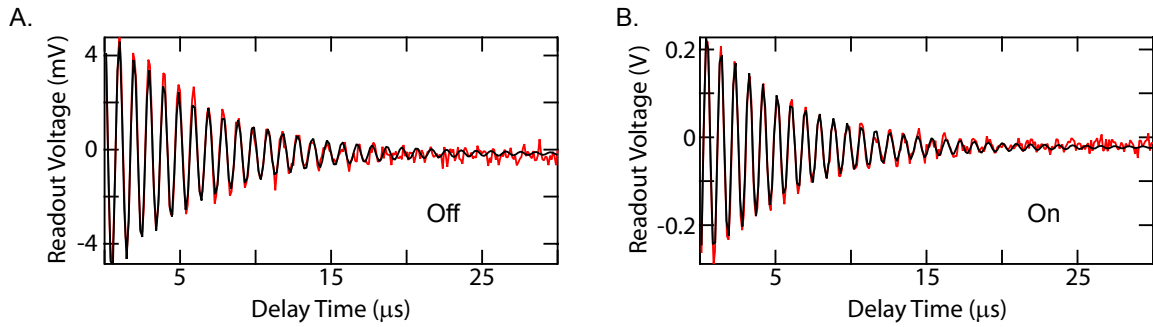


Figure 1.13: Measured Ramsey dephasing time of a qubit when amplified with a double-pumped JBA. The dephasing time without any amplification was $6.8 \mu\text{s}$, which only decreased to $5.2 \mu\text{s}$ when the amplifier was turned on, corresponding to only 1 additional photon in the cavity.

1.4 Quantum Operations

Removing the strong pump tone and associated qubit dephasing has allowed us to investigate Heisenberg back-action of the JBA. In general, the measurement process can be thought of as a series of unitary operations, together with projective measurements [1] (see Fig. 1.14). First, the cQED unitary entangles the state of the qubit Ψ with the coherent state entering the cavity $|\alpha\rangle$. Then $|\alpha\rangle$ traverses the cavity and enters the amplifier where it is subject to another unitary operation U_{amp} . The exact action of U_{amp} depends on the type of quantum limited parametric amplifier, the details of the operation such as the value of the pump phase of the amplifier relative to that of the signal, and the strength of the interaction. It may also take an additional input, here taken to be vacuum $|0\rangle$, depending on the exact details of the amplification. After the amplifier, the coherent state is measured, giving the result (I_m, Q_m) and any other output from the amplifier is typically thrown away into a cold 50Ω load. Since the qubit and the coherent state are entangled, all of the measurement operations made on the coherent state act-back on the final state of the qubit, here represented as a density matrix ρ_f . Moreover, different types of back-action can be imposed depending on the choice of the applied unitary operations.

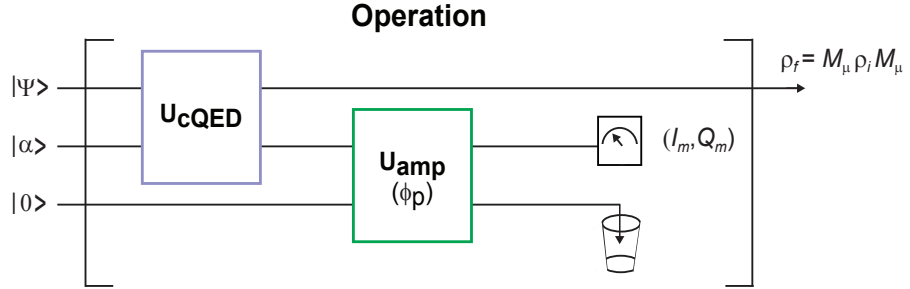


Figure 1.14: Logical Schematic of a Quantum Operation on a Qubit (top line) in Initial State Ψ . The qubit, coupled to a microwave cavity, undergoes a unitary dispersive interaction, U_{cQED} , with the incoming microwave pulse (second line) with initial state $|\alpha\rangle$, entangling qubit and microwave pulse. Subsequently, the microwave pulse enters a quantum-limited amplifier, where it undergoes a unitary operation U_{amp} . Depending on the details of the amplifier used, U_{amp} may depend on the pump phase of the amplifier ϕ_p , or some other mode of the amplifier which is taken to initially be in vacuum and later discarded. Losses after the amplifier project the output onto an outcome (I_m, Q_m) , which is used to calculate the final state of the qubit, ρ_f .

The DP-JBA is a particularly interesting amplifier for Heisenberg back-action experi-

ments. This amplifier squeezes one quadratures of the incident coherent state while amplifying the other, and by changing which quadrature is squeezed and which is amplified we can apply different U_{amp} . These different unitary operations also result in different types of back-action experienced by the qubit. If the I quadrature is amplified, the effect of the Heisenberg back-action is a stochastic walk toward the poles of the Bloch sphere. If instead the Q quadratures is amplified, the effect of the Heisenberg back-action is a stochastic rotation around the equator (see. Fig. 1.15). In either case, the magnitude of the stochastic kick depends on the strength of the measurement.

The back-action was measured by first setting the DP-JBA to give a particular U_{amp} and initializing the Bloch vector of the qubit to point along the $+y$ direction. Then a variable strength measurement is made of the coherent state, resulting in the outcome (I_m, Q_m) . Lastly, tomography is performed to measure the resulting qubit state $\langle X \rangle_c$, $\langle Y \rangle_c$, and $\langle Z \rangle_c$. This was repeated 10^6 times for each U_{amp} , the histograms of the coherent state measurements as all of the final qubit state information correlated to the corresponding coherent state measurement outcome are shown in Fig. 1.16. Both the character of U_{amp} , and the strength of the measurement were varied. The strength of the measurement is controlled by changing \bar{n} , but parametrized by the average center of the measured histogram \bar{I}_m normalized by the width of the measured histogram along the I direction σ_I when the I quadrature is amplified. Since \bar{I}_m increases linearly with increasing $|\alpha|$ while the width does not change, \bar{I}_m/σ_I is an easily measurable stand in for \bar{n} .

For weak interactions when the I quadrature is amplified (Fig. 1.16 A.), the qubit remains pointed along the $+y$ direction, and as the interaction strength increases the qubit moves toward the poles as indicated by the decay of deep red in the $\langle Y \rangle_c$ tomogram and the development of blue and red sections in the $\langle Z \rangle_c$ tomogram. This becomes the most evident for the strongest interaction strengths where the final qubit state is given by $z = \pm 1$, with the sign given by the final I_m value. If instead the Q quadrature is amplified (Fig. 1.16 B.), we see colored fringes develop in the $\langle X \rangle_c$ and $\langle Y \rangle_c$ tomograms representing the stochastic rotation around the equator. $\langle Z \rangle_c$ does not develop a definite color for any measurement strength, indicating that the Heisenberg back-action is fundamentally different for this U_{amp} . For a perfectly efficient measurement, as the measurement strength increases the frequency

of the fringe should increase but the amplitude should stay at 1. The amplitude of the measured fringes, particularly for the strongest measurement strengths is much smaller, indicating we have $\eta < 1$. One of the main limitations on η are losses between the cavity and the amplifier, which the second and third main contribution to this thesis will address.

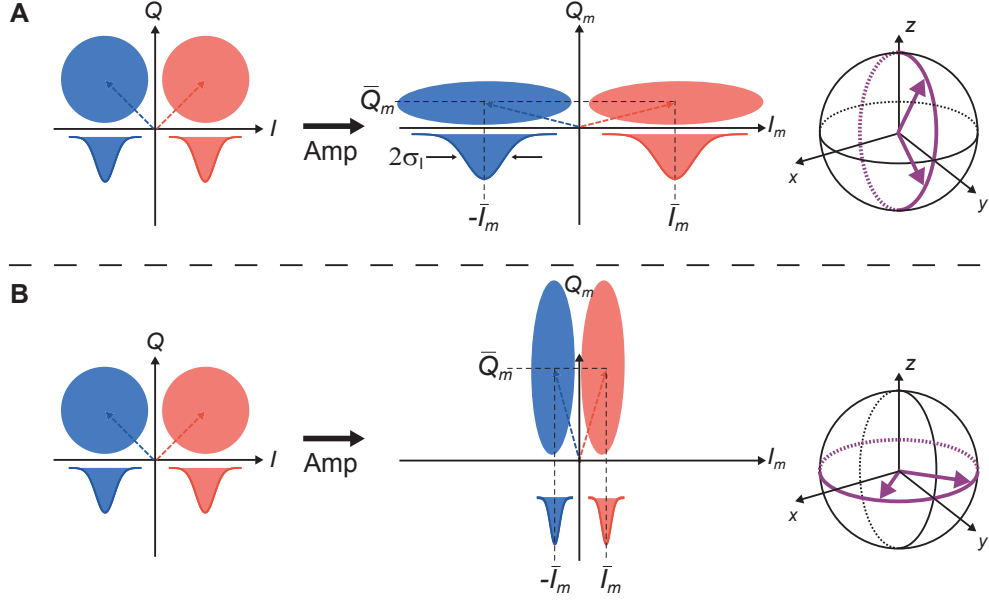


Figure 1.15: Heisenberg back-action of the double-pumped JBA. Due to the nature of U_{amp} applied by the double-pumped JBA the cavity state after the amplifier goes from circles to ellipses. The quadrature along which the noise is decreased depends on phase of the pump relative to that of the cavity. On the right is the Bloch sphere representation of the measurement back-action for these two different kinds of measurements. If the noise is amplified along the I quadrature (A) the qubit experiences a stochastic kick along lines of longitude, with the projection of the kick along z encoded in I_m . If instead the noise is amplified along the Q quadrature (B), The qubit experiences a stochastic kick along lines of latitude, with the angle of the kick encoded in Q_m . This is representative of the non-trivial types of Heisenberg back-action that can be observed after other unwanted types of back-action are well controlled and minimized.

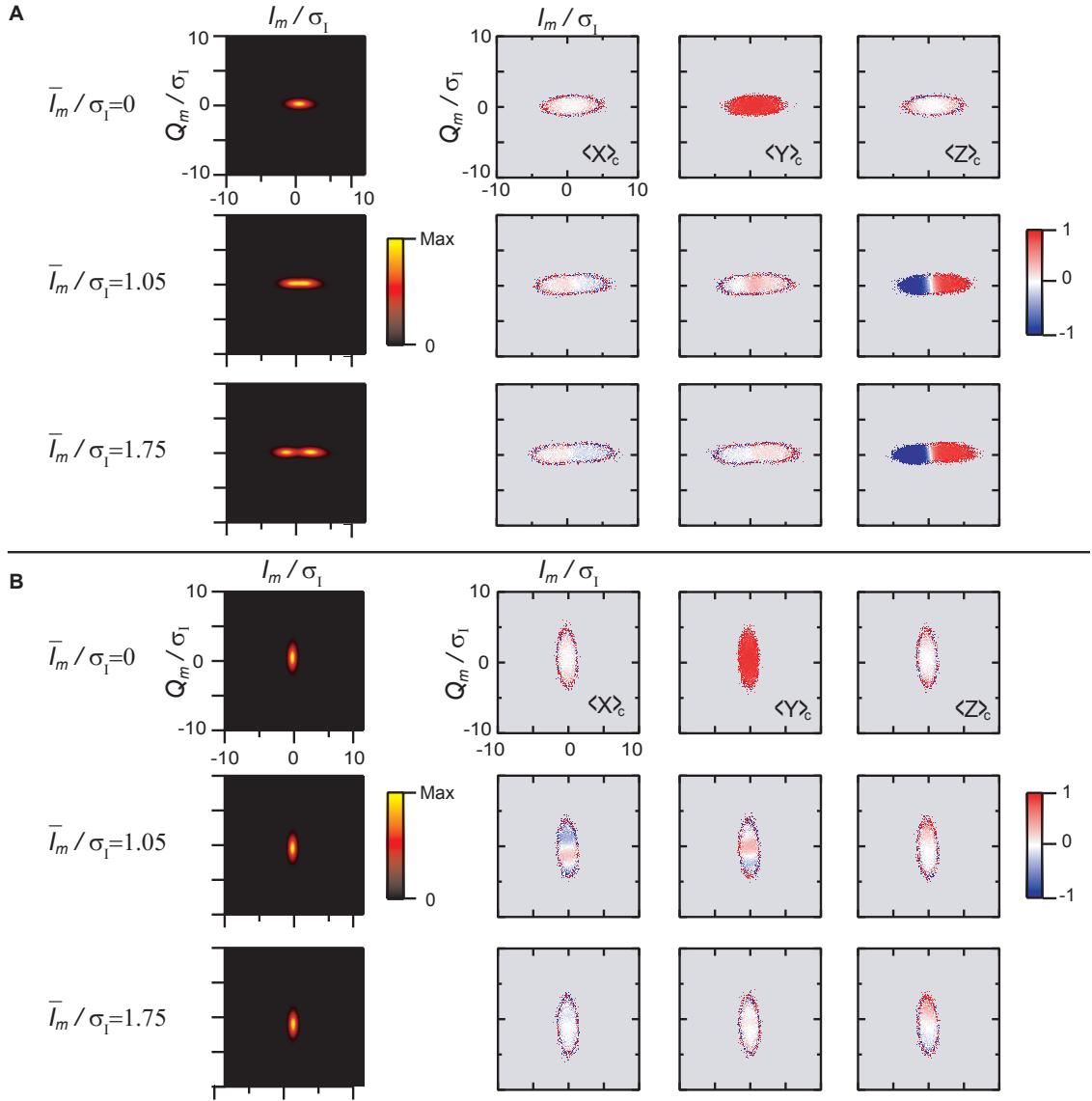


Figure 1.16: Measured Heisenberg back-action of the DP-JBA A) Experimental outcomes for amplification along the I -quadrature. The left column shows (I_m, Q_m) histograms, with the color plotted on a log scale for visibility, for three different measurement strengths (\bar{I}_m/σ_I). The right three columns are tomograms showing, for the same measurement strengths, conditional maps of $\langle X \rangle_c$, $\langle Y \rangle_c$, $\langle Z \rangle_c$ versus (I_m, Q_m) . The static value of the $\langle X \rangle_c$ measurement tomograms, as well as the decay in the $\langle Y \rangle_c$ tomograms and the color gradient that develops in the $\langle Z \rangle_c$ tomograms is consistent with qubit evolution along lines of longitude. B) Experimental outcomes for amplification along the Q -quadrature. The stochastic Ramsey fringes in the $\langle X \rangle_c$ and $\langle Y \rangle_c$ tomograms, along with no evidence of projection in the $\langle Z \rangle_c$ tomograms for even the highest measurement strengths, indicate an operation is being performed that is fundamentally not a measurement. These results are consistent with the qubit evolving along lines of latitude. Due to finite measurement efficiency, the contrast of the fringes is reduced, leading to the lack of visible fringes at $\bar{I}_m/\sigma_I = 1.75$.

1.5 The Josephson Circulator

A large source of loss between the cavity and the parametric amplifier is a microwave element known as the circulator. Circulators are non-reciprocal devices which transfer signals from port 1 to port 2 to port 3, while blocking anything from transferring in the other direction. They must be included in any measurement protocol involving a parametric amplifier which operates in reflection, both to separate the input and the output and to prevent qubit dephasing back-action due to the reflected signal tone. Commercial circulators rely upon Faraday rotation, or the non-reciprocal interaction between electromagnetic signals and magnetic fields. Not only are the circulators themselves lossy, but the strong magnetic fields needed to provide this Faraday rotation can also lead to qubit decoherence, requiring the circulators to be physically isolated from the qubit and cavity. This in turn requires extra cables and connectors, all of which also include some losses and thus also reduce our measurement efficiency. The second main contribution of this work is the realization of a Josephson microwave circulator. This device, based upon the JPC, is theoretically loss-less and does not require large magnetic fields to achieve non-reciprocity.

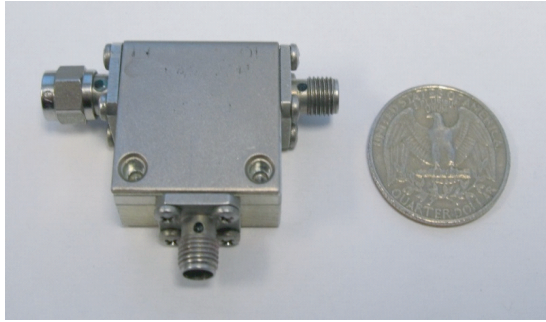


Figure 1.17: Photograph of a Pamtech commercial 4-8 GHz circulator. Commercial microwave circulators are large (a quarter has been included for scale), lossy, and rely on a strong and permanent magnetic field, making them challenging to integrate into experiments with superconducting qubits.

The Josephson circulator relies on a second type of three-wave parametric process supported by the JPC known as unity-gain photon conversion [29, 35]. This mode of operation, realized by applying a pump to one mode, say c , at the frequency difference of the other two ($\omega_p = \omega_a - \omega_b$), results in an interaction in which photons from mode a are coherently converted into photons of mode b and vice versa. The process is characterized by the photon

conversion coefficient at zero detuning C , which ranges from 0 (no-conversion), where no photons are converted and the JPC acts as a perfect reflector, to 1 (full-conversion) where signal and idler photons are exchanged one for one.

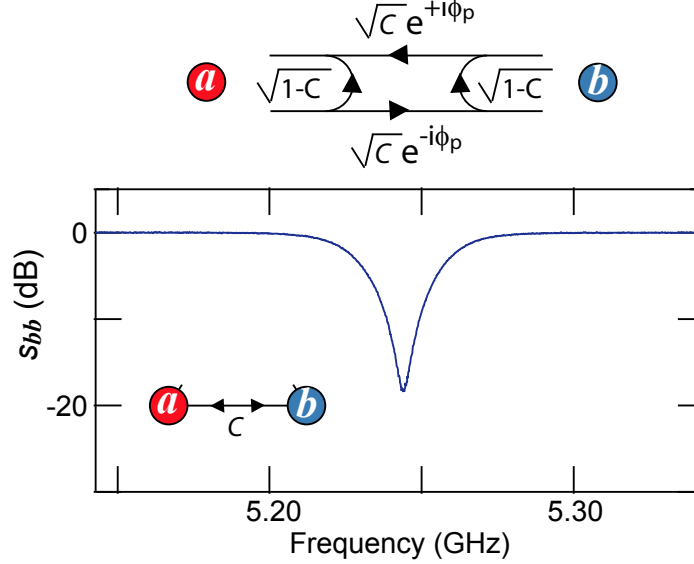


Figure 1.18: Unity Photon Gain Conversion in the JPC. Here, modes a and b are coupled by a pump applied to mode c at frequency $\omega_a - \omega_b$. The graph representation of the scattering matrix is shown at the top, and the measured s_{bb} is plotted versus probe frequency below. s_{bb} shows a -18 dB dip at ω_b where photons have been converted from ω_b to ω_a with conversion efficiency $C = 0.98$.

Typically, the JPC is used exclusively as a parametric amplifier or as a coherent photon converter. These functionalities are realized by coupling only one pair of modes at a time, via only one parametric process at a time. But the JPC is not limited to this. Following a method proposed by Ranzani et al. [57], we can calculate the effects of coupling multiple pairs of modes simultaneously via different types of coupling. If we couple all three pairs of modes via full coherent conversion processes (see Fig. 1.19), and properly set all of the pump phases to realize a total pump phase of $\phi_{tot}^{circ} = \pi/2$ we arrive at the following scattering matrix

$$|S_{circ}| = \begin{bmatrix} 0 & 1 & 0 \\ 0 & 0 & 1 \\ 1 & 0 & 0 \end{bmatrix}$$

which is identical to that of a ideal circulator [58].

Figure 1.20 shows the measured scattering parameters of an experimental realization of such a device, with individual conversion coefficients of 0.97, 0.98, and 0.99, and the calculated scattering coefficients for those values of individual conversion coefficient superimposed. This implementation of a microwave circulator removes the large magnetic field of a traditional circulator, and is fabricated via methods compatible with those of superconducting qubits. This means it could be physically located much closer to the qubit and cavity, and the three could even be fabricated on the same chip. This would also remove the loss from the cables and connectors which are currently needed to connect the cavity to the isolated traditional microwave circulator. Furthermore, the direction of circulation is in-situ reversible simply by changing the total pump phase, making it a more versatile device.

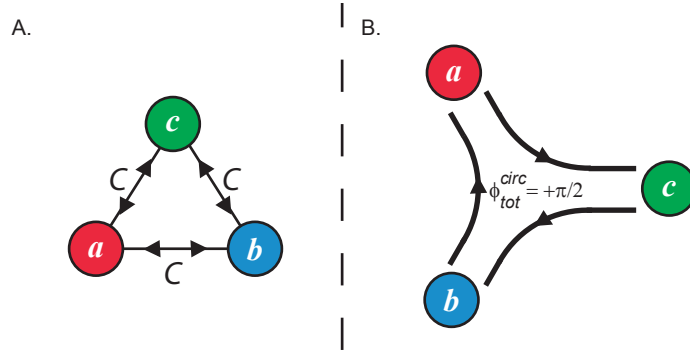


Figure 1.19: Pump Configuration (A) and Graphical Scattering Matrix (B) for the Josephson Circulator. Linking all pairs of modes via conversion processes realizes a clockwise circulator when the total pump phase $\phi_{total}^{circ} = \pi/2$.

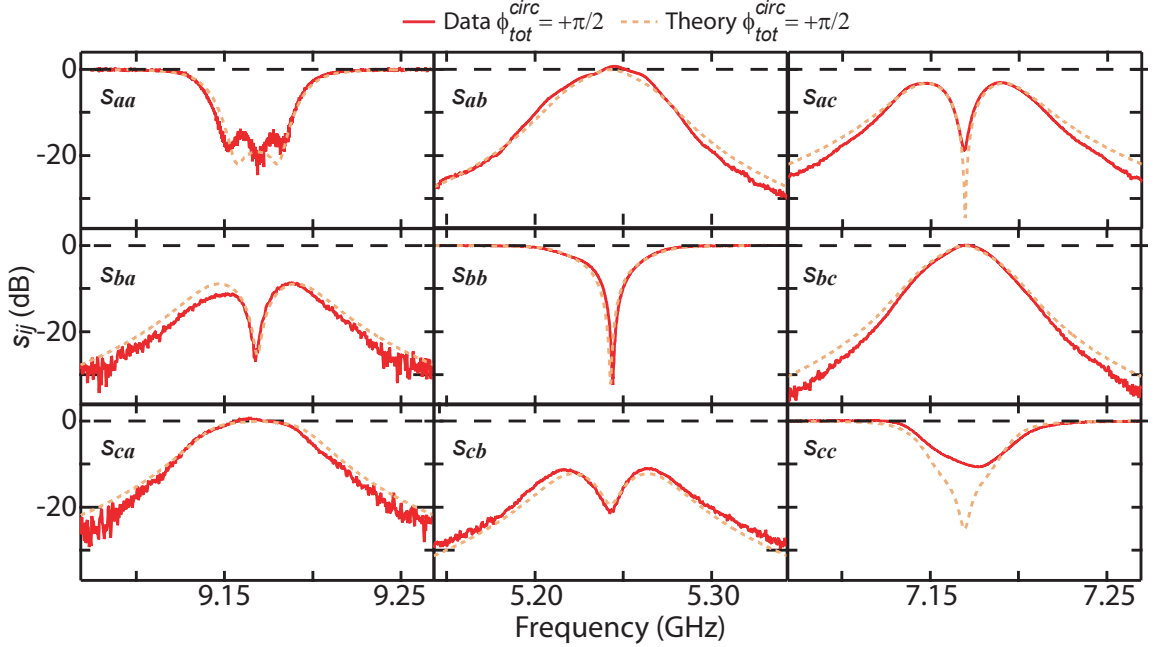


Figure 1.20: Measured circulator scattering parameters versus frequency for $\phi_{tot}^{circ} = \pi/2$ (red) along with superimposed theory (dashed yellow) for the Josephson circulator. The device has 1 dB insertion loss and -10.5 dB isolation over an 11 MHz bandwidth.

1.6 The Josephson Directional Amplifier

We could eliminate the circulators entirely if our parametric amplifiers were directional. An ideal directional amplifier would maintain all of the desirable quantities of a quantum limited parametric amplifier: adding no non-Heisenberg noise, having sufficient gain to minimize the non-Heisenberg noise of the HEMT, while additionally amplifying in one direction and attenuating in the other. This would minimize the back-action both from the amplifier itself, and from any other signals propagating backward from the measurement apparatus. As with the circulator, if we could fabricate a directional amplifier on-chip with our cQED system we could even further increase the measurement efficiency of our systems by removing the cables and connectors between the two, while minimizing the physical size of the experiment (see Fig. 1.21).

The third main contribution of this thesis is such a directional amplifier. The Josephson directional amplifier (JDA) is realized by coupling two pairs of modes of a JPC via parametric gain processes, and coupling the third pair of modes via a coherent conversion

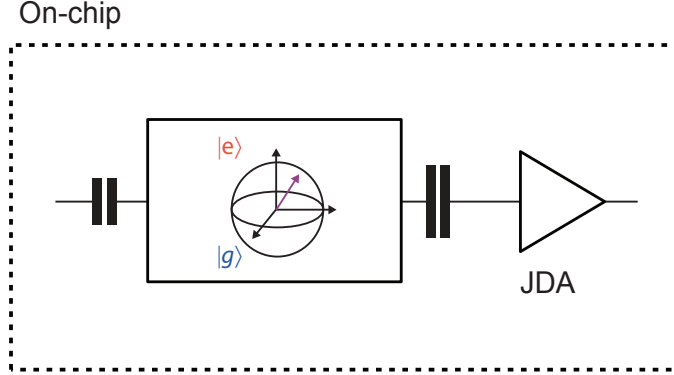


Figure 1.21: Schematic of the use of an on-chip directional amplifier. The goal is to be able to create qubits, cavities, and a directional amplifier on the same chip using the same fabrication methods. This will serve to both reduce losses before the first stage of amplification, leading to a reduction in qubit dephasing, and to greatly reduce the size of experiments. Currently, directional amplifiers such as HEMTs, and directional signal routing devices such as circulators use technologies that can not be directly implemented ‘on-chip’ with superconducting qubits.

process [57, 58]. Calculating the response of the device on resonance for two equal single pump gains G , full conversion $C = 1$, and an appropriate choice of the total pump phase $\phi_{tot}^{d-a} = \pi/2$ we find

$$|S_{da}| = \begin{bmatrix} 0 & \sqrt{G} & \sqrt{G-1} \\ 1 & 0 & 0 \\ 0 & \sqrt{G-1} & \sqrt{G} \end{bmatrix}$$

We can label the ports as the Signal (S) input, Idler (I) input, and Vacuum (V) input based upon the role each one plays. Signals incident on S correspond to the directional amplifier input, while signals exiting I form its output. The S port is matched (no power reflects), and incident power is instead transmitted with gain to the I and V ports. Signals incident on the V port are noiselessly and directionally transmitted through the device to the S port with unity photon gain. Any device must necessarily reflect, at a minimum, vacuum fluctuations back to the upstream signal source. In our implementation the source of these fluctuations would be provided by the cold 50Ω load terminating the V port. Furthermore, the unity-gain transmission of signals from the V to the S port follows from the combined requirements of quantum-limited amplification (sending it to I would degrade the noise performance of the device) and the information conserving nature of the device

(no entropy is produced since we assume there is no dynamical coupling between the amplitude of the signal and the amplitude of the pump, i.e. the pump is perfectly stiff [33]). Changing ϕ_{tot}^{d-a} by π flips which physical port plays the role of S and V, with I remaining unchanged. The roles can be further re-mapped by changing which pair of modes is linked via conversion and thus, in general, each of the three physical ports can play each role. We note that combining two gain processes with gain G yields a directional amplifier with gain G , not G^2 . The combined operation should be thought of as rerouting the outputs of one port of a non-directional amplifier (from S to V) rather than as two independent stages of amplification.

Figure 1.23 shows the measured scattering parameters of an experimental realization of this device, with individual pairwise gain processes $G = 12$ dB and $G = 13$ dB, and with an individual pairwise conversion process of $C = 0.998$. Here \mathbf{a} plays the role of the signal, \mathbf{b} plays the role of the idler and \mathbf{c} plays the role of the vacuum. The device shows 14 dB of gain over an 11 MHz bandwidth.

This is not the only Josephson junction based directional amplifier. Other implementations include voltage-biased DC-SQUIDS [59–63], non-linear superconducting transmission lines [22, 64–68], and coupled JPCs [33, 69], but these proposals generally rely upon careful matching of parameters, phase-matching conditions, or do not have the same noise performance.

The Josephson directional amplifier has good prospects for on-chip integration due to the compatibility of the operation and fabrication process with those used for superconducting qubits. This could improve the measurement efficiency of our experiments, and correspondingly our ability to investigate and control the Heisenberg back-action, due to the removal of lossy connectors, cables, and traditional microwave circulators from the setup. Furthermore, since the only difference between the directional amplifier and the Josephson circulator are the frequency and power of the microwave pumps applied at room temperature, we envision a future where a network of connected JPCs could form an incredibly versatile gain and circulation medium which could be invaluable in designing and controlling the types of Heisenberg mediated operations we would like to be able to implement.

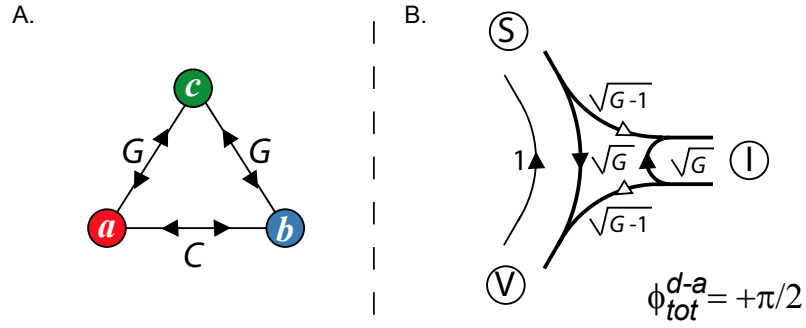


Figure 1.22: Schematic of pump configuration and graphical scattering matrix for the Josephson directional amplifier A) Schematic of pump configuration for the directional amplifier: two pairs of modes are coupled pairwise via gain processes and the third via unity-gain photon conversion. B) Graphical representation of the scattering matrix for a total pump phase $\phi_{tot}^{d-a} = \pi/2$: the three ports are named for the roles they perform in the amplification process. The signal (S) port serves as the directional amplifier input and is combined with the idler (I) port, which corresponds to the directional amplifier output. The vacuum (V) port does not participate in amplification but instead is transmitted with unity gain back to the signal port. For clarity, all zero amplitude scattering parameters are omitted. The unfilled arrows denote transmission of signals with phase conjugation. Flipping ϕ_{tot}^{d-a} to $-\pi/2$ or switching which pair of modes are connected via gain and conversion processes, changes which physical mode of the JPC plays which role in the directional amplifier.

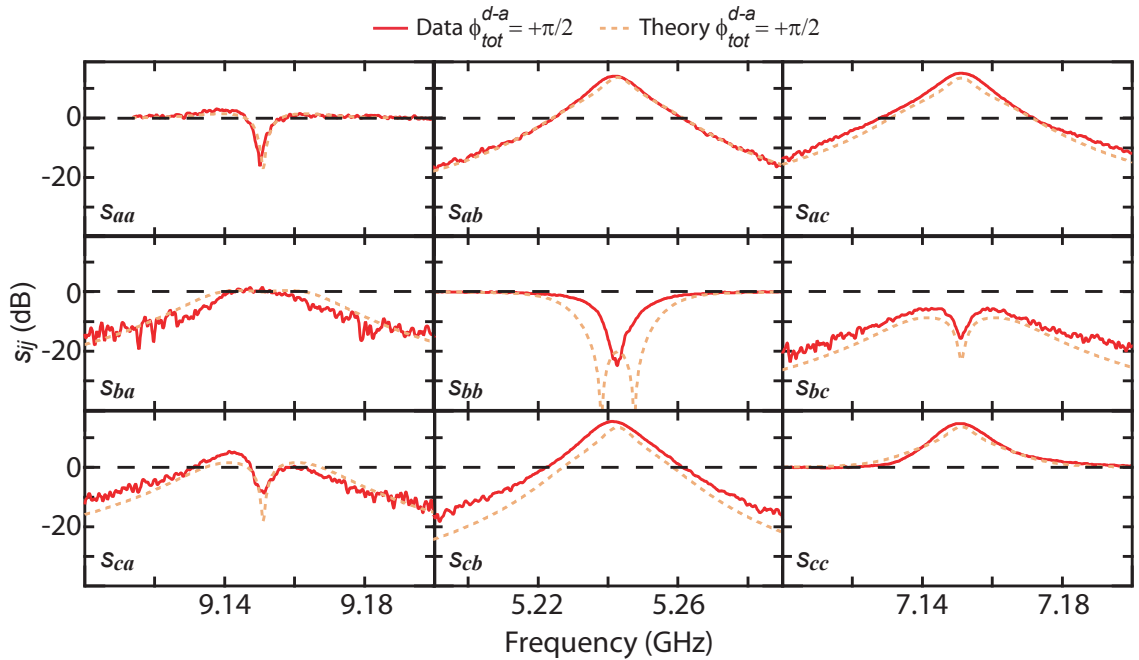


Figure 1.23: Measured directional amplifier scattering parameters versus frequency for $\phi_{tot}^{d-a} = \pi/2$ (red) along with superimposed theory (dashed yellow). The amplifier shows 14 dB of gain and an 11 MHz bandwidth.

1.7 Perspectives

This thesis presents three improvements to superconducting qubit measurement apparatuses in order to minimize effects which limit our ability to manipulate qubits by the Heisenberg back-action of measurement. Some of these improvements, such as double-pumping the JBA, have already been implemented within a superconducting qubit experiment and used to measure new effects. Others, such as replacing traditional microwave circulators with Josephson circulators or by replacing reflection-based parametric amplifiers with Josephson directional amplifiers have not, and improvements to the measurement efficiency have not been demonstrated. Improvements such as these will help enable new levels of qubit control and manipulation via Heisenberg back-action.

This work also paves the way for more complicated and efficient signal routing architectures. The Josephson circulator and the Josephson directional amplifiers are both realized with the same circuit, and the role that circuit plays can be changed in-situ just by changing the microwave pumping conditions. Several such tessellated circuits could form a truly quantum, in-situ re-routable, switch matrix/gain medium for superconducting qubits.

Chapter 2

Coherent Amplification and Conversion with Josephson Parametric Devices

Coherent amplification and frequency conversion are the two fundamental parametric processes which underlie every device which will be discussed in this thesis. They are both multi-wave mixing processes involving a pump tone, a signal tone, and an idler tone ¹. In parametric amplification, pump photons are converted into pairs of signal and idler photons, and in parametric conversion signal photons are converted into idler photons (and vice versa) through an interaction which is mediated by the pump. Although we will focus on those parametric processes arising in Josephson junctions, these phenomena are quite general and can be generated in a variety of physical systems ranging from the cochlea in the inner ear of mammals [70,71] to optical fibers [72]. Even within the class of parametric devices based on Josephson junctions there exists a substantial diversity. Some devices are based around the non-linearity of a single junction [73], while others involve two, three or even four junctions in a loop [30, 74, 75], and even larger arrays of junctions [22, 76].

1. More correctly, the signal and idler are wave packets and are not strictly speaking monochromatic. The signal and the idler have typically finite bandwidths which are on the order of MHz and which are set by the readout speed of the qubit. Even the pump tone as produced by a generator is not truly monochromatic, although the bandwidth of the pump is typically nine orders of magnitude smaller than that of the signal and the idler.

We can bring order to the variety of different implementations by classifying parametric devices by several basic characteristics. One axis of classification is based on physical characteristics of the device: how many modes or physical ports the device has, or what degree of non-linearity gives rise to amplification. Another axis is based on how they are operated: how they handle the two quadratures of the input signal, or whether they operate in reflection or not. This chapter explains some of the common classifications of parametric amplifiers, and presents the two parametric amplifiers that are a focus of this thesis, the Josephson bifurcation amplifier (JBA) and the Josephson parametric converter (JPC).

2.1 Classification of Parametric Devices

2.1.1 Non-Degenerate vs Degenerate

The first axis of classification depends on the device hardware. The eigenvectors which result from the diagonalization of the quadratic form associated with the Hamiltonian of the circuit define set of normal modes. If the signal tone and idler tone both excite different normal modes of the circuit, the device is known as non-degenerate. If the two excite the same normal mode, then the device is degenerate (see. Fig. 2.1). We can further break the degenerate amplifiers down into two sub-classes, singly-degenerate and doubly-degenerate. Singly-degenerate devices are circuits in which only the signal and the idler excite a single normal mode of the circuit, while while doubly-degenerate devices have the signal, idler, and pump tones all excite the same normal circuit mode ². Thus, higher levels of degeneracy correspond to fewer normal modes of the circuit. Each circuit is also interfaced with a set of physical ports which allow for incoming and outgoing tones. If multiple tones use the same physical port the circuit is known as spatially degenerate. There is often a link between the number of physical ports and the number of normal modes, but this is not always the case.

². Singly-degenerate paramps are less common than either non-degenerate or doubly-degenerate devices. The flux driven JPA [74, 77–79] is an example of such a device. This amplifier is composed of a SQUID shunted by a capacitor exactly like a JBA or JPA, but instead of being pumped with a microwave tone applied to the same input port as the signal (as will be described later in this chapter), the device is pumped by modulating the flux through SQUID.

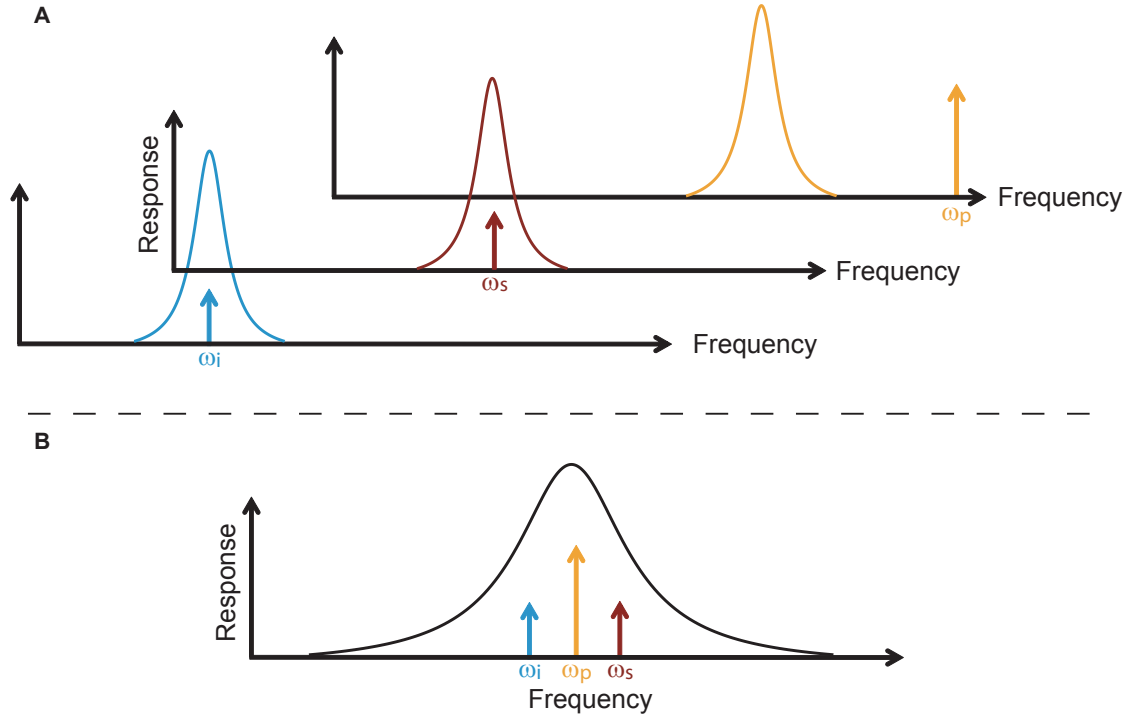


Figure 2.1: Non-degenerate and degenerate parametric amplifiers. A) Non-degenerate device. The circuit has at least three well-separated modes, whose response is represented by the Lorentzian curves, one of which is excited by the signal, and one of which is excited by the idler. (The third is excited by the pump). The circuit is also spatially non-degenerate, as all tones also enter and exit on a different physical ports represented by the different sets of axis. B) Degenerate device. The signal and idler are both associated with the same normal mode of the circuit, given by the single black Lorentzian curve. This example is actually doubly-degenerate since the pump also excites the same mode as the other two tones. The device is also spatially degenerate since tones also enter and exit on a single physical port represented by the single axis.

2.1.2 Phase-sensitive vs Phase-preserving

Another manner to classify parametric amplifiers is based on how one typically operates them to process the incoming quadratures of a signal. Incoming and outgoing signals will correspond to incoming and outgoing wave packets propagating along a transmission line.

Definition of the Field Operators and Photon Amplitude Operators

Care must be taken to properly define these types of signals quantum mechanically in both the time and the frequency domain. Following [75] we can start from the classical

propagating incoming and outgoing wave amplitudes along a transmission line

$$A_{in,out} = \frac{1}{2} \left(\left(1/\sqrt{Z_c}\right) V(x, t) \pm \sqrt{Z_c} I(x, t) \right) \quad (2.1)$$

where Z_c is the characteristic impedance of the transmission line, $V(x, t)$ is the voltage across the line and $I(x, t)$ is the current along the line. In a segment of transmission line, the time and spatial indices of the wave amplitude are not independent (see for example Appendix 1 of [33]), so we will only list the time index. The wave can also be described quantum mechanically, by making the transformation to the wave amplitude operator $A_{in,out}(t) \rightarrow \mathcal{A}_{in,out}(t)$. The wave amplitude operator has the Fourier transform

$$\mathcal{A}_{in,out}[\omega] = \frac{1}{\sqrt{2\pi}} \int_{-\infty}^{\infty} \mathcal{A}_{in,out}(t) e^{i\omega t} dt \quad (2.2)$$

which lets us define the field ladder operators

$$\mathbf{a}_{in,out}[\omega] = \frac{1}{\hbar|\omega|/2} \mathcal{A}_{in,out}[\omega] \quad (2.3)$$

where $\mathbf{a}_{in,out}[\omega]^\dagger = \mathbf{a}_{in,out}[-\omega]$. These field operators satisfy the commutation relations

$$[\mathbf{a}_{in,out}[\omega_1], \mathbf{a}_{in,out}[\omega_2]] = \text{sgn}(\omega_1 - \omega_2) \delta(\omega_1 + \omega_2) \delta_{in,out} \quad (2.4)$$

and the anti-commutator relation

$$\langle \{\mathbf{a}_{in}[\omega_1] \mathbf{a}_{in}[\omega_2]\} \rangle = 2\mathcal{N}_{in}^{\mathbf{a}} \left(\frac{\omega_1 - \omega_2}{2} \right) \delta(\omega_1 + \omega_2) \quad (2.5)$$

where $\mathcal{N}_{in}^{\mathbf{a}}[\omega] = \frac{\text{sgn}[\omega]}{2} \coth\left(\frac{\hbar\omega}{2k_B T}\right)$ is the photon spectral density of the incoming field. We can now define the quadrature operators for the incoming and outgoing field by $\mathbf{I}_{in,out} = (\mathbf{a}_{in,out} + \mathbf{a}_{in,out}^\dagger)/2$ and $\mathbf{Q}_{in,out} = (\mathbf{a}_{in,out} - \mathbf{a}_{in,out}^\dagger)/(2i)$.

The relationship $\mathbf{a}_{in,out}[\omega]^\dagger = \mathbf{a}_{in,out}[-\omega]$ leads to a surprise when returning to the time

domain. The Fourier transform of $\mathbf{a}_{in,out}[\omega]$ given by

$$\mathbf{a}_{in,out}(t) = \frac{1}{\sqrt{2\pi}} \int_{-\infty}^{\infty} \mathbf{a}_{in,out}[\omega] e^{-i\omega t} d\omega \quad (2.6)$$

is a hermitian operator. It is tempting to treat the two sides of the frequency axis separately,

$$\begin{aligned} \mathbf{a}'_{in,out}(t) &= \frac{1}{\sqrt{2\pi}} \int_0^{\infty} \mathbf{a}_{in,out}[\omega] e^{-i\omega t} d\omega \\ (\mathbf{a}'_{in,out}(t))^\dagger &= \frac{1}{\sqrt{2\pi}} \int_{-\infty}^0 \mathbf{a}_{in,out}[\omega] e^{-i\omega t} d\omega \end{aligned} \quad (2.7)$$

and think of $\mathbf{a}'_{in,out}(t)$ and $(\mathbf{a}'_{in,out}(t))^\dagger$ as the amplitude of the traveling photon flux in the wave packet, but then the commutation relationship in the time domain is given by

$$[\mathbf{a}'_{in,out}(t_1), \mathbf{a}'_{in,out}(t_2)^\dagger] = \left(\frac{1}{2} \delta(t_1 - t_2) + \frac{i}{2\pi} p.p. \left(\frac{1}{t_1 - t_2} \right) \right) \delta_{in,out} \neq \delta(t_1 - t_2) \delta_{in,out} \quad (2.8)$$

To remedy the above commutation relationship and properly define the photons of the traveling signals we can define the photon amplitude operators by using a wavelet basis. Wavelets are functions which form a basis for realistic signals (signals with finite energy), where each individual wavelet $w_{in,out}^{mp}(t)$ such that $w_{in,out}^{mp}(t)^* = w_{in,out}^{-mp}(t)$ is characterized by two indices, $(|m|, p)$ which correspond to the center of the function in frequency-time space. They obey the following orthogonality relations:

$$\int_{-\infty}^{+\infty} dt w_{in,out}^{m_1 p_1}(t) w_{in,out}^{m_2 p_2}(t)^* = \delta_{m_1, m_2} \delta_{p_1, p_2} \delta_{in,out} \quad (2.9)$$

$$\sum_{m=-\infty}^{+\infty} \sum_{p=-\infty}^{+\infty} w_{in,out}^{mp}(t_1) w_{in,out}^{-mp}(t_2) = \delta(t_1 - t_2) \quad (2.10)$$

Shannon wavelets are typically used, but other bases also exist [80]. We can now define the

photon ladder operator, $\psi_{in,out}^{mp}$, by

$$\psi_{in,out}^{mp} = \int_{-\infty}^{+\infty} d\tau w_{in,out}^{mp}(\tau) \mathbf{a}_{in,out}(\tau) \quad (2.11)$$

$$\psi_{in,out}^{-mp} = (\psi_{in,out}^{mp})^\dagger \quad (2.12)$$

It should be noted that this transformation is typically (see for example [34,81]) only taken over a restricted frequency range under the assumptions of the rotating wave approximation, but this is not strictly necessary [75].

These photon ladder operators satisfy the commutation relation

$$\begin{aligned} [\psi_{in,out}^{m_1 p_1}, (\psi_{in,out}^{m_2 p_2})^\dagger] &= \int_{-\infty}^{+\infty} \int_{-\infty}^{+\infty} dt_1 dt_2 w_{in,out}^{m_1 p_1}(t_1) w_{in,out}^{m_2 p_2}(t_2)^* [\mathbf{a}_{in,out}(t_1), \mathbf{a}_{in,out}(t_2)] \\ &= \delta(m_1 - m_2) \delta(p_1 - p_2) \delta_{in,out} \end{aligned} \quad (2.13)$$

as desired. The photon-number operator for the wave packet is given by $(\psi_{in,out}^{mp})^\dagger \psi_{in,out}^{mp}$.

Phase-sensitive and Phase-preserving Amplification

An ideal amplifier would treat both quadratures of the incoming signal equally, and would add no noise of its own. Unfortunately, as we will see, this situation is not allowed by quantum mechanics. Quantum mechanics mandates that the commutation relationship given in Eqn. 2.4 must be maintained for both the incoming and outgoing field operators. If both quadratures are amplified identically by the amplifier and no noise is added then $I_{out} = \langle \mathbf{I}_{out} \rangle = \sqrt{G} \langle \mathbf{I}_{in} \rangle$ and $Q_{out} = \langle \mathbf{Q}_{out} \rangle = \sqrt{G} \langle \mathbf{Q}_{in} \rangle$ or equivalently $\mathbf{a}_{out} = \sqrt{G} \mathbf{a}_{in}$ and $\mathbf{a}_{out}^\dagger = \sqrt{G} \mathbf{a}_{in}^\dagger$. But, if we take $[\mathbf{a}_{in}[\omega_1], \mathbf{a}_{in}[\omega_2]^\dagger] = \text{sgn}(\omega_1 - \omega_2) \delta(\omega_1 + \omega_2)$ then we find $[\mathbf{a}_{out}[\omega_1], \mathbf{a}_{out}[\omega_2]^\dagger] = G \text{sgn}(\omega_1 - \omega_2) \delta(\omega_1 + \omega_2) \neq \text{sgn}(\omega_1 - \omega_2) \delta(\omega_1 + \omega_2)$.

There are two ways to restore the output commutation relation, and they correspond to performing different types of amplification [18]. The first is to treat the quadratures unequally. If one quadrature, say I is amplified by a factor \sqrt{G} and the other is reduced by a factor of $1/(\sqrt{G})$ then we can rewrite the output operators as $\mathbf{a}_{out} = (\sqrt{G} \mathbf{I}_{in} + i/(\sqrt{G}) \mathbf{Q}_{in})$ and $\mathbf{a}_{out}^\dagger = (\sqrt{G} \mathbf{I}_{in} - i/(\sqrt{G}) \mathbf{Q}_{in})$, then $[\mathbf{a}_{out}[\omega_1], \mathbf{a}_{out}[\omega_2]^\dagger] = \text{sgn}(\omega_1 - \omega_2) \delta(\omega_1 + \omega_2)$ as desired. This unequal treatment of quadratures, known as phase-sensitive amplification, is

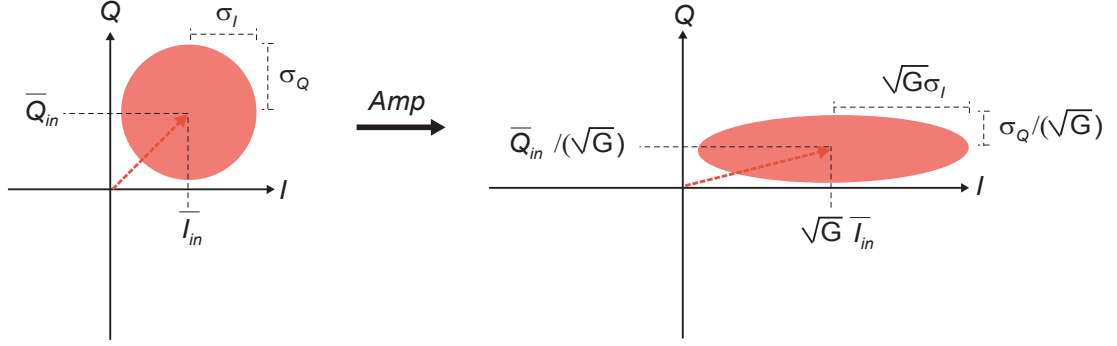


Figure 2.2: Fresnel plane before and after ideal phase-sensitive amplification. The input Fresnel lollipop has a center $(\bar{I}_{in}, \bar{Q}_{in})$ and a noise disk with standard deviation $\sigma_I = \sigma_Q$. The effect of the amplifier is to amplify Fresnel lollipop along one quadrature, here I , and de-amplifying it along the other. This results in an output lollipop with center $(\sqrt{G}\bar{I}_{in}, \bar{Q}_{in}/(\sqrt{G}))$ and a noise disk with standard deviations $\sqrt{G}\sigma_I$ and $\sigma_Q/(\sqrt{G})$.

shown graphically in fig. 2.2. Both the magnitude and the noise of the Fresnel lollipop are amplified along one quadrature, here I , and de-amplified along the other. This causes the disk to transform into an ellipse, but the signal to noise ratio of each quadrature individually remains constant. This type of amplification can be preferable if, for example, the signal is contained entirely in one quadrature.

Another way to maintain the commutation relations after the amplifier is to maintain the equal treatment of the quadratures so $\langle \mathbf{I}_{out} \rangle = \sqrt{G} \langle \mathbf{I}_{in} \rangle$ and $\langle \mathbf{Q}_{out} \rangle = \sqrt{G} \langle \mathbf{Q}_{in} \rangle$, and to include a second mode \mathbf{b} . If we take $\mathbf{a}_{out} = \sqrt{G}\mathbf{a}_{in} + \sqrt{G-1}\mathbf{b}_{in}^\dagger$ and $\mathbf{a}_{out}^\dagger = \sqrt{G}\mathbf{a}_{in}^\dagger + \sqrt{G-1}\mathbf{b}_{in}$, where $\sqrt{G-1}\mathbf{b}_{in}$ corresponds to amplified vacuum fluctuations coming from mode \mathbf{b} such that $[\mathbf{b}[\omega_1]_{in,out}, \mathbf{b}[\omega_2]_{in,out}^\dagger] = \text{sgn}(\omega_1 - \omega_2)\delta(\omega_1 + \omega_2)$, then $[\mathbf{a}[\omega_1]_{out}, \mathbf{a}[\omega_2]_{out}^\dagger] = \text{sgn}(\omega_1 - \omega_2)\delta(\omega_1 + \omega_2)\delta_{in,out}$ as desired. In a parametric amplifier this other mode \mathbf{b} typically corresponds to the mode of the device excited by the idler. This type of amplification, called phase-preserving amplification, is shown graphically in fig. 2.3. It is called phase-preserving amplification because the phase of the Fresnel lollipop relative to the I, Q axis is maintained. Although this type of amplification does add an additional half photon of noise from the vacuum fluctuations in mode \mathbf{b} , this noise still comes from the Heisenberg uncertainty principle, and does not lead to unwanted classical back-action [11]. Phase-preserving amplification is preferable if the signal is contained in both quadratures of the microwave field, or in an unknown quadrature of the microwave field. Even for a single-

quadrature signal, phase-preserving amplification may be preferable. In practice the signal quadrature and the amplified quadrature may drift relative to one another, and great care needs to be taken to minimize this effect.

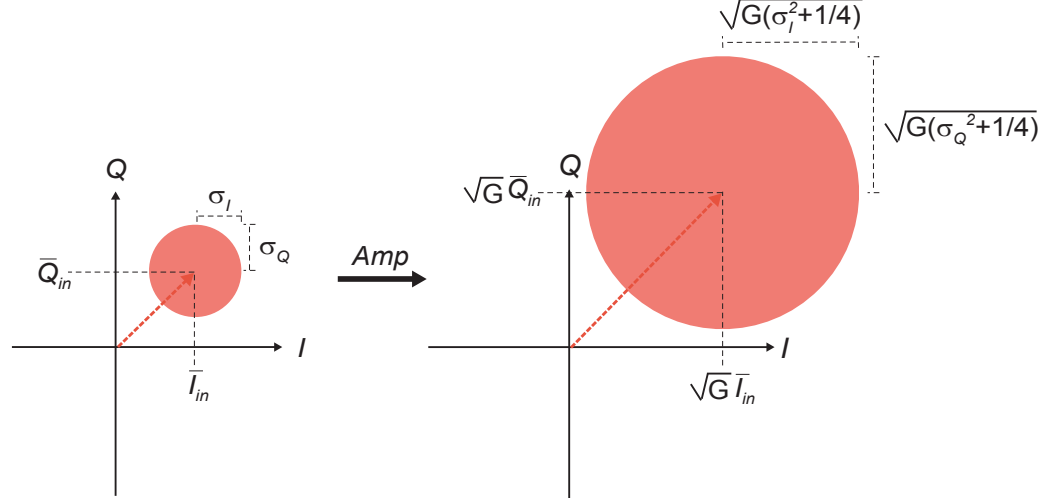


Figure 2.3: Fresnel plane before and after ideal phase-preserving amplification. The input Fresnel lollipop has center $(\bar{I}_{in}, \bar{Q}_{in})$ and a Gaussian noise disk with standard deviation $\sigma_I = \sigma_Q$. The amplifier treats the quadratures equally. This results in an output Fresnel lollipop with center $(\bar{I}_{in}\sqrt{G}, \bar{Q}_{in}\sqrt{G})$, and standard deviation $\sqrt{G(\sigma_{I,Q}^2 + 1/4)}$. The extra factor of $1/4$ in the standard deviation of each output quadrature corresponds to the additional Heisenberg noise added by the amplifier in order to restore the input and output commutation relations.

2.1.3 Reflection vs Through Amplifier

The next manner of classifying parametric amplifiers is based upon the path of signals through the device. An amplifier is classified as a reflection amplifier if any of the amplified signal exits the device from the same physical port it entered on. Amplifiers with a single physical port are necessarily reflection amplifiers, but multi port amplifiers may be reflection amplifiers as well. In contrast, an amplifier is classified as a through amplifier if the amplified signal exits the device through an entirely different physical port from the one it entered on. This does not necessarily mean that there is no amplified output exiting on any particular port, it just restricts the origin of those signals. For example, a two-port amplifier may have signals incident on port 1 exit through port 2 and vice versa. Port 1 still has an amplified output, but since the origin of that output is port 2 it is still a through amplifier. An

amplifier can be classified as a directional amplifier if the device amplifies signals from port 1 to port 2, and attenuates signals traveling in the reverse direction.

2.2 Four-Wave vs Three-Wave Mixing

The last major classification of parametric devices is based upon what type of non-linear mixing process gives rise to parametric amplification or conversion. Fourth order non-linearities in a system Hamiltonian give rise to a phenomena known as four-wave mixing. In this case parametric interactions manifest themselves in the mixing of two pump photons with one signal and one idler photon. Third order non-linearities will give rise to a similar phenomena known as three-wave mixing. Here parametric interactions correspond to mixing one pump, one signal, and one idler photon.

We can investigate the response of a circuit with a given Hamiltonian, \mathbf{H} , using the framework of input/output theory (see for example [82], or the appendix to [33]) and the quantum Langevin equation. In this framework the circuit is treated as a black box coupled to a transmission line which allows for incoming and outgoing waves. For each mode, the operators of the internal circuit mode are related to the incoming and outgoing field operators via

$$\sqrt{\kappa_a} \mathbf{a}(t) = \mathbf{a}_{in}(t) + \mathbf{a}_{out}(t) \quad (2.14)$$

where κ_a is the bandwidth the mode inherits from its coupling to the transmission line. The equation of motion for the internal mode of such a system can be calculated via the quantum Langevin equation

$$\frac{d\mathbf{a}(t)}{dt} = \frac{i}{\hbar} [\mathbf{H}, \mathbf{a}(t)] - \frac{\kappa_a}{2} \mathbf{a}(t) + \sqrt{\kappa_a} \mathbf{a}_{in}(t) \quad (2.15)$$

2.2.1 Four-Wave Mixing

Parametric devices based on four-wave mixing have fourth order non-linearities in their Hamiltonian. In a doubly-degenerate system this will correspond to the term $(\mathbf{a} + \mathbf{a}^\dagger)^4$, while in a non-degenerate system this will correspond to terms such as $(\mathbf{a} + \mathbf{a}^\dagger)(\mathbf{b} + \mathbf{b}^\dagger)(\mathbf{c} + \mathbf{c}^\dagger)^2$. In this section, following [43, 83], we will see how this type of term leads to amplification.

As an example, if we imagine the simplest single-mode resonant system with a fourth order nonlinearity, the Hamiltonian will take the form

$$\mathbf{H}_{4\text{wave}} = \hbar\omega'_a \mathbf{a}^\dagger \mathbf{a} + \hbar \frac{g_4}{6} (\mathbf{a} + \mathbf{a}^\dagger)^4 \quad (2.16)$$

where g_4 represents the strength of the fourth-order nonlinearity. Expanding and incorporating the effect of zero point motion into ω_a we get

$$\mathbf{H}_{4\text{wave}} = \hbar\omega_a \mathbf{a}^\dagger \mathbf{a} + \hbar \frac{g_4}{6} (\mathbf{a} \mathbf{a} \mathbf{a} \mathbf{a} + 4\mathbf{a}^\dagger \mathbf{a} \mathbf{a} \mathbf{a} + 6\mathbf{a}^\dagger \mathbf{a}^\dagger \mathbf{a} \mathbf{a} + 4\mathbf{a}^\dagger \mathbf{a}^\dagger \mathbf{a}^\dagger \mathbf{a} + \mathbf{a}^\dagger \mathbf{a}^\dagger \mathbf{a}^\dagger \mathbf{a}^\dagger) \quad (2.17)$$

The Langevin equation of motion for such a system is then given by

$$\begin{aligned} \frac{d\mathbf{a}(t)}{dt} = & -i\omega_a \mathbf{a}(t) - \frac{2ig_4}{3} \mathbf{a}(t) \mathbf{a}(t) \mathbf{a}(t) - 2ig_4 \mathbf{a}^\dagger(t) \mathbf{a}(t) \mathbf{a}(t) - 2ig_4 \mathbf{a}(t) \mathbf{a}^\dagger(t) \mathbf{a}^\dagger(t) \mathbf{a}(t) \\ & - \frac{2ig_4}{3} \mathbf{a}(t) \mathbf{a}^\dagger(t) \mathbf{a}^\dagger(t) \mathbf{a}^\dagger(t) - \frac{\kappa_a}{2} \mathbf{a}(t) + \sqrt{\kappa_a} \mathbf{a}_{in}(t) \end{aligned} \quad (2.18)$$

In a four-wave mixing system, parametric amplification occurs when the system is pumped with a strong tone at the frequency $2\omega_p = \omega_s + \omega_i$. In a doubly-degenerate system such as this, the pump, signal and idler are all associated with the same mode, leading to $\omega_s \sim \omega_i \sim \omega_p$. The incoming tone to mode \mathbf{a} will contain a contribution both from the pump and from the signal that will be amplified, which we can explicitly separate by letting α^p represent the pump and \mathbf{d} representing the small incoming signal. This results in

$$\begin{aligned} \mathbf{a}_{in}(t) &= \alpha_{in}^p(t) e^{-i(\omega_p t + \phi_p)} + \mathbf{d}_{in}(t) \\ \mathbf{a}_{out}(t) &= \alpha_{out}^p(t) e^{-i(\omega_p t + \phi_p)} + \mathbf{d}_{out}(t) \\ \mathbf{a}(t) &= \alpha^p(t) e^{-i(\omega_p t + \phi_p)} + \mathbf{d}(t) \end{aligned} \quad (2.19)$$

Further, we are going to assume the pump is stiff, that is the quantum amplitude of the pump can be treated as a classical drive and no changes in the pump amplitude due to quantum fluctuations in the mode or due to the dynamics of the circuit can be detected. Substituting these in to 2.18, taking the rotating wave approximation (RWA) to only keep

terms rotating at ω_p , and only terms linear in the signal we find

$$\begin{aligned}
& -i\omega_p\alpha^p(t)e^{-i(\omega_p t+\phi_p)} + \frac{d\mathbf{d}(t)}{dt} = \\
& -i\omega_a\alpha^p(t)e^{-i(\omega_p t+\phi_p)} - i\omega_a\mathbf{d}(t) - 2ig_4\alpha^p(t)^3e^{-i(\omega_p t+\phi_p)} \\
& -2ig_4\mathbf{d}(t)^\dagger\alpha^p(t)^2e^{-i(\omega_p t+2\phi_p)} - 4ig_4\alpha^p(t)^2\mathbf{d}(t) - \frac{\kappa_a}{2}\alpha^p(t)e^{-i(\omega_p t+\phi_p)} \\
& -\frac{\kappa_a}{2}\mathbf{d}(t) + \sqrt{\kappa_a}\alpha^p(t)e^{-i(\omega_p t+\phi_p)} + \sqrt{\kappa_a}\mathbf{d}_{in}(t)
\end{aligned} \tag{2.20}$$

The terms that only depend on $\alpha^p(t)$ correspond to the classical solution for the pump alone. Omitting the pump solution, the solution for the signal in the presence of the pump becomes

$$\frac{d\mathbf{d}(t)}{dt} = [-i\omega_a - \frac{\kappa_a}{2}]\mathbf{d}(t) - 4ig_4|\alpha^p(t)|^2\mathbf{d}(t) - 2ig_4\alpha^p(t)^2e^{-2i\phi_p}\mathbf{d}(t)^\dagger + \sqrt{\kappa_a}\mathbf{d}_{in}(t) \tag{2.21}$$

This is most easily solved by transforming to the frequency domain, yielding

$$\sqrt{\kappa_a}\mathbf{d}_{in}[\omega] = [i(\omega_a - \omega) + \frac{\kappa_a}{2}]\mathbf{d}[\omega] + 4ig_4(\alpha^p)^2\mathbf{d}[\omega] + 2ig_4(\alpha^p)^2e^{-2i\phi_p}\mathbf{d}[-\omega_i]^\dagger \tag{2.22}$$

where $\omega_i = 2\omega_p - \omega$. Here we first see the importance of the four-wave mixing term in the Hamiltonian. It is that term which gives rise to the $2ig_4\alpha^p(t)^2e^{-2i\phi_p}\mathbf{d}[-\omega_i]^\dagger$ term in the equation of motion, which corresponds to the creation of an idler at $-\omega_i$. This is a hallmark of parametric amplification resulting from the pairwise creation of signal and idler photons.

Using the input/output relation given in Eqn. 2.14 allows us to eliminate the internal mode and write the relationship between the incoming and outgoing fields for both the signal and the idler

$$\begin{aligned}
& [i(\omega_a - \omega) + \frac{\kappa_a}{2} + 4ig_4(\alpha^p)^2]\mathbf{d}_{out}[\omega] + 2ig_4(\alpha^p)^2e^{-2i\phi_p}\mathbf{d}_{out}[-\omega_i]^\dagger = \\
& [-i(\omega_a - \omega) + \frac{\kappa_a}{2} - 4ig_4(\alpha^p)^2]\mathbf{d}_{in}[\omega] - 2ig_4(\alpha^p)^2e^{-2i\phi_p}\mathbf{d}_{in}[-\omega_i]^\dagger \\
& [-i(\omega_a - \omega) + \frac{\kappa_a}{2} - 4ig_4(\alpha^p)^2]\mathbf{d}_{out}[-\omega_i]^\dagger - 2ig_4(\alpha^p)^2e^{2i\phi_p}\mathbf{d}_{out}[\omega] = \\
& [i(\omega_a - \omega) + \frac{\kappa_a}{2} + 4ig_4(\alpha^p)^2]\mathbf{d}_{in}[-\omega_i]^\dagger + 2ig_4(\alpha^p)^2e^{2i\phi_p}\mathbf{d}_{in}[\omega]
\end{aligned} \tag{2.23}$$

This coupled set of equations can easily be transformed into the scattering matrix

$$\begin{bmatrix} \mathbf{d}_{out}[\omega] \\ \mathbf{d}_{out}[-\omega_i]^\dagger \end{bmatrix} = \begin{bmatrix} s_{11} & s_{21}e^{-2i\phi_p} \\ s_{21}^\dagger e^{2i\phi_p} & s_{22} \end{bmatrix} \begin{bmatrix} \mathbf{d}_{in}[\omega] \\ \mathbf{d}_{in}[-\omega_i]^\dagger \end{bmatrix} \quad (2.24)$$

where we find reflected signal power gain $G = |s_{11}|^2 = |s_{22}|^2$ given by

$$G = 1 + \frac{64\kappa_a^2 g_4^2 (\alpha^p)^4}{(\kappa_a^2 - 16g_4^2 (\alpha^p)^4 + 4(\omega_a + 4g_4 (\alpha^p)^2 - \omega)^2)} \quad (2.25)$$

and trans-gain $G_T = |s_{21}|^2 = G - 1$ is given by

$$G_T = \frac{64\kappa_a^2 g_4^2 (\alpha^p)^4}{(\kappa_a^2 - 16g_4^2 (\alpha^p)^4 + 4(\omega_a + 4g_4 (\alpha^p)^2 - \omega)^2)} \quad (2.26)$$

2.2.2 Three-Wave Mixing

The other type of non-linear interaction that can give rise to parametric processes is three-wave mixing. This kind of interaction comes from third order non-linearities in the Hamiltonian. Although one could consider a third order non-linearity in a degenerate system, which would realize only amplification, here we will describe how to achieve both parametric gain and coherent frequency conversion within a non-degenerate system. Following [33], we posit the Hamiltonian of such a system to be

$$\begin{aligned} \mathbf{H}_{3\text{wave}} &= \hbar\omega_a \mathbf{a}^\dagger \mathbf{a} + \hbar\omega_b \mathbf{b}^\dagger \mathbf{b} + \hbar\omega_c \mathbf{c}^\dagger \mathbf{c} + \hbar g_3 (\mathbf{a} + \mathbf{a}^\dagger)(\mathbf{b} + \mathbf{b}^\dagger)(\mathbf{c} + \mathbf{c}^\dagger) \\ &= \hbar\omega_a \mathbf{a}^\dagger \mathbf{a} + \hbar\omega_b \mathbf{b}^\dagger \mathbf{b} + \hbar\omega_c \mathbf{c}^\dagger \mathbf{c} + \\ &\quad \hbar g_3 (\mathbf{a} \mathbf{b} \mathbf{c} + \mathbf{a}^\dagger \mathbf{b} \mathbf{c} + \mathbf{a} \mathbf{b}^\dagger \mathbf{c} + \mathbf{a}^\dagger \mathbf{b}^\dagger \mathbf{c} + \mathbf{a} \mathbf{b} \mathbf{c}^\dagger + \mathbf{a}^\dagger \mathbf{b} \mathbf{c}^\dagger + \mathbf{a} \mathbf{b}^\dagger \mathbf{c}^\dagger + \mathbf{a}^\dagger \mathbf{b}^\dagger \mathbf{c}^\dagger) \end{aligned} \quad (2.27)$$

This system is non-degenerate so we will let the signal excite mode \mathbf{a} , the idler excite mode \mathbf{b} , and the pump excite mode \mathbf{c} . Writing out the Langevin equations for the signal and the idler modes we find

$$\begin{aligned} \frac{d\mathbf{a}(t)}{dt} &= -i\omega_a \mathbf{a}(t) - ig_3 (\mathbf{b}(t) \mathbf{c}(t) + \mathbf{b}^\dagger(t) \mathbf{c}(t) + \mathbf{b}(t) \mathbf{c}(t)^\dagger + \mathbf{b}^\dagger(t) \mathbf{c}(t)^\dagger) - \frac{\kappa_a}{2} \mathbf{a}(t) + \sqrt{\kappa_a} \mathbf{a}_{in}(t) \\ \frac{d\mathbf{b}(t)}{dt} &= -i\omega_b \mathbf{b}(t) - ig_3 (\mathbf{a}(t)^\dagger \mathbf{c}(t) + \mathbf{a}(t) \mathbf{c}(t) + \mathbf{a}(t) \mathbf{c}^\dagger(t) + \mathbf{a}(t)^\dagger \mathbf{c}^\dagger(t)) - \frac{\kappa_b}{2} \mathbf{b}(t) + \sqrt{\kappa_b} \mathbf{b}_{in}(t) \end{aligned} \quad (2.28)$$

Parametric Gain

Parametric amplification in this system occurs when a pump applied to mode c is at the frequency $\omega_p = \omega_s + \omega_i = \omega_a + \omega_b$. If we again assume the pump is stiff, then we can replace $\mathbf{c}(t)$ by

$$\mathbf{c}(t) \rightarrow \alpha^p e^{-i\omega_p t + \phi_p} \quad (2.29)$$

Substituting these in and taking the rotating wave approximation (RWA) at ω_a and ω_b respectively the equations of motion reduce to

$$\begin{aligned} \frac{d\mathbf{a}(t)}{dt} &= -i\omega_a \mathbf{a}(t) - ig_3 \mathbf{b}(t)^\dagger \alpha^p e^{-i\phi_p} - \frac{\kappa_a}{2} \mathbf{a}(t) + \sqrt{\kappa_a} \mathbf{a}_{in}(t) \\ \frac{d\mathbf{b}(t)}{dt} &= -i\omega_b \mathbf{b}(t) - ig_3 \mathbf{a}(t)^\dagger \alpha^p e^{-i\phi_p} - \frac{\kappa_b}{2} \mathbf{b}(t) + \sqrt{\kappa_b} \mathbf{b}_{in}(t) \end{aligned} \quad (2.30)$$

Much like in the four-wave mixing case, here we explicitly see the creation of an idler in the equation of motion for the signal (and vice versa) coming from the third order mixing term. These coupled equations are again more easily solved in the frequency domain. Taking a Fourier transform of both sides, with ω_1 serving as the general frequency variable for the mode \mathbf{a} and ω_2 for \mathbf{b} , and substituting in the boundary conditions from the input/output relations gives

$$\begin{aligned} (i\omega_1 - i\omega_a - \frac{\kappa_a}{2}) \mathbf{a}_{out}[\omega_1] - ig_3 \alpha^p \sqrt{\frac{\kappa_a}{\kappa_b}} e^{-i\phi_p} \mathbf{b}_{out}[-\omega_2]^\dagger &= \\ (i\omega_a - i\omega_1 - \frac{\kappa_a}{2}) \mathbf{a}_{in}[\omega_1] + ig_3 \alpha^p \sqrt{\frac{\kappa_a}{\kappa_b}} e^{-i\phi_p} \mathbf{b}_{in}[-\omega_2]^\dagger & \\ (-i\omega_2 + i\omega_b - \frac{\kappa_b}{2}) \mathbf{b}_{out}[-\omega_2]^\dagger + ig_3 \alpha^p \sqrt{\frac{\kappa_b}{\kappa_a}} e^{i\phi_p} \mathbf{a}_{out}[\omega_1] &= \\ (-i\omega_b + i\omega_2 - \frac{\kappa_b}{2}) \mathbf{b}_{in}[-\omega_2]^\dagger - ig_3 \alpha^p \sqrt{\frac{\kappa_b}{\kappa_a}} e^{i\phi_p} \mathbf{a}_{in}[\omega_1] & \end{aligned} \quad (2.31)$$

where $\omega_2 = \omega_p - \omega_1$.

This coupled set of equations also gives rise to a parametric scattering matrix

$$\begin{bmatrix} \mathbf{a}_{out}[\omega_1] \\ \mathbf{b}_{out}[-\omega_2]^\dagger \end{bmatrix} = \begin{bmatrix} s_{11} & s_{21}e^{-i\phi_p} \\ s_{21}^\dagger e^{i\phi_p} & s_{22} \end{bmatrix} \begin{bmatrix} \mathbf{a}_{in}[\omega_1] \\ \mathbf{b}_{in}[-\omega_2]^\dagger \end{bmatrix} \quad (2.32)$$

where

$$s_{11} = \frac{(1 + 2i(\omega_a - \omega_1)/\kappa_a)(1 + 2i(\omega_2 - \omega_b)/\kappa_b) + \rho^2}{(1 - 2i(\omega_a - \omega_1)(1 + 2i(\omega_2 - \omega_b)/\kappa_b) - \rho^2)} \quad (2.33)$$

$$s_{21} = \frac{-2i\rho}{(1 - 2i(\omega_a - \omega_1)(1 + 2i(\omega_2 - \omega_b)/\kappa_b) - \rho^2)} \quad (2.34)$$

$$s_{22} = \frac{(1 - 2i(\omega_a - \omega_1)/\kappa_a)(1 - 2i(\omega_2 - \omega_b)/\kappa_b) + \rho^2}{(1 - 2i(\omega_a - \omega_1)(1 + 2i(\omega_2 - \omega_b)/\kappa_b) - \rho^2)} \quad (2.35)$$

and we have defined the normalized pump power ρ by

$$\rho = \frac{g_3 \alpha^p}{\sqrt{\kappa_a \kappa_b}} \quad (2.36)$$

On resonance, $\omega_1 = \omega_a$ and $\omega_2 = \omega_b$, the scattering matrix reduces to

$$\begin{bmatrix} \mathbf{a}_{out}[\omega_a] \\ \mathbf{b}_{out}[-\omega_b]^\dagger \end{bmatrix} = \begin{bmatrix} \sqrt{G} & -i\sqrt{G_T}e^{-i\phi_p} \\ i\sqrt{G_T}e^{i\phi_p} & \sqrt{G} \end{bmatrix} \begin{bmatrix} \mathbf{a}_{in}[\omega_a] \\ \mathbf{b}_{in}[-\omega_b]^\dagger \end{bmatrix} \quad (2.37)$$

where the reflected signal power gain is

$$G = \frac{1 + \rho^2}{1 - \rho^2} \quad (2.38)$$

and the trans-gain

$$G_T = \frac{2}{1 - \rho^2} \quad (2.39)$$

where again $G_T = G - 1$.

Parametric Conversion

The three-wave mixing non-linearity also supports another parametric process, coherent frequency conversion [29, 35]. To realize this process we pump one of the modes, say mode \mathbf{c} , at the frequency difference of the other two: $\omega_{\mathbf{a}} - \omega_{\mathbf{b}}$. Returning to Eqn. 2.28, and again following [33] the equations of motion for the signal and idler under the RWA now become

$$\begin{aligned}\frac{d\mathbf{a}(t)}{dt} &= -i\omega_{\mathbf{a}}\mathbf{a}(t) - ig_3\mathbf{b}(t)\alpha^p e^{i\phi_p} - \frac{\kappa_{\mathbf{a}}}{2}\mathbf{a}(t) + \sqrt{\kappa_{\mathbf{a}}}\mathbf{a}_{in}(t) \\ \frac{d\mathbf{b}(t)}{dt} &= -i\omega_{\mathbf{b}}\mathbf{b}(t) - ig_3\mathbf{a}(t)\alpha^p e^{i\phi_p} - \frac{\kappa_{\mathbf{b}}}{2}\mathbf{b}(t) + \sqrt{\kappa_{\mathbf{b}}}\mathbf{b}_{in}(t)\end{aligned}\quad (2.40)$$

Substituting in the input/output relation and writing the coupled equations in matrix form yields

$$\begin{bmatrix} \mathbf{a}_{out}[\omega_1] \\ \mathbf{b}_{out}[\omega_2] \end{bmatrix} = \begin{bmatrix} s_{11} & s_{21}e^{-i\phi_p} \\ s_{21}^\dagger e^{i\phi_p} & s_{22} \end{bmatrix} \begin{bmatrix} \mathbf{a}_{in}[\omega_1] \\ \mathbf{b}_{in}[\omega_2] \end{bmatrix}\quad (2.41)$$

where

$$s_{11} = \frac{(1 + 2i(\omega_{\mathbf{a}} - \omega_1)/\kappa_{\mathbf{a}})(1 - 2i(\omega_2 - \omega_{\mathbf{b}})/\kappa_{\mathbf{b}}) - \rho^2}{(1 - 2i(\omega_{\mathbf{a}} - \omega_1)(1 + 2i(\omega_2 - \omega_{\mathbf{b}})/\kappa_{\mathbf{b}}) + \rho^2)}\quad (2.42)$$

$$s_{21} = \frac{2i\rho}{(1 - 2i(\omega_{\mathbf{a}} - \omega_1)(1 + 2i(\omega_2 - \omega_{\mathbf{b}})/\kappa_{\mathbf{b}}) + \rho^2)}\quad (2.43)$$

$$s_{22} = \frac{(1 - 2i(\omega_{\mathbf{a}} - \omega_1)/\kappa_{\mathbf{a}})(1 + 2i(\omega_2 - \omega_{\mathbf{b}})/\kappa_{\mathbf{b}}) - \rho^2}{(1 - 2i(\omega_{\mathbf{a}} - \omega_1)(1 + 2i(\omega_2 - \omega_{\mathbf{b}})/\kappa_{\mathbf{b}}) + \rho^2)}\quad (2.44)$$

and again

$$\rho = \frac{g_3\alpha^p}{\sqrt{\kappa_{\mathbf{a}}\kappa_{\mathbf{b}}}}\quad (2.45)$$

On resonance this reduces to

$$\begin{bmatrix} \mathbf{a}_{out}[\omega_1] \\ \mathbf{b}_{out}[\omega_2] \end{bmatrix} = \begin{bmatrix} \sqrt{1-C} & i\sqrt{C}e^{-i\phi_p} \\ -i\sqrt{C}e^{i\phi_p} & \sqrt{1-C} \end{bmatrix} \begin{bmatrix} \mathbf{a}_{in}[\omega_1] \\ \mathbf{b}_{in}[\omega_2] \end{bmatrix}\quad (2.46)$$

Where the conversion coefficient $C = \frac{4g_3^2(\alpha^p)^2/(\kappa_a\kappa_b)}{(1+|g_3|^2(\alpha^p)^2/(\kappa_a\kappa_b))^2}$. This process corresponds to coherent conversion of signals incident on one mode into signals exiting from the other. This process is realized in full for the extremal value $C = 1$, where all signal and idler photons are converted into each other on a one for one basis (with a phase shift given by the phase of the pump). For $0 < C < 1$, only part of the incoming signal is coherently converted to the other mode with the rest reflected this just corresponds to partial conversion and partial reflection of an incoming signal, where the amount reflected and the amount converted is controlled by the value of C .

2.3 Parametric Amplification with the JBA

The first specific parametric device we will look at is the JBA [43, 83], which is a doubly-degenerate, four-wave mixing, reflection amplifier which is typically used to implement phase-sensitive amplification. As can be seen in Fig. 2.4, it is composed of two Josephson junctions connected in a loop to form a SQUID, which is then shunted by a split parallel plate capacitor. We can simplify the circuit by treating it as a single junction shunted by a single capacitor as follows. By Kirchhoff's current law, and assuming the linear inductance of the loop is small, the current going into the SQUID, I_s , is given by $I_s = I_0 \sin(\frac{\Phi_1}{\varphi_0}) + I_0 \sin(\frac{\Phi_2}{\varphi_0}) = I_0 \sin(\varphi_1) + I_0 \sin(\varphi_2)$. The total magnetic flux through a loop is quantized, so if an external magnetic flux, Φ_{ext} , is applied to the loop of the SQUID, the relation $\varphi_2 - \varphi_1 = \Phi_{\text{ext}}/\varphi_0 + 2\pi n$, where n is an integer, must hold. Using this, we can rewrite the current through the SQUID as $I_s = 2I_0 \cos(\frac{\Phi_{\text{ext}}}{2\varphi_0} + n\pi) \sin(\varphi)$ where $\varphi = (\varphi_1 + \varphi_2)/2$ is the phase across the SQUID. This looks like one effective junction whose critical current changes with the external applied magnetic flux. Moving to the capacitor, the physical structure is two identical capacitors which share a common voltage on one plate. This is equivalent to a single parallel plate capacitor with double the distance between the plate, yielding a total capacitance C whose value is half the capacitance of either physical capacitor alone. This circuit has only one normal mode, so the JBA must be a degenerate parametric amplifier. It also only has one physical port coupled to that one normal mode, meaning it must be a reflection amplifier.

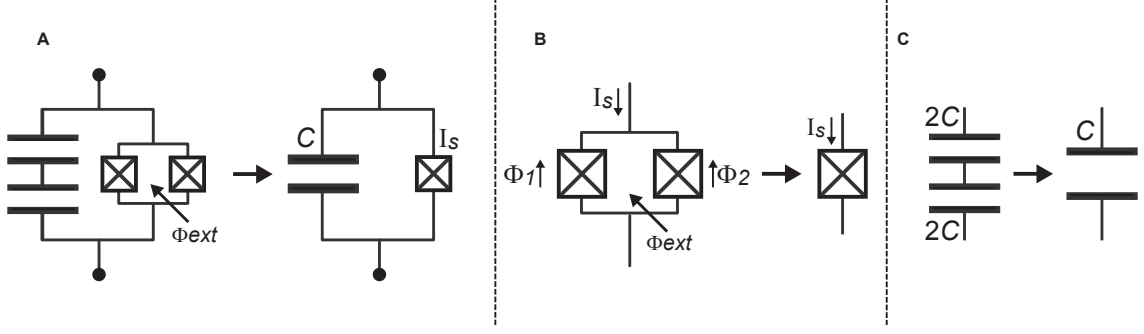


Figure 2.4: Schematic of the JBA. A) The JBA consists of a SQUID loop shunted by a large split capacitor. For some fixed value of an externally applied magnetic field given by Φ_{ext} , the SQUID can be treated of as a single effective junction with critical current I_s and the split capacitor can be treated as a single effective capacitor with capacitance C . The device here is drawn with two ports (black circles) since it will be differentially driven with an in-box hybrid. B) If the SQUID had identical junctions, meaning $\varphi_1 = \varphi_2$, then it can be treated as a single effective junction with critical current I_s . C) The two physical capacitors having capacitance $2C$ can be represented as a single capacitor having capacitance C .

To show that it is a four-wave mixing amplifier, we need to write out the Hamiltonian and check the order of the non-linearity. For the reduced circuit composed of a single effective capacitor and a single effective junction the Hamiltonian is

$$\mathbf{H}_{\text{JBA}} = \frac{Q^2}{2C} - E_J \cos(\varphi) \quad (2.47)$$

where $\frac{Q^2}{2C}$ is the energy corresponding to the effective capacitance, and $-E_J \cos(\varphi)$ is the energy of the effective junction, with $E_J = \varphi_0 I_s$. Expanding the cosine

$$\mathbf{H}_{\text{JBA}} = \frac{Q^2}{2C} - E_J + \frac{E_J \varphi^2}{2!} - \frac{E_J \varphi^4}{4!} + \dots \quad (2.48)$$

Writing the Hamiltonian in terms of the creation and annihilation operators for the normal mode of the circuit given by $Q = \sqrt{\frac{\hbar}{2Z_a}} \frac{a - a^\dagger}{i}$ and $\varphi = \sqrt{\frac{\hbar Z_a}{2\varphi_0^2}} (a + a^\dagger)$ where $Z_a = \sqrt{\frac{\varphi_0^2}{E_J C}}$, and incorporating the zero point motion into ω_a we find

$$\mathbf{H}_{\text{JBA}} = \frac{\hbar \omega_a}{2} a^\dagger a - \frac{\hbar^2}{96 \varphi_0^2 C} (a + a^\dagger)^4 + \dots \quad (2.49)$$

This is equivalent to the four-wave mixing Hamiltonian given in Eqn. 2.17 with $g_4 = \frac{\hbar^2}{96 \varphi_0^2 C}$, making the JBA a four-wave mixing amplifier. When the JBA is excited with a strong

pump tone we can see the expected parametric gain (see Fig. 2.5).

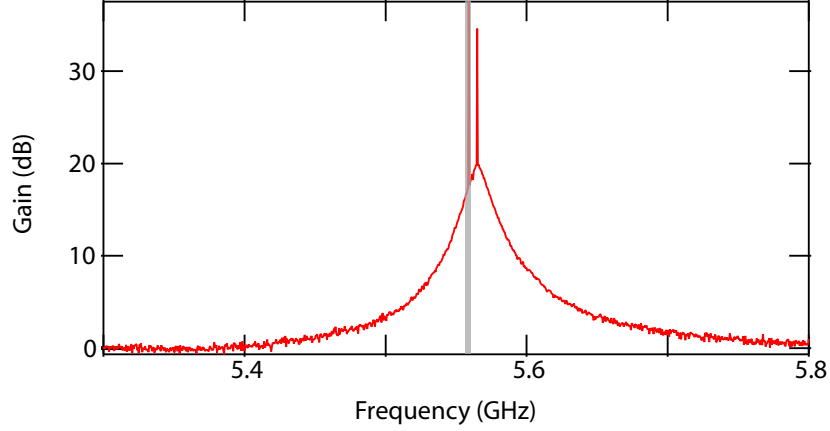


Figure 2.5: Measured 20 dB reflection gain from the JBA. The strong reflected pump tone, as well as a pump artifact (colored in gray), can be seen at shown at the center of the Lorentzian gain curve.

The JBA can be operated as either a phase-sensitive or phase-preserving amplifier depending on how the input signal is presented to the device. As can be seen from the four-wave mixing scattering matrix (Eqn. 2.24), the JBA will sum the incoming signal and idler tones. If a signal is presented slightly detuned from resonance such that $\omega_s = \omega_p + \delta\omega$, and if the incoming idler at $\omega_i = \omega_p - \delta\omega$ is left in vacuum, then the JBA will perform phase-preserving amplification, where the half-photon of added noise comes from quantum fluctuations in the vacuum presented to the idler.

If instead the incoming signal has a bandwidth straddling the pump, then the amplifier matrix mixes the incoming signal with itself and the output becomes

$$\begin{aligned} \mathbf{a}[\omega]_{out} &= \sqrt{G}\mathbf{a}[\omega]_{in} + \sqrt{G_T}e^{-2i\phi_p}\mathbf{a}[\omega_i]_{in}^\dagger \\ \mathbf{a}[-\omega_i]_{out}^\dagger &= \sqrt{G_T}e^{2i\phi_p}\mathbf{a}[\omega]_{in} + \sqrt{G}\mathbf{a}[-\omega_i]_{in}^\dagger \end{aligned} \quad (2.50)$$

Converting to quadrature variables, this is equivalent to

$$\begin{aligned} I_{out} &= (\sqrt{G} + \sqrt{G_T}e^{-2i\phi_p})I_{in} \\ Q_{out} &= (\sqrt{G} - \sqrt{G_T}e^{-2i\phi_p})Q_{in} \end{aligned} \quad (2.51)$$

For some pump phases such as $\phi_p = 0$, $I_{out} = (\sqrt{G} + \sqrt{G_T})I_{in} = (\sqrt{G} + \sqrt{G-1})I_{in}$ and

$Q_{out} = (\sqrt{G} - \sqrt{G_T})Q_{in} = (\sqrt{G} - \sqrt{G-1})Q_{in}$ which in the high gain limit simplifies to

$$\begin{aligned} I_{out} &= 2\sqrt{G}I_{in} \\ Q_{out} &= 1/(2\sqrt{G})Q_{in} \end{aligned} \quad (2.52)$$

This corresponds to phase-sensitive amplification where the I quadrature is amplified and the Q quadrature is de-amplified. For other pump phases such as $\phi_p = \pi/2$, the Q quadrature is amplified and the I quadrature is de-amplified.

2.4 Parametric Amplification and Coherent Conversion with the JPC

The next specific parametric device we will look at is the JPC [29, 30, 34]. As we will see, the JPC is a non-degenerate, reflection amplifier typically used to perform phase-preserving amplification. It is also a three-wave mixing amplifier, which allows it to function both as an amplifier and as a coherent converter. The three-wave mixing interaction in the JPC originates from the loop of Josephson junctions found at the heart of the device. This loop, known as the Josephson ring modulator (JRM), was originally composed of four junctions in a loop and was later extended to include four linear shunt inductors (see Fig. 2.6) or Josephson junctions playing the role of inductors [31, 34].

The energy of the JRM can be found by summing the energy of all the constitutive elements. Each Josephson junction will have energy $-E_J \cos(\varphi_i)$, where $\varphi_i = \Phi_i/\varphi_0$, and each linear shunting inductor will have energy $1/2LI^2$ where I is the current flowing through it. If we assume all the outer junctions are identical and all of the inner shunting inductors are identical we find

$$E_{\text{JRM}} = -E_J(\cos(\varphi_a) + \cos(\varphi_b) + \cos(\varphi_c) + \cos(\varphi_d)) + \frac{1}{2L}(\varphi_1^2 + \varphi_2^2 + \varphi_3^2 + \varphi_4^2) \quad (2.53)$$

The JRM has three normal modes which we can write down in terms of the node fluxes $\Phi_{I,II,III,IV}$. \mathbf{a} corresponds to a top/bottom excitation of the ring given by $\Phi_{\mathbf{a}} = \Phi_I - \Phi_{III}$, \mathbf{b} corresponds to a right/left excitation of the ring given by $\Phi_{\mathbf{b}} = \Phi_{IV} - \Phi_{II}$, and \mathbf{c} which

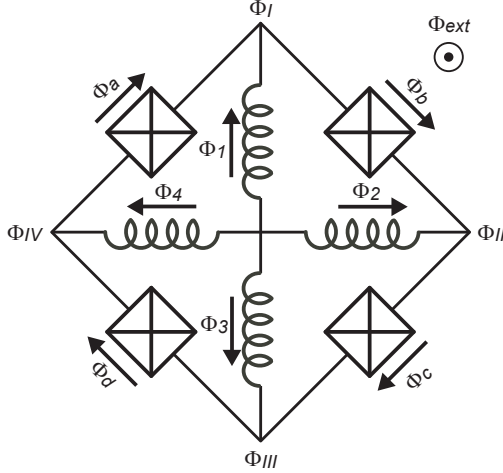


Figure 2.6: Schematic of the JRM. The shunted JRM is composed of four outer Josephson junctions and four inner shunt inductors which allow for frequency tunability when the entire ring is threaded with an uniform external flux given by Φ_{ext} . Also included are the fluxes Φ_i and flux directions for each circuit element in the ring as well as the node-fluxes $\Phi_{I,II,III,IV}$.

is a common mode excitation of the ring given by $\Phi_c = (\Phi_{II} + \Phi_{IV} - \Phi_I - \Phi_{III})/2$ (see Fig. 2.7).

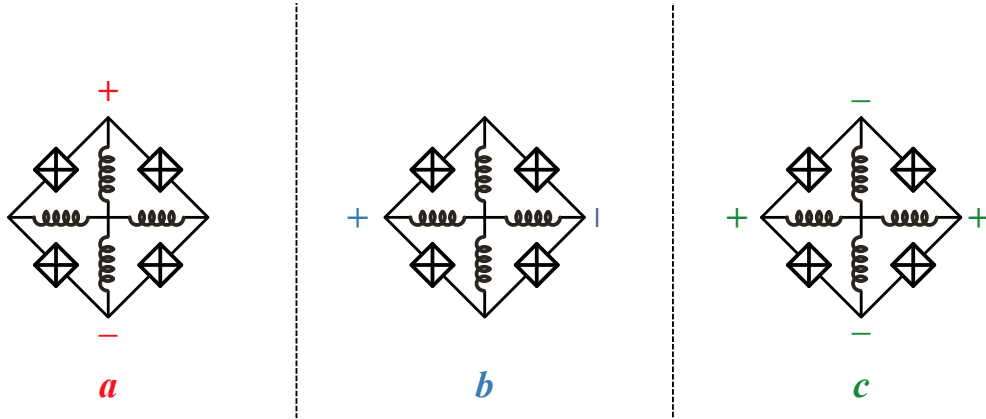


Figure 2.7: The three normal modes of the JRM. Mode **a** corresponds to a left-right excitation of the ring, mode **b** corresponds to a top-bottom excitation of the ring, and mode **c** corresponds to a common excitation of the ring.

We can make a change of variables from the fluxes through the outer junctions into the

three normal mode fluxes plus an extra mode Φ_M

$$\begin{bmatrix} \varphi_a \\ \varphi_b \\ \varphi_c \\ \varphi_M \end{bmatrix} = \begin{bmatrix} \frac{1}{2} & \frac{1}{2} & -\frac{1}{2} & -\frac{1}{2} \\ \frac{1}{2} & -\frac{1}{2} & -\frac{1}{2} & \frac{1}{2} \\ \frac{1}{4} & -\frac{1}{4} & \frac{1}{4} & -\frac{1}{4} \\ 1 & 1 & 1 & 1 \end{bmatrix} \begin{bmatrix} \varphi_a \\ \varphi_d \\ \varphi_c \\ \varphi_b \end{bmatrix}$$

Although Φ_M does not couple to the ring, it does represent the effect of an external flux threading the JRM. This can be seen from looking at the flux quantization condition $\varphi_a + \varphi_b + \varphi_c + \varphi_d = \frac{\Phi_{\text{ext}}}{\varphi} + 2\pi n = \varphi_M$. Taking the lowest ring energy where $n=0$, we can write the flux through the linear inductors as a function of the normal mode fluxes

$$\begin{aligned} 4\Phi_1 &= 3\Phi_I - \Phi_{II} - \Phi_{III} - \Phi_{IV} = 2\Phi_a - 2\Phi_c \\ 4\Phi_2 &= 3\Phi_{II} - \Phi_I - \Phi_{III} - \Phi_{IV} = -2\Phi_b + 2\Phi_c \\ 4\Phi_3 &= 3\Phi_{II} - \Phi_I - \Phi_{II} - \Phi_{IV} = -2\Phi_a - 2\Phi_c \\ 4\Phi_4 &= 3\Phi_{IV} - \Phi_I - \Phi_{II} - \Phi_{III} = 2\Phi_b - 2\Phi_c \end{aligned} \tag{2.54}$$

This allows us to express the energy of the ring as

$$\begin{aligned} E_{\text{JRM}} &= -4E_J \cos(\varphi_a/2) \cos(\varphi_b/2) \cos(\varphi_c) \cos(\varphi_{\text{ext}}/4) \\ &\quad - 4E_J \sin(\varphi_a/2) \sin(\varphi_b/2) \sin(\varphi_c) \sin(\varphi_{\text{ext}}/4) \\ &\quad + \frac{\varphi_0^2}{2L} \left(\frac{\varphi_a^2}{2} + \frac{\varphi_b^2}{2} + \varphi_c^2 \right) \end{aligned} \tag{2.55}$$

Expanding to the third order in φ_a , φ_b , and φ_c this becomes

$$\begin{aligned} E_{\text{JRM}} &= -4E_J \cos(\varphi_{\text{ext}}/4) + \left(\frac{\varphi_0^2}{4L} + \frac{E_J}{2} \cos(\varphi_{\text{ext}}/4) \right) (\varphi_a^2 + \varphi_b^2) \\ &\quad + \left(\frac{\varphi_0^2}{2L} + 4E_J \cos(\varphi_{\text{ext}}/4) \right) \varphi_c^2 - E_J \sin(\varphi_{\text{ext}}/4) \varphi_a \varphi_b \varphi_c \end{aligned} \tag{2.56}$$

This expression includes a the three-wave mixing term in the form $\varphi_a \varphi_b \varphi_c$, but this is just the energy expression for the JRM, not the JPC as a whole. To complete the circuit we embed the JRM at the center of two crossed $\lambda/2$ resonators (see Fig. 2.8). The resonant

modes of this structure directly couple to the normal modes of the ring: the excitation of the signal resonator will couple to the top-bottom excitation of the ring corresponding to mode **a**, the excitation of the other resonator will couple to the left-right excitation of mode **b**, and the elbow excitation of the two resonators will couple to mode **c**. Signals are presented to mode **a** and mode **b** via the delta ports of a 180-degree hybrid, and the pump is presented via the one of the sigma ports which allows the spatial pattern of the incoming signals to match the spatial pattern of the modes. It should be noted that the linear resonance of mode **c** will be $(\omega_a + \omega_b)/2$, which is generally far detuned from the frequency of the applied pump. The one-to-one correspondence between normal modes of the circuit and the pump, signal, and idler tones means the JPC is a non-degenerate amplifier. Taking the ring and the resonators together we can write the Hamiltonian of the full JPC in terms of the creation and annihilation operators of the modes instead of the fluxes, we find

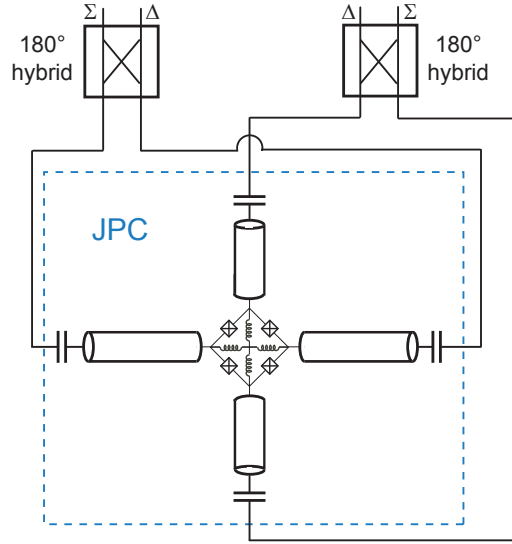


Figure 2.8: Schematic of the complete JPC. The JRM is embedded in two crossed $\lambda/2$ resonators, which are then driven with a set of 180-degree hybrids. The differential port of the hybrid attached to the vertical resonator provides a drive which excites mode **a**, while that of the hybrid attached to the horizontal resonator properly excites mode **b**. Either could be used as the amplifier input. The sigma port of one of the hybrids is used for the off resonant pump, while the other sigma port has to be terminated in a cold 50Ω .

$$\mathbf{H}_{\text{JPC}} = \hbar\omega_a \mathbf{a} \mathbf{a}^\dagger + \hbar\omega_b \mathbf{b} \mathbf{b}^\dagger + \hbar\omega_c \mathbf{c} \mathbf{c}^\dagger + g_3 (\mathbf{a} + \mathbf{a}^\dagger)(\mathbf{b} + \mathbf{b}^\dagger)(\mathbf{c} + \mathbf{c}^\dagger) + \dots \quad (2.57)$$

where the mode frequencies have been slightly renormalized but the square terms in E_{Ring} and $g_3 = -E_J \sin(\frac{\Phi_{\text{ext}}}{4}) \sqrt{\frac{\hbar}{2Z_a}} \sqrt{\frac{\hbar}{2Z_b}} \sqrt{\frac{\hbar}{2Z_c}}$ with the impedance for mode i is given by $Z_i = \sqrt{\frac{L_i}{C_i}}$. This is equivalent to the three-wave mixing Hamiltonian given in Eqn. 2.27, making the JPC a three-wave mixing amplifier.

As a three-wave mixing amplifier, the JPC is capable of both parametric gain and conversion. When one mode, say mode \mathbf{c} , is pumped with a strong tone at frequency $\omega_a + \omega_b$ the JPC exhibits parametric gain (see Fig. 2.9). As expected from the three-wave mixing scattering matrix, the JPC shows both reflection gain and trans-gain making it a reflection amplifier. Furthermore, since the signal and idler both excite different normal modes of the circuit it is a non-degenerate amplifier. If the mode \mathbf{c} is instead pumped with a strong tone at frequency $\omega_a - \omega_b$ the JPC exhibits conversion (see Fig. 2.10). The dip seen in the reflected scattering parameter corresponds to the fact that incident photons on \mathbf{a} are not reflected off the input mode, but are instead converted to mode \mathbf{b} leading to a peak in s_{ab} .

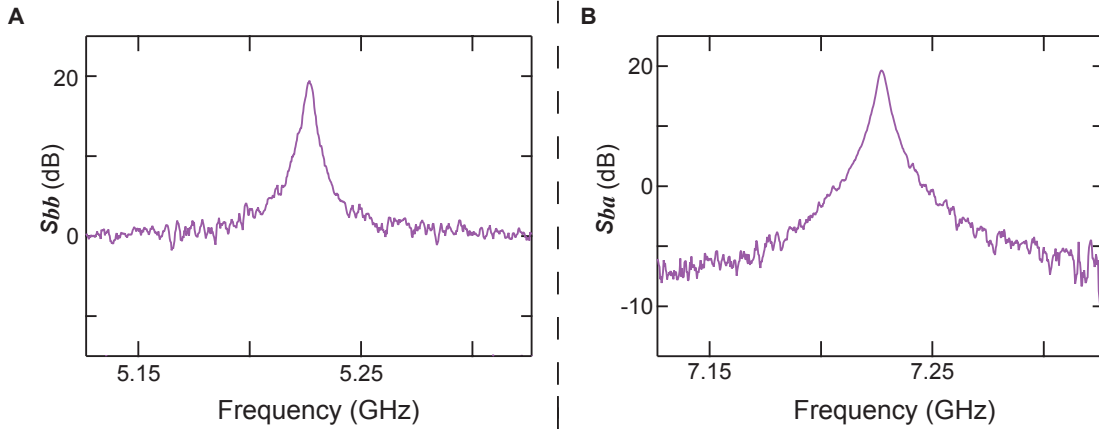


Figure 2.9: Measure JPC response curve. The maximum gain is 20 dB. The device exhibits both reflection gain (A) where signals both enter and exit with gain on a single port and trans-gain (B) where signals enter one port and are amplified and frequency converted and exit on the other. Since the input and output are at separate frequencies, a mixer was used $\omega_b + \omega_c$ to mix the output at frequency ω_b back down to the input frequency ω_c .

The JPC can also implement either phase-sensitive or phase preserving amplification depending on how the signal is presented to the device [34]. Analogously to the JBA, if the signal is applied to only one mode, and the other is left in vacuum, then the JPC will perform phase-preserving amplification. If the signal is instead split, and applied to both modes such that the signal can interfere with itself within the amplifier, then it will perform phase-sensitive amplification. This is much harder to implement in the JPC than it is in the JBA, since the JPC is a non-degenerate amplifier where the modes are both at very different frequencies and addressed via entirely different spatial ports. Thus the JPC is usually used to implement phase-preserving amplification.

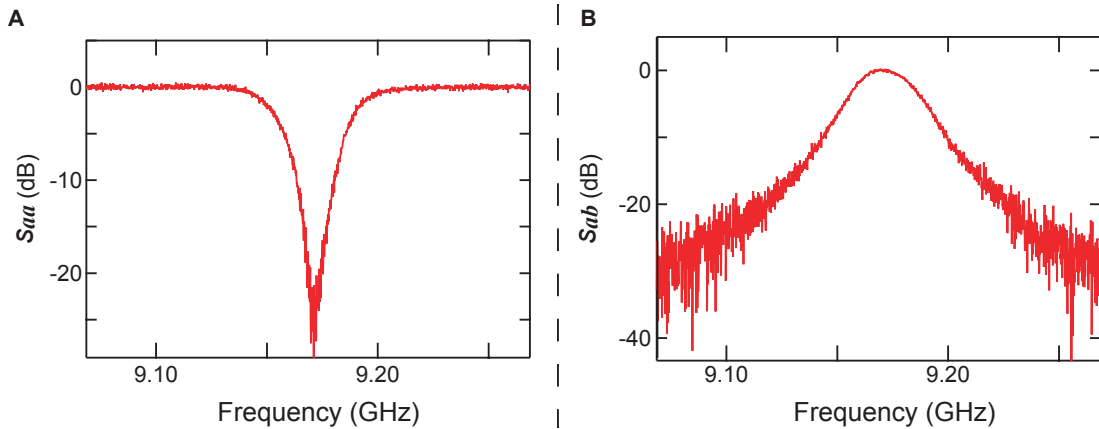


Figure 2.10: Measured conversion from the JPC for $C = 0.99$. The dip in the reflected scattering parameter (A) indicates photons incident on mode \mathbf{a} at 9.17 GHz are not being reflected. Instead they are being frequency translated over to mode \mathbf{b} at 5.25 GHz. These converted photons appear as a peak (B) whose magnitude approaches 1 as the conversion coefficient grows. Since the input and output for B are at separate frequencies, a mixer was used $\omega_a - \omega_b$ to mix the output at frequency ω_b back down to the input frequency ω_a .

Physical Implementation of the JPC

Unlike the JBA, which is implemented exactly as described earlier, there are a few different physical implementation of the JPC. The shunting inductors in the JRM have been implemented via linear inductors as described above [31], but the length of the wire needed to provide sufficient linear inductance leads to a very large ring. Other types of inductors have been used to shunt the outer junctions of the JRM including larger Josephson junctions (see Fig. 2.11), and the kinetic inductance of thin aluminum wires. Larger junctions [34]

are typically chosen because they minimize the size of the JRM while being relatively easy to reproducibly fabricate. The resonant modes are typically defined by $\lambda/2$ resonators as described, but those have also been implemented instead by large external capacitances shunting the JRM much in the style of the JBA. In this case the mode frequencies are defined by large capacitance shunting a particular mode, and inductance of that mode coming from the JRM. This implementation, developed both here at Yale and concurrently at ENS-Paris [32], minimizes the size of the JPC, and can lead to some performance improvements, but is much more sensitive to asymmetries in the JRM.

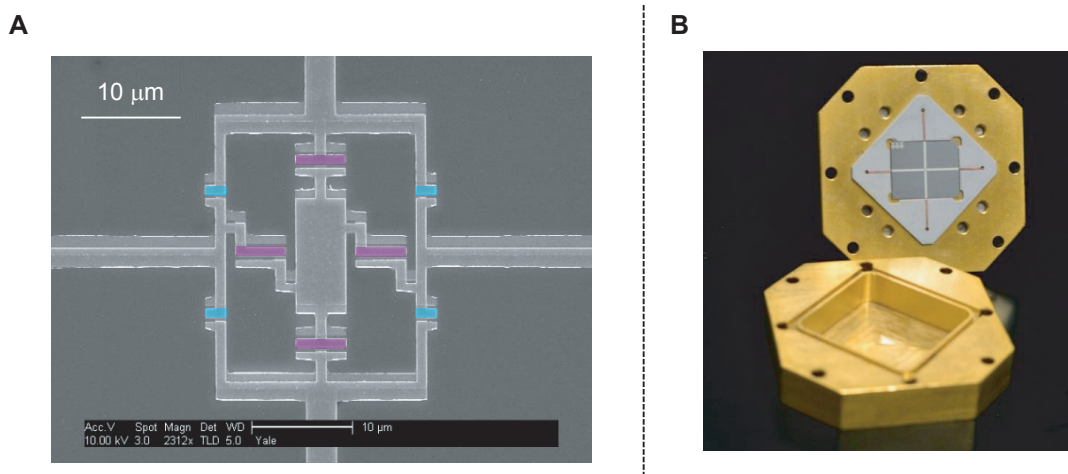


Figure 2.11: SEM image of the JRM and optical image of the full JPC. A) SEM image of the eight-junction JRM shunted by large Josephson junctions. The small outer junction that give the three-wave mixing nonlinearity are highlighted in blue while the four inner junctions shunting the ring are highlighted in purple. B) Photograph of the complete amplifier. It shows the JPC chip (dark gray) with the two resonators visible in light gray. Also visible is the PC board (square, white) whose role is to provide the interface between the chip and the SMA connectors (not visible) located on the back of the gold housing.

Chapter 3

Double Pumping the JBA

The JBA, which was presented in the last chapter, is widely used as a parametric amplifier in superconducting qubit experiments. As a four wave mixing device, it is typically biased with a single strong pump tone whose frequency, ω_p , corresponds to the frequency of maximum gain, ω_g . However, when integrated with a superconducting qubit, the strong pump tone coincides problematically with the center of the bandwidth of the cavity. Without sufficient isolation, the reflected pump floods the cavity with photons causing significant dephasing. As proposed in a theoretical paper by Kamal et al. [56], the single pump at the center of the amplification band can be replaced with two pumps at the frequencies $\omega_{pump1} = \omega_g + \Delta$ and $\omega_{pump2} = \omega_g - \Delta$. If Δ is large enough, both of these pump tones can be well outside the bandwidth of the cavity, and the amplifier can cause significantly less dephasing. This chapter presents both the theory and an experimental realization of the double-pumped mode of operation, and shows that this operating scheme leads to significantly less dephasing while also increasing the amount of input power the amplifier is capable of handling.

3.1 Derivation of Double-Pumped Gain

The theoretical deviation of gain in the double-pumped JBA was originally derived in [56], here it will be re-derived, but via a slightly different method. We will use the approach presented in the last chapter for the single-pumped four wave mixing amplifier, but we will modify the incoming and internal fields to include two pump fields given by $\alpha^+(t)e^{-i(\omega_{pump1}t+\phi_{p1})}$

and $\alpha^-(t)e^{-i(\omega_{pump2}t+\phi_{p2})}$

$$\begin{aligned}
\mathbf{a}_{in}(t) &= \alpha_{in}^+(t)e^{-i(\omega_{pump1}t+\phi_{p1})} + \alpha_{in}^-(t)e^{-i(\omega_{pump2}t+\phi_{p2})} + \mathbf{d}_{in}(t) \\
\mathbf{a}_{out}(t) &= \alpha_{out}^+(t)e^{-i(\omega_{pump1}t+\phi_{p1})} + \alpha_{out}^-(t)e^{-i(\omega_{pump2}t+\phi_{p2})} + \mathbf{d}_{out}(t) \\
\mathbf{a}(t) &= \alpha^+(t)e^{-i(\omega_{pump1}t+\phi_{p1})} + \alpha^-(t)e^{-i(\omega_{pump2}t+\phi_{p2})} + \mathbf{d}(t)
\end{aligned} \tag{3.1}$$

where $\omega_{pump1} = \omega_g + \Delta$, $\omega_{pump2} = \omega_g - \Delta$, and $\mathbf{c}(t)$ represents a small incoming signal around ω_g . We will take both pumps to be stiff, replacing $\alpha^{(+,-)}(t)$ with $\alpha^{(+,-)}$ and $\alpha_{in,out}^{(+,-)}(t)$ with $\alpha_{in,out}^{(+,-)}$. If we insert these back into the four-wave mixing Langevin equation (Eqn. 2.18), keep only terms to first order in the signal, and take the RWA we find

$$\begin{aligned}
& -i\omega_{pump1}\alpha^+e^{-i(\omega_{pump1}t+\phi_{p1})} - i\omega_{pump2}\alpha^-e^{-i(\omega_{pump2}t+\phi_{p2})} + \frac{d\mathbf{d}(t)}{dt} = \\
& -i\omega_{\mathbf{a}}(\alpha^+e^{-i(\omega_{pump1}t+\phi_{p1})} + \alpha^-e^{-i(\omega_{pump2}t+\phi_{p2})} + \mathbf{d}(t)) \\
& -4ig_4\mathbf{d}(t)(\alpha^+)^2 - 4ig_4\mathbf{d}(t)(\alpha^-)^2 - 4ig_4\mathbf{d}(t)^\dagger\alpha^+\alpha^-e^{-i(\phi_{p1}+\phi_{p2})} \\
& -\frac{\kappa_{\mathbf{a}}}{2}(\alpha^+e^{-i(\omega_{pump1}t+\phi_{p1})} + \alpha^-e^{-i(\omega_{pump2}t+\phi_{p2})} + \mathbf{d}(t)) \\
& +\sqrt{\kappa_{\mathbf{a}}}(\alpha_{in}^+e^{-i(\omega_{pump1}t+\phi_{p1})} + \alpha_{in}^-e^{-i(\omega_{pump2}t+\phi_{p2})} + \mathbf{d}_{in}(t))
\end{aligned}$$

As before, the terms containing only α^+ and α^- will correspond to the pump tone, which we will neglect. This leaves us with the equation of motion for the signal in the presence of the pumps

$$\begin{aligned}
\frac{d\mathbf{d}(t)}{dt} &= -i\omega_{\mathbf{a}}\mathbf{d}(t) - 4ig_4\mathbf{d}(t)(\alpha^+)^2 - 4ig_4\mathbf{d}(t)(\alpha^-)^2 \\
& -4ig_4\mathbf{d}(t)^\dagger\alpha^+\alpha^-e^{-i(\phi_{p1}+\phi_{p2})} - \frac{\kappa_{\mathbf{a}}}{2}\mathbf{d}(t) + \sqrt{\kappa_{\mathbf{a}}}\mathbf{d}_{in}(t)
\end{aligned}$$

Moving to the frequency domain and using Eqn. 2.14 to replace the internal modes with

the incoming and outgoing modes this becomes

$$\begin{aligned}
& (i(\omega_a - \omega + 4g_4(\alpha^+)^2 + (\alpha^-)^2) + \frac{\kappa_a}{2}) \mathbf{d}_{out}[\omega] + 4ig_4\alpha^+\alpha^- e^{-i(\phi_{p1}+\phi_{p2})} \mathbf{d}_{out}[-\omega_i]^\dagger = \\
& (-i(\omega_a - \omega + 4g_4((\alpha^+)^2 + (\alpha^-)^2)) + \frac{\kappa_a}{2}) \mathbf{d}_{in}[\omega] - 4ig_4\alpha^+\alpha^- e^{-i(\phi_{p1}+\phi_{p2})} \mathbf{d}_{in}[-\omega_i]^\dagger \\
& (-i(\omega_a - \omega + 4g_4(\alpha^+)^2 + (\alpha^-)^2) + \frac{\kappa_a}{2}) \mathbf{d}_{out}[-\omega_i]^\dagger - 4ig_4\alpha^+\alpha^- e^{i(\phi_{p1}+\phi_{p2})} \mathbf{d}_{out}[\omega] = \\
& (i(\omega_a - \omega + 4g_4((\alpha^+)^2 + (\alpha^-)^2)) + \frac{\kappa_a}{2}) \mathbf{d}_{in}^\dagger[-\omega_i] + 4ig_4\alpha^+\alpha^- e^{i(\phi_{p1}+\phi_{p2})} \mathbf{d}_{in}[\omega]
\end{aligned} \tag{3.2}$$

where $\omega_i = 2\omega_g - \omega$. This looks very similar to the analogous single-pumped four-wave mixing expressions given in Eqn. 2.23. Both have the form

$$\begin{aligned}
& (i(\omega_a - \omega + \Omega) + \frac{\kappa_a}{2}) \mathbf{d}_{out}[\omega] + \Lambda e^{-i\phi_{eff}} \mathbf{d}_{out}[-\omega_i]^\dagger = \\
& (-i(\omega_a - \omega + \Omega) + \frac{\kappa_a}{2}) \mathbf{d}_{in}[\omega] - \Lambda e^{-i\phi_{eff}} \mathbf{d}_{in}[-\omega_i]^\dagger \\
& (-i(\omega_a - \omega + \Omega) + \frac{\kappa_a}{2}) \mathbf{d}_{out}[-\omega_i]^\dagger - \Lambda e^{i\phi_{eff}} \mathbf{d}_{out}[\omega] = \\
& (i(\omega_a - \omega + \Omega) + \frac{\kappa_a}{2}) \mathbf{d}_{in}[-\omega_i]^\dagger + \Lambda e^{i\phi_{eff}} \mathbf{d}_{in}[\omega]
\end{aligned} \tag{3.3}$$

where $\Omega = 4g_4((\alpha^+)^2 + (\alpha^-)^2)$ in the double-pump case and $\Omega = 4g_4(\alpha^p)^2$ in the single-pump case represents a power dependent shift in the resonance frequency, $\Lambda = 4ig_4\alpha^+\alpha^-$ in the double-pump case and $\Lambda = 2ig_4(\alpha^p)^2$ in the single-pump case represents the pump-dependent four-wave mixing term and $\phi_p^{eff} = 2\phi_p$ in the single pump case and $\phi_p^{eff} = \phi_{p1} + \phi_{p2}$ in the double pump case is the effective pump phase. We can then define the effective pump amplitude to be $\rho_{eff} = |\Lambda|/\kappa_a$. Calculating the scattering matrix we then find

$$\begin{bmatrix} \mathbf{d}_{out}[\omega] \\ \mathbf{d}_{out}[-\omega_i]^\dagger \end{bmatrix} = \begin{bmatrix} \sqrt{G} & \sqrt{G_T} e^{-i\phi_p^{eff}} \\ \sqrt{G_T} e^{i\phi_p^{eff}} & \sqrt{G} \end{bmatrix} \begin{bmatrix} \mathbf{d}_{in}[\omega] \\ \mathbf{d}_{in}[-\omega_i]^\dagger \end{bmatrix} \tag{3.4}$$

where the reflected signal power gain is

$$G = 1 + \frac{16\rho_{eff}^2}{(1 - 4\rho_{eff}^2 + \frac{4}{\kappa_a^2}(\Omega - \omega + \omega_a)^2)^2} \tag{3.5}$$

and the trans-gain is

$$G_T = \frac{16\rho_{eff}^2}{(1 - 4\rho_{eff}^2 + \frac{4}{\kappa_a^2}(\Omega - \omega + \omega_a)^2)^2} \quad (3.6)$$

Thus the double-pumped JBA both functions as an amplifier, and can be thought of very analogously to the single-pump JBA. The two pumps act as a single effective pump, but unlike in the single-pump JBA the physical pump tones are located well outside the bandwidth of the device (see Fig. 3.1).

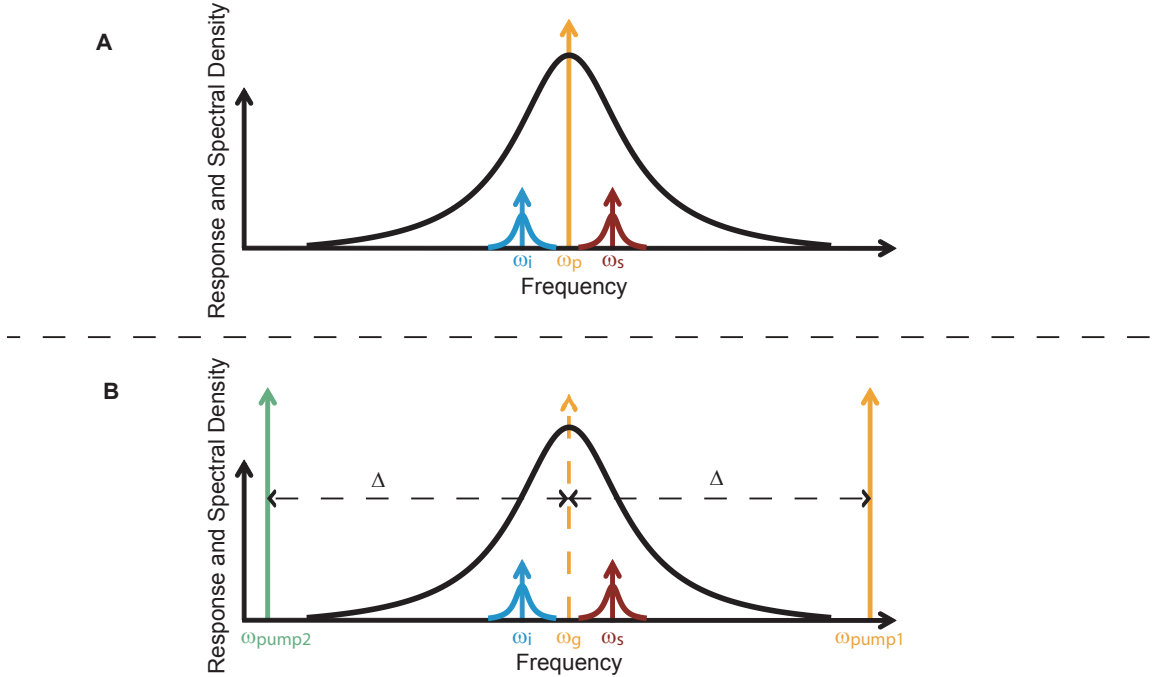


Figure 3.1: Frequency landscape of a single and double-pumped JBA. A) Frequency Schematic of a Single-Pumped JBA. The Lorentzian gain response of the JBA (black) is overlaid on the frequency location of the pump (orange) signal (maroon) and idler (blue) tones. The frequency of the pump, ω_p , corresponds to the frequency of maximum gain. If a small signal (maroon) is applied at the frequency ω_s , it will be amplified in reflection at that frequency (the bandwidth due to the modulation of that signal is represented by the thick maroon response curve) and an additional amplified copy (blue) will be produced at the idler frequency given by $\omega_i = 2\omega_p - \omega_s$. B) Frequency schematic of a double-pumped JBA. The same Lorentzian gain curve can be produced by two pumps at ω_{pump1} and ω_{pump2} . If these two pumps are uniformly detuned from the center of the desired gain curve by an amount Δ , we can think of them as one effective ghost pump (dotted orange arrow) at the center frequency ω_g . If a small signal (maroon) is applied at the frequency ω_s , it will be amplified in reflection at that frequency and an additional amplified copy (blue) will be produced at the idler frequency given by $\omega_i = \omega_{pump1} + \omega_{pump2} - \omega_s$. (Reproduced from Fig. 1.10)

3.2 Pump Stiffness in the JBA

The above derivation assumed that the pump was stiff, or that the dynamics of the pump due to the generation of signal and idler photons are too small to have any impact on the performance of the amplifier. As the incoming signal becomes larger, or the gain of the device becomes higher, more pump photons are destroyed in the amplification process. Eventually these changes in the internal pump field due to the creation of signal and idler photons will be large enough to decrease the instantaneous gain of the device. The question of saturation power was also originally addressed in [56], and it was shown that the double-pumped JBA has a higher saturation power than the single-pumped JBA. Instead of following the method used in [56], we will compare pump stiffness in the single and double-pumped JBA by comparing how the fluctuations of the internal pump field compare to fluctuations of the incoming pump field. This procedure can be found in [33], (and is similar to the procedure in [84]), although those references directly treat a different amplifier. If either the single or double pumped JBA exhibit greater fluctuations than the other for the same incoming pump field, then that device will have a less stiff pump and will be able to process less input signal power.

3.2.1 Pump Dynamics in the Single-Pumped JBA

We can see these effects on the pump field by solving for the pump dynamics using the Langevin equation (Eqn. 2.20). We will keep terms which depend on the pump, and which are rotating around the pump frequency ω_p . This yields

$$\begin{aligned}
 -i\omega_p\alpha^p &= -i\omega_a(\alpha^p + \mathbf{d}(t)) - 2ig_4(2|\alpha^p|^2\mathbf{d}(t) + |\alpha^p|^2\alpha^pe^{-i\phi_p} + 2\alpha^p\mathbf{d}(t)\mathbf{d}(t)^\dagger)e^{-i\phi_p} \\
 &\quad + (\alpha^p)^\dagger\mathbf{d}(t)\mathbf{d}(t)e^{i\phi_p} + |\alpha^p|^2\mathbf{d}(t)^\dagger e^{-2i\phi_p}) + \frac{\kappa_a}{2}\alpha^p = \sqrt{\kappa_a}\alpha_{in}^p
 \end{aligned}
 \tag{3.7}$$

Solving for the average value for the internal pump field this becomes

$$\langle\alpha^p\rangle = \frac{-2ig_4\langle\mathbf{d}(t)\mathbf{d}(t)\rangle\langle(\alpha^p)^\dagger\rangle + \sqrt{\kappa_a}\langle\alpha_{in}^p\rangle}{i(\omega_a - \omega_p) + \frac{\kappa_a}{2} + 2ig_4(\langle|\alpha^p|^2\rangle + 2\langle\mathbf{d}(t)\mathbf{d}(t)^\dagger\rangle)}
 \tag{3.8}$$

We want to find a self-consistent solution for the dynamics of the average internal pump

field in terms of both the incoming pump and signal fields. This needs to be done in a perturbative manner. First we note that the four wave mixing g_4 term is small, and that the incoming pump field is much larger than the signal. This lets us write Eqn. 3.8 as

$$\langle \alpha^p \rangle = \frac{-2ig_4 \langle \mathbf{d}(t) \mathbf{d}(t) \rangle (\langle \alpha_0^p \rangle^\dagger) + \sqrt{\kappa_a} (\langle \alpha_{in}^p \rangle + \langle \mathbf{d}_{in}(t) \rangle)}{i(\omega_a - \omega_p) + \frac{\kappa_a}{2} + 2ig_4 (\langle |\alpha_0^p|^2 \rangle + 2 \langle \mathbf{d}(t) \mathbf{d}(t)^\dagger \rangle)} \quad (3.9)$$

where

$$\alpha_0^p = \frac{\sqrt{\kappa_a} \alpha_{in}^p}{i(\omega_a - \omega_p) + \frac{\kappa_a}{2}} \quad (3.10)$$

Next we will evaluate how the terms relating to the internal signal field given by the terms $\langle \mathbf{d}(t) \mathbf{d}(t) \rangle$ and $\langle \mathbf{d}(t) \mathbf{d}(t)^\dagger \rangle$ relate to the incoming fields. It is easiest to evaluate these terms in the frequency domain, where these terms become

$$\langle \mathbf{d}(t) \mathbf{d}(t) \rangle = \int_{-\infty}^{\infty} \int_{-\infty}^{\infty} \langle \mathbf{d}[\omega] \mathbf{d}[\omega'] \rangle e^{-i(\omega+\omega')t} d\omega d\omega' \quad (3.11)$$

and

$$\langle \mathbf{d}(t) \mathbf{d}(t)^\dagger \rangle = \int_{-\infty}^{\infty} \int_{-\infty}^{\infty} \langle \mathbf{d}[\omega] \mathbf{d}[-\omega']^\dagger \rangle e^{-i(\omega-\omega')t} d\omega d\omega' \quad (3.12)$$

and then by using the input/output relations given in Eqn. 2.14 and the scattering matrix given in Eqn. 3.4 to get

$$\begin{aligned} \langle \mathbf{d}(t) \mathbf{d}(t) \rangle &= \frac{1}{\kappa_a} \int_{-\infty}^{\infty} \int_{-\infty}^{\infty} \left((1 + \sqrt{G})^2 \langle \mathbf{c}_{in}[\omega] \mathbf{c}_{in}[\omega'] \rangle + \sqrt{G_T} (1 + \sqrt{G}) e^{-i\phi_p} \langle \mathbf{c}_{in}[\omega] \mathbf{c}_{in}[-\omega']^\dagger \rangle \right) \\ &\quad + (1 + \sqrt{G}) \mathbf{c}_{in} e^{-i\phi_p} \langle \mathbf{c}[-\omega_i]^\dagger \mathbf{c}_{in}[\omega'] \rangle + G_T \langle \mathbf{c}[-\omega_i]^\dagger \mathbf{c}[-\omega']^\dagger \rangle e^{-i(\omega+\omega')t} d\omega d\omega' \end{aligned} \quad (3.13)$$

and

$$\begin{aligned} \langle \mathbf{d}(t) \mathbf{d}(t)^\dagger \rangle &= \frac{1}{\kappa_a} \int_{-\infty}^{\infty} \int_{-\infty}^{\infty} \left((1 + \sqrt{G})^2 \langle \mathbf{d}_{in}[\omega] \mathbf{d}_{in}[-\omega']^\dagger \rangle + \sqrt{G_T} (1 + \sqrt{G}) e^{-i\phi_p} \langle \mathbf{d}_{in}[\omega] \mathbf{d}_{in}[\omega'] \rangle \right) \\ &\quad + (1 + \sqrt{G}) \mathbf{d}_{in} e^{i\phi_p} \langle \mathbf{d}[-\omega_i]^\dagger \mathbf{d}_{in}[-\omega']^\dagger \rangle + G_T \langle \mathbf{d}[-\omega_i]^\dagger \mathbf{d}[\omega'] \rangle e^{-i(\omega-\omega')t} d\omega d\omega' \end{aligned} \quad (3.14)$$

These depend only on the incoming signal power and the gain of the amplifier. This becomes

even more obvious when we introduce the photon spectral densities \mathcal{N}_{in}^d given by

$$\langle \{ \mathbf{d}_{in}[\omega] \mathbf{d}_{in}[\omega'] \} \rangle = 2\mathcal{N}_{in}^d \left(\frac{\omega - \omega'}{2} \right) \delta(\omega + \omega') \quad (3.15)$$

Evaluating the mean using the photon spectral densities we get

$$\langle \mathbf{d}(t) \mathbf{d}(t) \rangle = \frac{1}{\kappa_a} \int_{-\infty}^{\infty} 2(1 + \sqrt{G})^2 \mathcal{N}_{in}^d(\omega) + 2G_T \mathcal{N}_{in}^d(-\omega) d\omega \quad (3.16)$$

and

$$\langle \mathbf{d}(t) \mathbf{d}(t)^\dagger \rangle = \frac{1}{\kappa_a} \int_{-\infty}^{\infty} \left(2\sqrt{G_T}(1 + \sqrt{G})e^{-i\phi_p} \mathcal{N}_{in}^d(\omega) + 2\sqrt{G_T}(1 + \sqrt{G})e^{i\phi_p} \mathcal{N}_{in}^d(-\omega) \right) e^{-2i\omega} d\omega \quad (3.17)$$

These expressions depend only on the input spectral density to the signal and idler, and on the gain of the amplifier. When comparing the single and double-pumped modes of operation we would like to compare the dynamics of the internal pump field for the same gain and the same input signal powers. Thus we replace these terms with the functions $\gamma_{dd}(G, P_{in}^d)$ and $\gamma_{dd^\dagger}(G, P_{in}^d)$, which will be taken to be the same in both cases.

Substituting into enq. 3.8 we can now express average pump field as a function of the incoming average incoming fields by

$$\langle \alpha^p \rangle = \frac{-2ig_4 \gamma_{dd}(G, P_{in}^d) \langle \alpha_0^p \rangle^\dagger + \sqrt{\kappa_a} \langle \alpha_{in}^p \rangle}{i(\omega_a - \omega_p) + \frac{\kappa_a}{2} + 2ig_4(|\alpha_0^p|^2) + 2\gamma_{dd^\dagger}(G, P_{in}^d)} \quad (3.18)$$

3.2.2 Pump Dynamics in the Double-Pumped JBA

We can perform the same analysis of the double-pumped JBA by starting from the Langevin equation for each of the pumps independently, and trying to find an expression relating the internal pump field in terms of the input fields. Keeping only terms rotating at the pump frequency ω_{pump1} and ω_{pump2} respectively we get

$$\begin{aligned} & -i(\omega_g \pm \Delta)\alpha^{(+,-)} + i\omega_a \alpha^{(+,-)} + 2ig_4(|\alpha^{(+,-)}|^2 \alpha^{(+,-)} + 2|\alpha^{(-,+)}|^2 \alpha^{(+,-)} + \\ & (\alpha^{(-,+)}^\dagger e^{i(\phi_{p1} + \phi_{p2})} \mathbf{d}(t) \mathbf{d}(t) + 2\alpha^{(+,-)} \mathbf{d}(t) \mathbf{d}(t)^\dagger) + \frac{\kappa_a}{2} \alpha^{(+,-)} = \sqrt{\kappa_a} \alpha_{in}^{(+,-)} \end{aligned} \quad (3.19)$$

where $+$ is taken for α^+ and $-$ is taken for α^- . Looking at the average of the dynamics and solving for $\langle\alpha^+\rangle$ and $\langle\alpha^-\rangle$ respectively we get

$$\langle\alpha^{(+,-)}\rangle = \frac{-2ig_4\langle\mathbf{d}(t)\mathbf{d}(t)\rangle\left\langle\left(\alpha_0^{(-,+)}\right)^\dagger\right\rangle + \sqrt{\kappa_a}\langle\alpha_{in}^{(+,-)}\rangle}{i(\omega_a - (\omega_g \pm \Delta)) + \frac{\kappa_a}{2} + 2ig_4\left(2\langle|\alpha_0^{(-,+)}|^2\rangle + \langle|\alpha_0^{(+,-)}|^2\rangle + 2\langle\mathbf{d}(t)\mathbf{d}(t)^\dagger\rangle\right)} \quad (3.20)$$

where analogously

$$\alpha_0^{(+,-)} = \frac{\sqrt{\kappa_a}\alpha_{in}^{(+,-)}}{i(\omega_a - (\omega_p \pm \Delta)) + \frac{\kappa_a}{2}} \quad (3.21)$$

The terms $\langle\mathbf{d}(t)\mathbf{d}(t)\rangle$ and $\langle\mathbf{d}(t)\mathbf{d}(t)^\dagger\rangle$ can again be replaced by the functions $\gamma_{dd}(G, P_{in}^d)$ and $\gamma_{dd^\dagger}(G, P_{in}^d)$, where we will compare single and double pump points with the same amplifier gain G and the same input signal and idler power. This lets us write the average value of the internal field as

$$\langle\alpha^{(+,-)}\rangle = \frac{-2ig_4\gamma_{dd}(G, P_{in}^d)\left\langle\left(\alpha_0^{(-,+)}\right)^\dagger\right\rangle + \sqrt{\kappa_a}\langle\alpha_{in}^{(+,-)}\rangle}{i(\omega_a - (\omega_g \pm \Delta)) + \frac{\kappa_a}{2} + 2ig_4\left(2\langle|\alpha_0^{(-,+)}|^2\rangle + \langle|\alpha_0^{(+,-)}|^2\rangle + 2\gamma_{dd^\dagger}(G, P_{in}^d)\right)} \quad (3.22)$$

The presence of Δ in the denominator of this expression compared that of Eqn. 3.18, as well as the factor of Δ in the denominator of the definitions of $\alpha_0^{(+,-)}$ relative to α_0^p , means that the internal pump field for double-pumped mode of operation will experience a smaller change due to the amplification of incoming signals compared to the internal field of the single-pumped JBA. It also means that fluctuations of the incoming pump field will cause smaller fluctuations in the internal pump field for the double-pumped JBA relative to the single-pumped JBA. This directly translates into the pumps being stiffer in the double-pumped mode of operation.

3.3 Experimental Characterization

3.3.1 Device Description

The JBA used to characterize the double-pumping mode of operation consisted of a SQUID loop with two $3.5 \mu\text{A}$ Josephson junctions defined via electron beam lithography and a

shunting capacitor created from a series combination of two physical 8 pF capacitors composed of a joint niobium bottom plate, a 220 nm dielectric layer of silicon nitride, and two separate top plates of aluminum. As seen in Fig. 3.2 the JBA is then connected to two microwave circulators which allow us to separate input to the JBA from amplified output, and the whole block is attached to the mixing chamber of a dilution refrigerator. A pump tone sourced from a microwave generator and a probe tone sourced from a VNA are combined at room temperature, and applied via the same input line. For the double pumping data, the two pump tones were sourced from physically separate generators locked to the same 10 MHz rubidium clock whose outputs were combined at room temperature before being further combined with the probe tone. A superconducting wire wound magnet is placed below the sample and biased with a DC current to thread an external flux through the SQUID and allow the linear resonance of the circuit to tune in frequency.

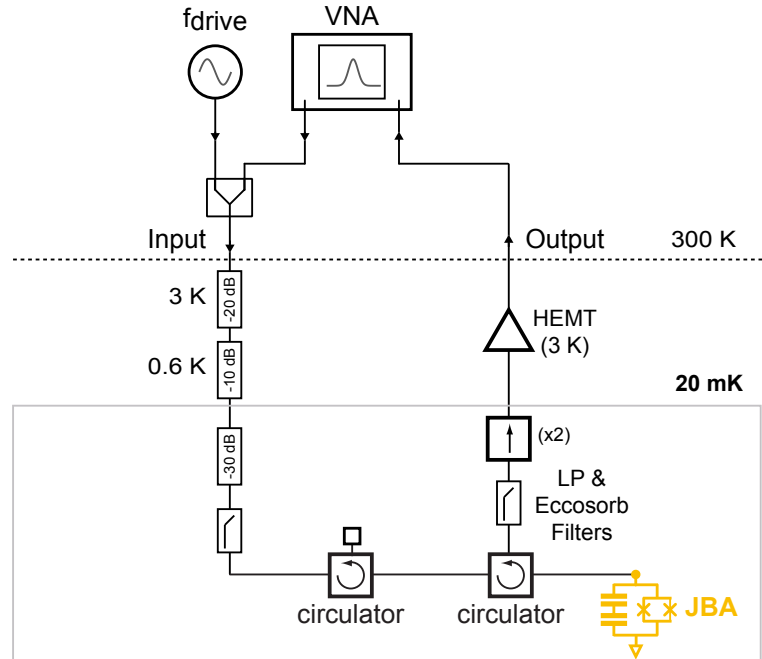


Figure 3.2: Experimental setup for initial characterization of the DP-JBA. Pump tones for the single and double-pumping modes of operation are sourced from generators at room temperature here represented by the single generator at f_{drive} . Pump tones are combined with probe tones sourced from a VNA which then travel down one input line of the fridge to base where they are directed toward the JBA via a two circulators. The reflected output from the amplifier is then directed back up to room temperature where it is measured at the second port of the VNA.

3.3.2 Biasing Protocol

Next we need to develop a protocol for biasing the DP-JBA to achieve a particular amount of gain at a particular frequency. First we need to determine the relative detuning between the frequency of maximum gain, ω_g , and the linear frequency of the circuit, ω_a . We see from Eqn. 3.3 that the linear resonance of the JBA shifts with applied power. Looking back at the expression for the gain (Eqn. 3.5), we can see that the maximum gain of the device will be limited if the detuning between ω_g and ω_a does not compensate for this shift in resonance frequency. Thus, we choose our relative detuning such that the amplifier is capable of achieving high (30+ dB) gains.

Next we need to decide on Δ . A large pump detuning is desirable since it will both minimize the overlap of the pump with the cavity, and increase the pump stiffness of the amplifier. But, as Δ increases the amount of pump power needed to achieve a particular amplifier gain will increase, and may lead to unwanted heating of the refrigerator which will itself cause unwanted back-action in the form of lower qubit coherence times. Additionally, if the detuning is too large then the two pumps may see significantly different attenuations in the lines of the dilution refrigerator, leading to dramatic differences in the amount of power that needs to be sourced at room temperature. We verified that pump detunings from 250 MHz to 1 GHz all resulted in high gains, and chose $\Delta/2\pi = 1$ GHz as a standard value since it resulted in pump tones that were far outside of both the amplifier and cavity bandwidths, but close enough in frequency to not see significantly different line attenuations and to avoid heating the refrigerator.

Next we need an easy way to find the physical pump powers needed to achieve a desired amount of gain. Fig. 3.3 shows the gain of the device as a function of the two pump powers. The gain profile is characterized by a point of highest gain surrounded by concentric contours of different gain points. The contours come from different combinations of individual pump powers that result in the same effective pump power ρ_{eff} . A simple and effective way to navigate this landscape is to find the unique point of maximum gain and equally reduce the individual pump powers until the desired device gain is reached. This methodology easily yields one effective pump power variable. Fig. 3.4 shows a set of gain profiles, from 5 dB

all the way up to 30 dB, taken with the pump powers stepped in this way. The small blip that can be seen at the center frequency of some of the lower gain curves is not some kind of reflected pump like it was in the single pump case, but is instead a hallmark of phase-sensitive amplification. The VNA used to measure these curves has a finite bandwidth, and around the center of the gain curve you have the coherent mixing of signal components with gain G and idler components with gain $G_T e^{-i\phi_p^{eff}}$. All of these curves have the same ω_g because the frequency of the two pumps is kept fixed.

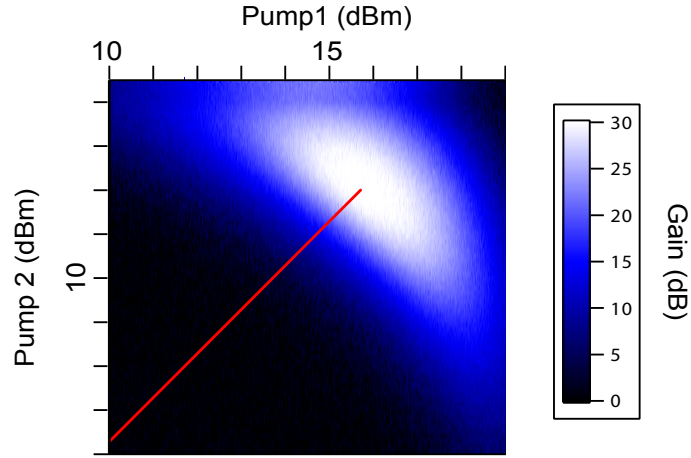


Figure 3.3: Measured double-pumped gain (color) as a function of both pump powers for $\Delta = 1$ GHz. Pump 1 was applied at 4.55 GHz and swept from 10 to 19 dBm (at the output of the generator). Pump 2 was applied at 6.55 GHz and swept from 6 to 14.5 dBm (at the output of the generator). With this pump configuration, depending on the exact values of the single pump powers we can see anywhere from 0 to 30 dB of amplifier gain. The superimposed 45° red line represents the cut through the gain landscape that is taken if the pumps are equally decreased in power from the point of maximum gain.

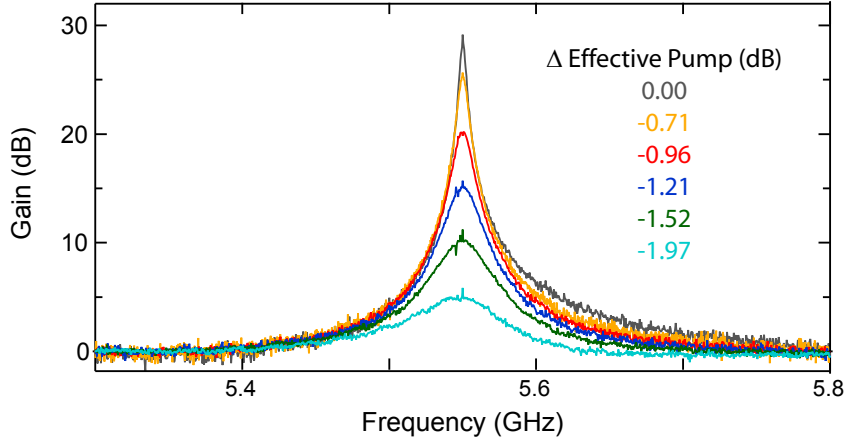


Figure 3.4: Measured DP-JBA gain curves for multiple effective pump powers. Starting from the point of maximum gain as a function of both pumps, we turn down the effective pump power by reducing the power of each individual pump by an equal amount (Δ Effective Pump) while keeping the frequencies and magnetic flux fixed. This allows us to vary the gain of the DP-JBA from the maximum value, here 30 dB, down to whatever value is desired. The small peak or dip that can be seen in the center of the gain curves is not related to the pumps, but is a characteristic feature of phase-sensitive amplification.

3.4 Comparison Between Single and Double-Pumping Amplifier Characteristics

3.4.1 Gain

After confirming that we can achieve amplification with a double-pump JBA, we can compare the properties of the single-pumping and double-pumping modes of operation. As expected from Eqn. 3.5, both are capable of achieving Lorentzian gain of greater than 20 dB of gain with very similar bandwidths. Fig. 3.5 compares the 20 dB gain points from both modes of operation. The single-pumped gain point (red) was taken at with a pump frequency of 5.565 GHz, and the double-pumped gain point (blue) was taken with pumps at 4.55 GHz and 6.55 GHz. The frequency offset arises from the slightly different biasing procedure for the two modes of operation. The single-pump JBA is typically biased by finding the maximum gain as a function of pump power for a given detuning between ω_p and ω_a . A larger detuning between ω_g and ω_a is needed in the double-pumped case to reach high gain, leading to a difference in the central frequency of the two gain profiles. The bandwidth, defined as the full-width of the Lorentzian at a gain 3 dB lower than the

maximum value, is 31 MHz for the single-pump curve and 28 MHz for the double-pumped curve. The most notable difference between these two curves is the absence of the large reflected pump tone at the center of the double-pump gain profile. The double-pump curve does also exhibit reflected pump tones, but they are well outside the frequency range of the figure.

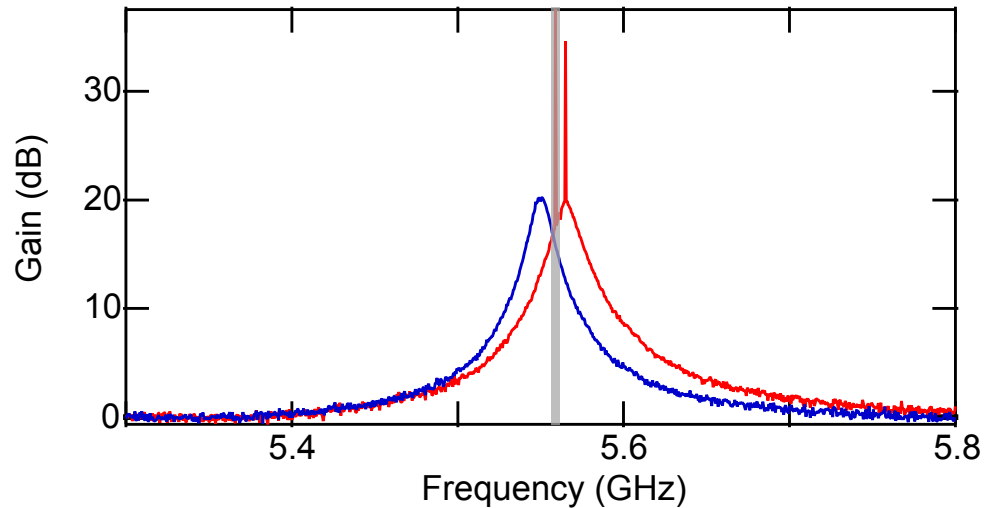


Figure 3.5: Measured 20 dB gain curves from a single-pump (red) and double-pump (blue) JBA. The single pump trace shows the large reflected pump tone at 5.565 GHz, corresponding to the point of maximum gain. It also shows an artificial secondary spike (due to the pump overwhelming mixers in the VNA) to the left of the main gain peak colored in gray. The pumps for the blue trace were located at 4.55 GHz and 6.55 GHz, well removed from maximum gain frequency and outside of the window of the graph.

3.4.2 Added Noise

The JBA is theoretically quantum-limited in both the single and double-pumped modes of operation [56]. The simplest way to characterize the added noise of an amplifier is to look at the noise visibility ratio (NVR), which is defined as the ratio of the noise power received in a spectrum analyzer at room temperature when the amplifier is turned on relative to when the amplifier is turned off. When the JBA is off, noise seen at the output of the fridge is set predominantly by the HEMT, and is relatively flat over a large frequency range. This background is taken to be a NVR of 0 dB. When the amplifier is turned on, a peak in the noise is seen corresponding to the extra narrow band amplification of the JBA along with any extra noise added by the JBA. Fig. 3.6 shows the NVR for the 20 dB single-pump and

double-pump gain curves shown in Fig. 3.5. Although the exact value of the NVR for the single-pumped device is a bit difficult to determine because of the large peak arising from the pump, if we fit single-pump noise profile we can extract a 0.8 dB difference between the single-pump NVR and the double-pump NVR. If we compare the signal to noise ratio given by $G/NVR = 1/(2T_{amp}/T_{sys} + 1/G)$ for the two modes of operation, where T_{amp} is the noise temperature of the amplifier and T_{sys} is the system noise temperature given by the components after the amplifier. If we take T_{sys} to be the same for both the single and double-pumped JBA, we find $T_{amp}^{DP}/T_{amp}^{SP} = 1.2$. Thus the double-pumped mode of operation does not add significantly more noise than the single-pumped mode of operation. A better measure of the added noise of the double-pumped JBA will be presented in the next chapter, where we will use a qubit as a calibrated noise source to find the measurement efficiency of a measurement chain based around the DP-JBA.

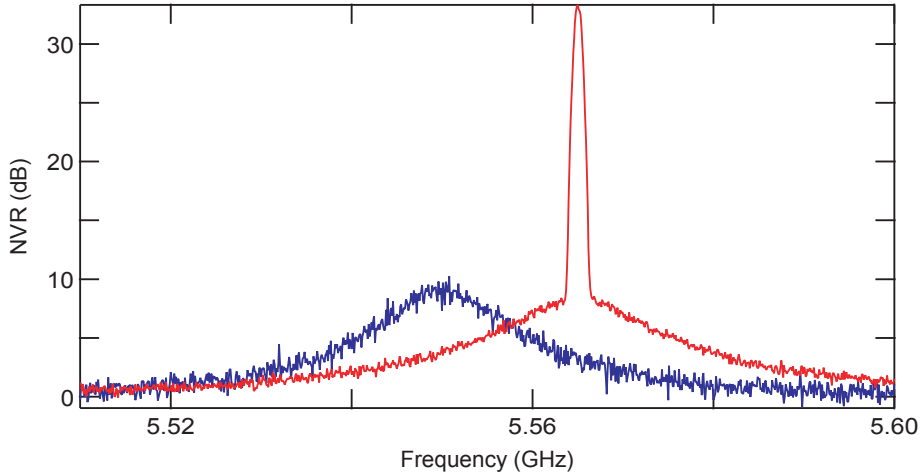


Figure 3.6: Noise Visibility Ratio for a 20 dB single-pump (red) and double-pump (blue) gain curve. The large peak in the single-pump NVR curve arises from the pump.

3.4.3 Saturation Power

As shown in section 3.2, we expect the pumps for the double-pumped mode of operation to be stiffer than the pump for the single-pumped mode of operation. We can verify this experimentally by comparing the saturation power for the two devices, that is how much input power each mode of operation can process for a given amount of gain before pump depletion causes the observed gain to fall. The insert of Fig. 3.7 shows the measured

amplifier gain as a function of input power for several unsaturated amplifier gains. If we examine just one of those curves, we find a range of input powers over which the effects of pump depletion are small and the measured gain of the amplifier is constant. Once the input power reaches some critical level the effects of pump depletion start to be significant and the gain starts to fall. We then extract the input power at which the gain has fallen by 1 dB, known as the $P_{-1\text{dB}}$ power. The value of the gain taken for the double-pumped JBA is taken at ω_g , while the value of the gain for the single-pumped JBA is taken slightly off resonance to avoid contamination by the large reflected pump tone. Fig. 3.7 then compares the $P_{-1\text{dB}}$ powers, the single and double-pumped modes of operation for several different unsaturated amplifier gains. For all gain points, the double-pumped JBA shows a higher $P_{-1\text{dB}}$ power, and thus a stiffer pump, as expected from section 3.2.

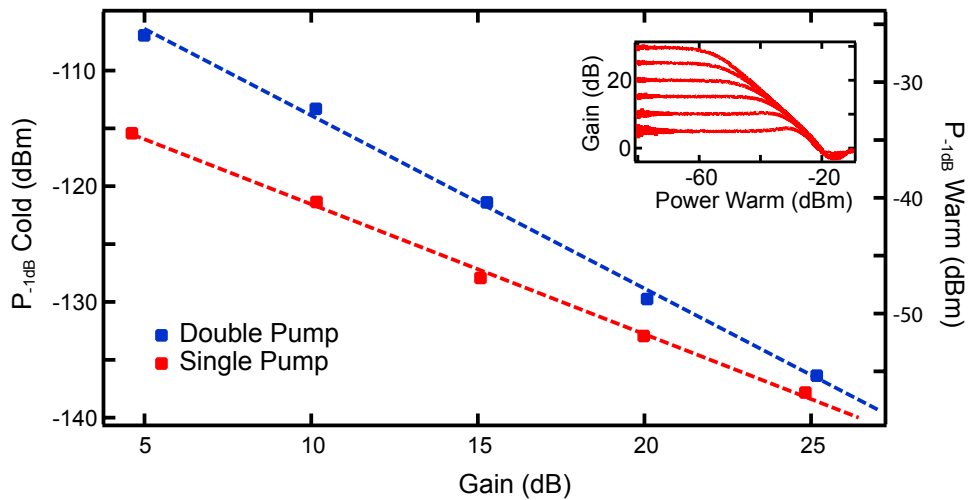


Figure 3.7: Saturation power for the single vs double-pumped JBA. We compare the $P_{-1\text{dB}}$ powers for both the single pumped (red) and double pumped (blue) mode of operation. This input power is given both at the plane of the VNA (warm) and at the plane of the amplifier, as estimated from the measured input line attenuation, (cold) for a variety of unsaturated amplifier gains. For all amplifier gains, the amplifier can tolerate a higher input power before saturating while being double-pumped compared to being single-pumped. Insert: Individual gain versus input power traces for several amplifier gains. While in the unsaturated regime the gain is independent of pump power and the curve remains flat. Then once a certain threshold is reached the gain begins to drop as the amplifier saturates. The $P_{-1\text{dB}}$ power is defined as the warm input power at which the gain of the amplifier falls 1 dB below the constant value it starts with at low input powers.

3.5 Comparison of Qubit Dephasing with the Single and Double-Pumped JBA

We expect less qubit dephasing when measuring with a DP-JBA because the two pump tones are spectrally separated from the cavity. We measured the Ramsey decoherence times of a transmon qubit [85] in a copper cavity [86] with frequency $\omega_q/(2\pi) = 4.419$ GHz and longitudinal decay and Ramsey decoherence times $T_1 = 21 \mu\text{s}$ and $T_{2R} = 6.6 \mu\text{s}$, respectively. The qubit, with antenna length 1.1 mm and width 250 μm , is placed in a 3D copper cavity with resonance frequency $\omega_c^g/(2\pi) = 7.428$ GHz when the qubit is in the ground state, resulting in a dispersive shift $(\omega_c^g - \omega_c^e)/(2\pi) = \chi/2\pi = 4.27$ MHz. It is asymmetrically coupled to input and output transmission lines ($Q_{in}^c = 90000$, $Q_{out}^c = 1700$) resulting in a decay rate of the readout mode of $\kappa/2\pi = 4.3$ MHz. We used a different JBA from the one in the previous section. This JBA was composed of two $4\mu\text{A}$ Josephson junctions which formed the SQUID loop and had a total shunting capacitance of 4.25 pF.

A detailed diagram of the setup for qubit measurements with the single and double-pumped JBA is shown in Fig. 3.8. The cavity and the JBA are connected via two circulators and a directional coupler, which are all then mounted at the base of a dilution refrigerator. The circulator directly connected to the JBA was used to separate input from amplified output, with the third port leading to higher stages of amplification and our demodulation setup. The directional coupler was used to apply pumps to the JBA, and the circulator closest to the cavity served as a way to probe the amplifier through the diagnostic port for tuning. For the single-pump mode of operation, the cavity drive is sourced from a generator at f_{drive} that is then shaped by an Arbitrary Waveform Generator (AWG). The pump for the JBA is sourced from a physically separate generator and applied to the weakly coupled port of the directional coupler.

We will be using the JBA to perform phase-sensitive amplification. As shown in the previous chapter, it is the relative phase between the pump and the signal which determines which quadrature is amplified. When we sourced the two pump tones and the cavity tone via three separate generators locked to a common 50 MHz rubidium clock, as discussed previously, we saw significant drifts in the relative phase, and the amplifier required frequent

retuning to avoid drifts in which quadrature was being amplified. We addressed this issue by generating the cavity drive and pump tones from a single set of generators as seen in Fig. 3.9. The two pumps for the JBA are generated by mixing two tones, one at f_{drive} which also corresponds to both the readout frequency for the cavity and the frequency of maximal gain for the DP-JBA, and the other at the desired pump detuning frequency f_{Δ} . This results in one pump at $f_{drive} + f_{\Delta}$ and the other at $f_{drive} - f_{\Delta}$. The use of an IQ mixer along with a variable attenuator and phase shifter on one arm of the IQ input allows us to have independent amplitude control over the two final pump tones. A second variable attenuator is included after the mixer to allow us to change the power of both pumps simultaneously and easily change the total gain of the amplifier. The pumps are then applied to the JBA via a directional coupler as before. The cavity drive is created from another branch of f_{drive} which is then passed through a variable phase shifter and is then shaped with an AWG as before. Drifts in the phase of f_{drive} now equally affect both JBA pump phase, and the relative phase between the drive and the pumps is now set by the physical variable phase shifter on the cavity drive arm. With this configuration the relative phase only needs to be re-tuned only every day or so, allowing for more involved experiments.

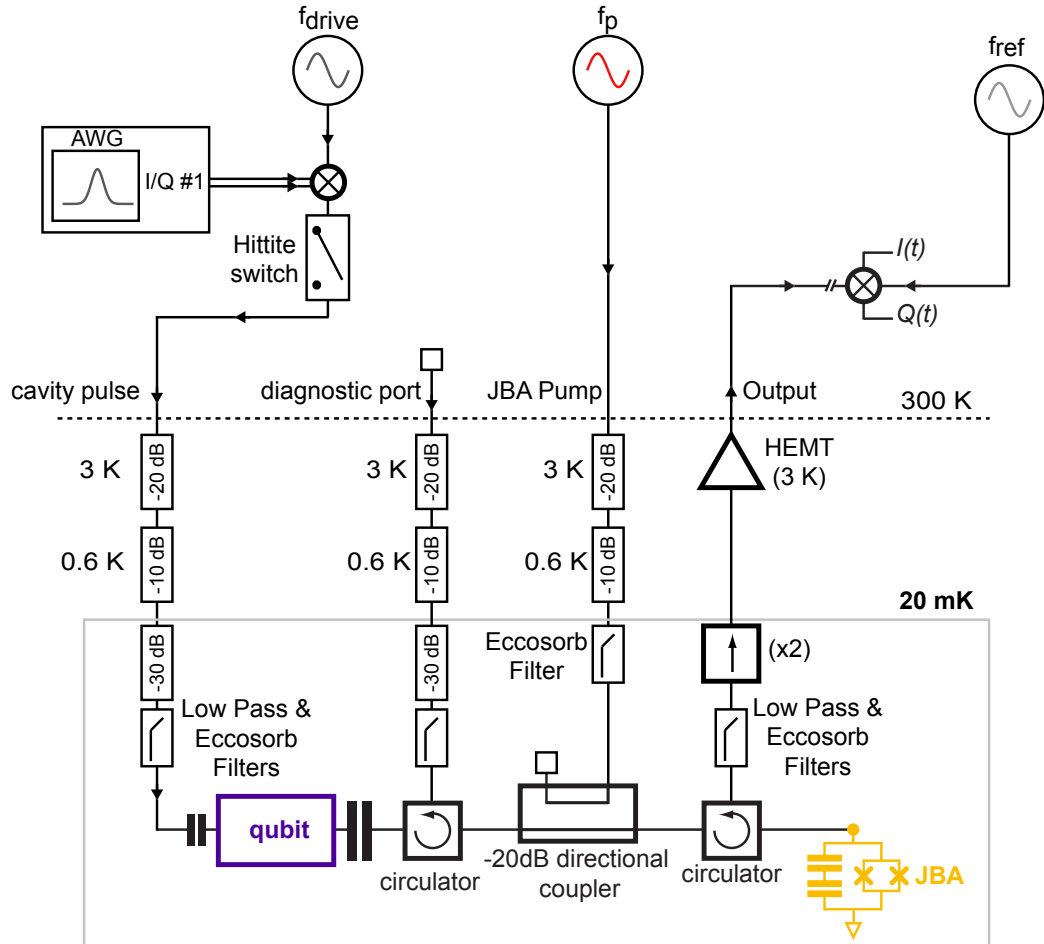


Figure 3.8: Experimental setup for the single-pump JBA: A generator at f_{drive} which is shaped by an AWG creates the readout pulse for the cavity. A microwave switch is included to ensure no leakage power is transmitted to the cavity when the readout is off. The readout pulse exits the cavity where it passes through two circulators and a directional coupler before being amplified with a JBA and finally is directed toward higher stages of amplification and demodulation. The pump for the JBA is sourced from a generator at f_p and combined with the signal from the cavity via a directional coupler at base.

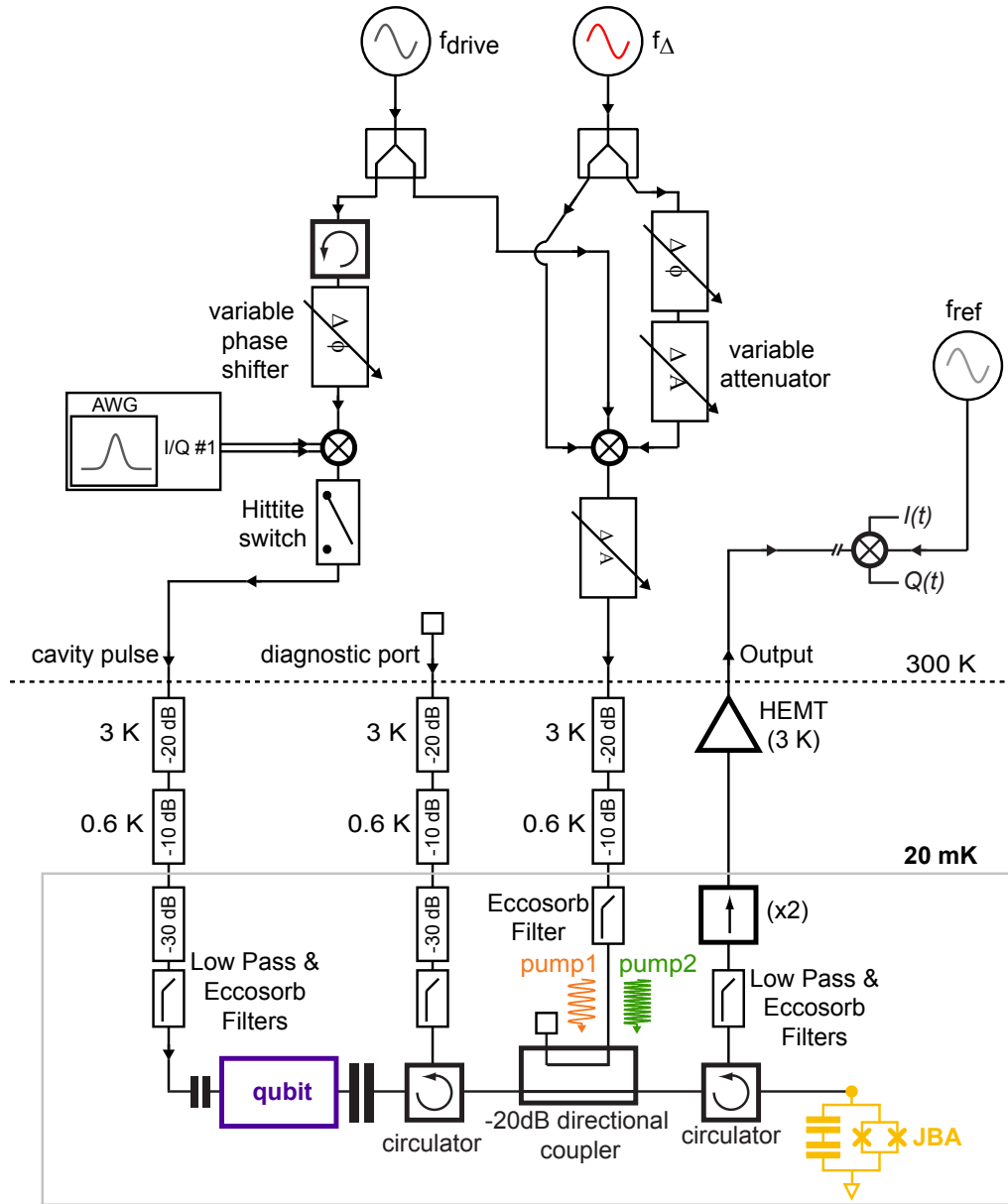


Figure 3.9: Experimental setup for the double-pump JBA: f_{drive} is set to the cavity frequency and split three ways. The left branch forms the cavity measurement pulse after a manual phase shifter, an IQ mixer connected to an AWG for pulse shaping and switch. The right branch is mixed with our detuning frequency to create the two pump tones which are applied to the DP-JBA via a directional coupler. The variable phase shifter and variable attenuator on one arm of the split detuning drive allow separate amplitude control of the two pumps. In between the cavity and the DP-JBA there are two circulators used both to direct pulses and to provide extra isolation to the qubit.

To quantify the dephasing induced by the two modes of pumping we looked at the Ramsey decoherence time (T_{2R}) of the qubit while amplifying along the I quadrature. It is measured by first applying a detuned $R_x(\pi/2)$ pulse to the qubit, then waiting a variable amount of time for the qubit state to evolve, and then applying a second detuned $R_x(\pi/2)$ pulse followed by a measurement pulse. This results in an oscillating signal with a frequency that corresponds to the detuning of the $R_x(\pi/2)$ pulses, and an exponentially decaying envelope whose decay constant is the Ramsey decoherence time. This decoherence time is a combination of the pure dephasing time given by twice the characteristic decay time of the excited state of the qubit, and an added dephasing time. In the case of the single-pump JBA, the primary contribution to the added dephasing time is the presence of excess photons in the cavity, which happens at a rate $\gamma_\phi = 2\bar{n}\kappa \sin^2(\theta/2)$ [16]. At a 20 dB single pump gain point the Ramsey dephasing curves for the amplifier on and the amplifier off are shown in Fig. 3.10. The decrease in phase coherence from 8 μs to 290 ns indicates the single-pump mode of operation is adding an addition 28 average photons to the cavity. For the double-pump mode of operation (Fig. 3.11) the phase coherence only decreased from 6.8 μs to 5.2 μs , putting a limit on the added average photon number of only 1.

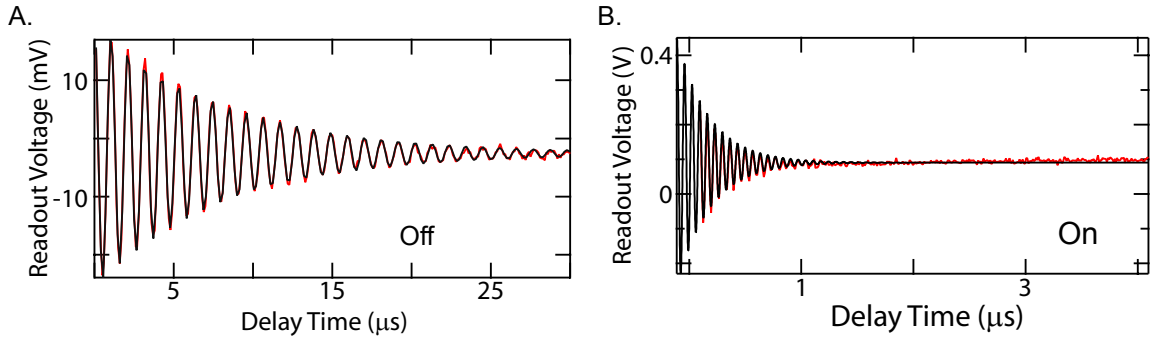


Figure 3.10: Measured Ramsey dephasing time of a qubit when amplified with a single-pumped JBA. The dephasing time without any amplification was 8 μs . This decreased to 290 ns when the amplifier is turned on, corresponding to an average of 28 photons in the cavity due to the large reflected pump tone. (Reproduced from Fig. 1.12)

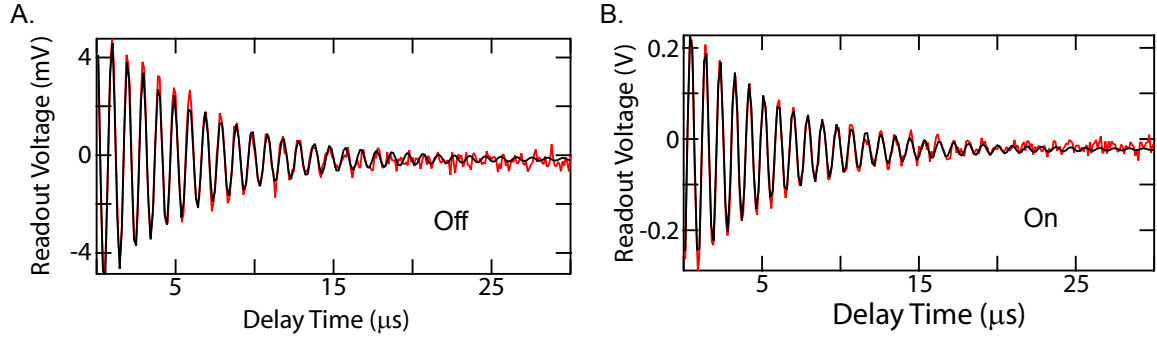


Figure 3.11: Measured Ramsey dephasing time of a qubit when amplified with a double-pumped JBA. The dephasing time without any amplification was $6.8 \mu\text{s}$, which only decreased to $5.2 \mu\text{s}$ when the amplifier was turned on, corresponding to only 1 additional photon in the cavity. (Reproduced from Fig. 1.13)

We conclude that double-pumping the JBA is a stable, reliable method of minimizing the dephasing typically seen with the single-pump mode of operation, and increases the saturation power of the amplifier. As we will see in the next chapter, using this mode of operation allows us to begin to investigate the Heisenberg back-action of phase-sensitive amplification using the DP-JBA.

Chapter 4

Quantum Operations with Parametric Amplifiers

In addition to being an essential component to the measurement chain used to readout superconducting qubits, parametric amplification can be used to manipulate them as well. For instance, the Heisenberg back-action associated with parametric amplification can perform essential function such as the remote entanglement of distant qubits [9,23,28,87]. But Heisenberg back-action is a delicate phenomena. The JPC in its standard mode of operation already allows us to observe the Heisenberg back-action of phase-preserving amplification [11], but the qubit dephasing arising from the strong reflected pump tone prevented a similar measurement with the JBA. Double-pumping the JBA, as described in the last chapter, minimizes this effect enough to allow us to observe the Heisenberg back-action of phase-sensitive amplification as well.

As will be explained in this chapter, the fragility of Heisenberg back-action can be an advantage. It can be used for an accurate, self-calibrating determination of our measurement efficiency. These types of measurements will be vital in identifying and eliminating the remaining effects which limit our ability to manipulate quantum systems by the Heisenberg back-action of measurement.

4.1 Heisenberg Back-Action of Phase-Sensitive Amplification Along the I Quadrature

Understanding the Heisenberg back-action of a parametric amplification process is easier if we break the measurement process down into a series of steps [1, 11]. Following the procedure explicitly calculated in [11], but done here for phase-sensitive amplification as opposed to phase-preserving amplification, we first entangle the state of the qubit, $\Psi = c_g |g\rangle + c_e |e\rangle$ with the coherent state used to probe the cavity $|\alpha\rangle$, resulting in the joint state $c_g |g\rangle \otimes |\alpha_g\rangle + c_e |e\rangle \otimes |\alpha_e\rangle$. This joint state then propagates to the input of a degenerate phase-sensitive amplifier such as the JBA, where the amplifier will perform a unitary operation on the quadratures of the input state. A measurement is then made on the state leaving the amplifier, resulting in the outcome I_m and a collapse of the output mode into the eigenstate $|\Psi_{I_m}\rangle$ where $\mathbf{I}|\Psi_{I_m}\rangle = I_m|\Psi_{I_m}\rangle$. The new joint, but no longer entangled, state of the system is then given by $(c_g \langle \Psi_{I_m} | \alpha_g \rangle |g\rangle + c_e \langle \Psi_{I_m} | \alpha_e \rangle |e\rangle) \otimes |\Psi_{I_m}\rangle$.

Calculating the back-action of the measurement on the qubit state is thus equivalent to calculating the Kraus operator [2] for phase-sensitive amplification given by [88]

$$M_{I_m} = \begin{pmatrix} \langle \Psi_{I_m} | \alpha_g \rangle & 0 \\ 0 & \langle \Psi_{I_m} | \alpha_e \rangle \end{pmatrix} = \frac{e^{-\frac{\bar{Q}_m^2}{4\sigma_I^2}}}{(2\pi)^{1/4} \sigma_I^{1/2}} \begin{pmatrix} e^{-\frac{(I_m - (-\bar{I}_m + i\bar{Q}_m))^2}{4\sigma_I^2}} & 0 \\ 0 & e^{-\frac{(I_m - (\bar{I}_m + i\bar{Q}_m))^2}{4\sigma_I^2}} \end{pmatrix} \quad (4.1)$$

where I_m is a particular measurement outcome, the probability distribution of which is centered around \bar{I}_m with standard deviation

$$\sigma_I^2 = \sigma_{\text{Heis}}^2 = 1/4 \quad (4.2)$$

If we represent the initial qubit state by its density matrix ρ_i , then the effect of the mea-

surement is to transform the density matrix via

$$\rho_i \xrightarrow{\text{msmt}} \rho_f(I_m) = \frac{M_{I_m} \rho_i M_{I_m}^\dagger}{\text{Tr}(M_{I_m} \rho_i M_{I_m}^\dagger)} \quad (4.3)$$

where $\sum_{I_m} M_{I_m}^\dagger M_{I_m} = 1$. If we take the qubit to originally be pointing along the y -axis so $(x_i, y_i, z_i) = (0, 1, 0)$, and take the Q quadrature to be perfectly squeezed, then we can explicitly calculate the final Bloch vector to be

$$\begin{aligned} x_f^I &= 0 \\ y_f^I &= \text{sech}\left(\frac{I_m \bar{I}_m}{\sigma_I^2}\right) \\ z_f^I &= \tanh\left(\frac{I_m \bar{I}_m}{\sigma_I^2}\right) \end{aligned} \quad (4.4)$$

This result corresponds to motion in the $y - z$ plane, with the extent of the motion varying with the strength of the measurement, here parametrized by \bar{I}_m/σ_I . For small \bar{I}_m/σ_I the back-action looks like a stochastic hyperbolic rotation in the $y - z$ plane with the degree of rotation encoded in I_m . All outcomes are possible, and the measurement strength determines their relative probabilities. As the measurement strength increases, $y_f \rightarrow 0$ and $z_f \rightarrow \pm 1$ with $+1$ corresponding negative I_m results and -1 corresponding to positive I_m results. This is exactly what we expect from a text-book strong projective measurement as presented in chapter 2. The final qubit state will be one of the two poles of the Bloch sphere, with $|g\rangle$ corresponding to $I_m < 0$ results and $|e\rangle$ corresponding to $I_m > 0$ results.

In practice, we are still not able to remove all of the sources of added noise from our measurement. We can include these effects on the final state of the qubit Bloch vector by taking

$$\sigma_I^2 = \sigma_{\text{Heis}}^2 + \sigma_{\text{add}}^2 \quad (4.5)$$

where the measurement efficiency is given by $\eta = \sigma_{\text{Heis}}^2/\sigma_I^2$, and then taking the weighted sum of all of the perfect measurement results I which, under the effects of the additional back-action, could have resulted in the imperfect measurement result I_m . This yields the

final Bloch vector components $(x, y, z)_f^I$ given by

$$\begin{aligned} x_f^I(I_m) &= \int \mathbb{P}(I|I_m)x_f(I) dI \\ y_f^I(I_m) &= \int \mathbb{P}(I|I_m)y_f(I) dI \\ z_f^I(I_m) &= \int \mathbb{P}(I|I_m)z_f(I) dI \end{aligned} \quad (4.6)$$

where the weighting factor $\mathbb{P}(I|I_m)$ is the conditional probability that a perfect measurement would have given the outcome I given that our imperfect measurement gave the result I_m . We can calculate this conditional probability via the quantum Bayes rule

$$\mathbb{P}(I|I_m) = \frac{\mathbb{P}(I_m|I)P(I)}{\int dI\mathbb{P}(I_m|I)P(I)} \quad (4.7)$$

where

$$P(I) = \text{Tr}(M_{I_m}\rho_i M_{I_m}^\dagger) = \frac{1}{\sqrt{8\pi\sigma_{\text{Heis}}^2}} \left(e^{-\frac{(I-\bar{I}_m)^2}{2\sigma_{\text{Heis}}^2}} + e^{-\frac{(I+\bar{I}_m)^2}{2\sigma_{\text{Heis}}^2}} \right) \quad (4.8)$$

is the probability of obtaining outcome I for a perfect measurement and

$$\mathbb{P}(I_m|I) = \frac{1}{\sqrt{2\pi\sigma_I^2(1-\eta)}} e^{-\frac{(I_m-I)^2}{2(1-\eta)\sigma_I^2}} \quad (4.9)$$

is the probability the perfect measurement result I corresponds to the imperfect measurement result I_m . This yields

$$\int dI\mathbb{P}(I_m|I)P(I) = \frac{1}{\sqrt{8\pi\sigma_I^2}} \left(e^{-\frac{(I_m-\bar{I}_m)^2}{2\sigma_I^2}} + e^{-\frac{(I_m+\bar{I}_m)^2}{2\sigma_I^2}} \right) \quad (4.10)$$

and thus

$$\mathbb{P}(I|I_m) = \frac{e^{-\frac{(I_m-I)^2}{2(1-\eta)\sigma_I^2}} \left(e^{-\frac{(I-\bar{I}_m)^2}{2\sigma_{\text{Heis}}^2}} + e^{-\frac{(I+\bar{I}_m)^2}{2\sigma_{\text{Heis}}^2}} \right)}{\sqrt{2\pi\eta(1-\eta)\sigma_I^2} \left(e^{-\frac{(I_m-\bar{I}_m)^2}{2\sigma_I^2}} + e^{-\frac{(I_m+\bar{I}_m)^2}{2\sigma_I^2}} \right)} \quad (4.11)$$

Now we can calculate the effect of an imperfect measurement chain on the final Bloch vector, again assuming we start in the state $(0,1,0)$, and find

$$\begin{aligned} x_f^I &= 0 \\ y_f^I &= \operatorname{sech} \left(\frac{I_m \bar{I}_m}{\sigma_I^2} \right) e^{-\frac{\bar{I}_m^2}{2\sigma_I^2} \left(\frac{1-\eta}{\eta} \right)} \\ z_f^I &= \tanh \left(\frac{I_m \bar{I}_m}{\sigma_I^2} \right) \end{aligned} \quad (4.12)$$

Finite measurement efficiency has two effects. The first is to decrease the apparent measurement strength \bar{I}_m/σ_I since σ_I is now larger due to the added contribution from the added non-Heisenberg noise, and the second is to induce reduction in the y-component of the final qubit state, and thus the magnitude of the Bloch vector, due to information losses. This information loss can be interpreted as dephasing of the qubit.

4.2 Heisenberg Back-Action of Phase-Sensitive Amplification Along the Q Quadrature

The case of phase-sensitive amplification along the Q quadrature starts off with the same entangled state $c_g |g\rangle \otimes |\alpha_g\rangle + c_e |e\rangle \otimes |\alpha_e\rangle$ which will again propagate toward the amplifier. In this case, the amplifier will apply a different unitary, and a measurement will result in an eigenstate of the output mode $|\Psi_{Q_m}\rangle$ where $\mathbf{Q} |\Psi_{Q_m}\rangle = Q_m |\Psi_{Q_m}\rangle$. The new joint, but no longer entangled, state of the system is then given by $(c_g \langle \Psi_{Q_m} | \alpha_g \rangle |g\rangle + c_e \langle \Psi_{Q_m} | \alpha_e \rangle |e\rangle) \otimes |\Psi_{Q_m}\rangle$ where we have assumed perfect de-amplification of the I quadrature.

We will keep the same convention used in the previous section, where the measurement strength is parameterized by the value \bar{I}_m/σ_I . This is possible if we take our plane of

reference to be the input of the amplifier, where $\sigma_I^2 = \sigma_Q^2 = 1/4$. We can again find the new state of the qubit by calculating the Kraus map for phase-sensitive amplification along the Q quadrature, given by [88]

$$M_{Q_m} = \begin{pmatrix} \langle \Psi_{Q_m} | \alpha_g \rangle & 0 \\ 0 & \langle \Psi_{Q_m} | \alpha_e \rangle \end{pmatrix} = \frac{e^{-\frac{\bar{I}_m^2}{4\sigma_I^2}}}{(2\pi)^{1/4} \sigma_I^{1/2}} \begin{pmatrix} e^{-\frac{(Q_m - i(-\bar{I}_m + i\bar{Q}_m))^2}{4\sigma_I^2}} & 0 \\ 0 & e^{-\frac{(Q_m - i(\bar{I}_m + i\bar{Q}_m))^2}{4\sigma_I^2}} \end{pmatrix} \quad (4.13)$$

Starting from the same initial state $\rho_i = (0, 1, 0)$, we can calculate the final qubit Bloch vector

$$\begin{aligned} x_f^Q &= \sin\left(\frac{Q_m \bar{I}_m}{\sigma_I^2}\right) \\ y_f^Q &= \cos\left(\frac{Q_m \bar{I}_m}{\sigma_I^2}\right) \\ z_f^Q &= 0 \end{aligned} \quad (4.14)$$

The back-action for amplification along this quadrature is fundamentally different. The operation kicks the qubit to a new position on the equator of the Bloch sphere, with the resulting azimuthal angle encoded in the outcome Q_m . This process is stochastic because the measurement outcome is a-priori unknown. As before, all angles are accessible, with their relative likelihoods determined by measurement strength still given by \bar{I}_m/σ_I . Furthermore, if we view this process as a stochastic Ramsey rotation, then the frequency of the oscillation in x_f^Q and y_f^Q is determined by the measurement strength. We emphasize that this back-action is not the result of variation of the cavity-qubit interaction, but instead is determined by the choice of amplified quadrature which can be made on the fly after the coherent state has left the cavity.

We can again add in the effects of an imperfect measurement chain via added classical noise in the same way as we did for amplification along the I quadrature, finding

$$\mathbb{P}(Q_m|Q) = \frac{1}{\sqrt{2\pi\sigma_I^2(1-\eta)}} e^{-\frac{(Q_m-Q)^2}{2(1-\eta)\sigma_I^2}}$$

and

$$P(Q) = \frac{1}{\sqrt{2\pi\sigma_I^2}} e^{-\frac{(Q-\bar{Q}_m)^2}{2\sigma_I^2}}$$

thus,

$$\mathbb{P}(Q|Q_m) = \frac{1}{\sqrt{2\pi(1-\eta)\eta\sigma_I^2}} e^{-\frac{(Q-\bar{Q}_m(1-\eta)-Q_m\eta)^2}{2(1-\eta)\eta\sigma_I^2}} \quad (4.15)$$

We then calculate the final Bloch vector for amplification along the Q -quadrature in the case of an imperfect measurement chain via

$$\begin{aligned} x_f^Q(Q_m) &= \int \mathbb{P}(Q|Q_m) x_f(Q) dQ \\ y_f^Q(Q_m) &= \int \mathbb{P}(Q|Q_m) y_f(Q) dQ \\ z_f^Q(Q_m) &= \int \mathbb{P}(Q|Q_m) z_f(Q) dQ \end{aligned} \quad (4.16)$$

and find

$$\begin{aligned} x_f^Q &= \sin\left(\frac{Q_m\bar{I}_m}{\sigma_I^2} + \frac{\bar{I}_m\bar{Q}_m}{\sigma_I^2} \left(\frac{1-\eta}{\eta}\right)\right) e^{-\frac{\bar{I}_m^2}{2\sigma_I^2} \left(\frac{1-\eta}{\eta}\right)} \\ y_f^Q &= \cos\left(\frac{Q_m\bar{I}_m}{\sigma_I^2} + \frac{\bar{I}_m\bar{Q}_m}{\sigma_I^2} \left(\frac{1-\eta}{\eta}\right)\right) e^{-\frac{\bar{I}_m^2}{2\sigma_I^2} \left(\frac{1-\eta}{\eta}\right)} \\ z_f^Q &= 0 \end{aligned} \quad (4.17)$$

Here the effects of non-Heisenberg noise are much more apparent. The reduced measurement efficiency serves to both give an offset to the stochastic Ramsey fringes, and more importantly reduces the contrast of the fringes. For very low η , this effect will not be visible at all. We can thus use the contrast of these fringes as a direct measurement of η .

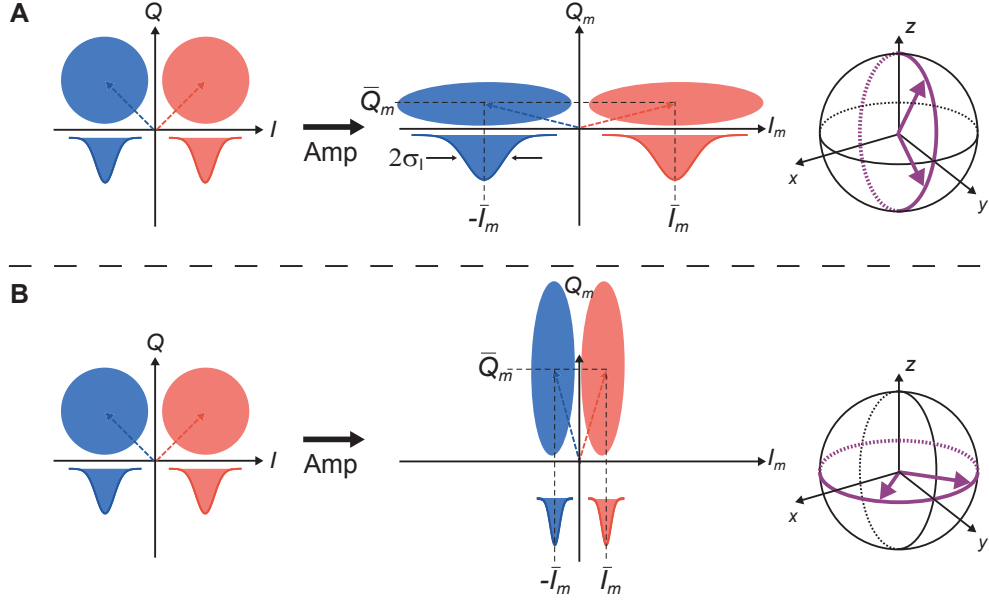


Figure 4.1: Heisenberg back-action of phase-sensitive amplification. A) Fresnel lollipop representation of the joint qubit and signal coherent state before and after phase-sensitive amplification along the I quadrature. The back-action resulting on the qubit from this unitary applied to the coherent state is a stochastic kick along lines of longitude, with the projection of the kick along z encoded in I_m . B) Fresnel lollipop representation of the coherent state before and after phase-sensitive amplification along the Q quadrature. The resulting Heisenberg back-action is a stochastic kick along lines of latitude, with the the magnitude of the kick encoded in Q_m . This is representative of the non-trivial types of Heisenberg back-action that can be observed after other unwanted types of back-action are well controlled and minimized. (Reproduced from Fig. 1.15)

4.3 Heisenberg Back-Action of Phase-Preserving Amplification

Phase-preserving amplification treats the two quadratures on the same footing, so we should expect to see both the stochastic kick along lines of longitude that we saw encoded in the I_m outcome and the stochastic Ramsey rotation along lines of latitude encoded in the Q_m outcome. One potential complication of phase-preserving amplification is the need to explicitly include the idler. We can do this by writing the input state as $c_g |g\rangle \otimes |\alpha_g, 0\rangle + c_e |e\rangle \otimes |\alpha_e, 0\rangle$ where the input to the signal comes from the cavity and is represented by $c_g |g\rangle \otimes |\alpha_g\rangle + c_e |e\rangle \otimes |\alpha_e\rangle$ and the 0 represents the vacuum input to the idler. Phase-preserving amplification corresponds to an addition of the signal and idler inputs (see section 2.1.2), so the observables in this case are not I and Q , but are instead $I_{pp} = I_{\text{signal}} + Q_{\text{idler}}$

and $\mathbf{Q}_{pp} = \mathbf{Q}_{\text{signal}} + \mathbf{I}_{\text{idler}}$. A measurement will project us into an eigenstate $|\Psi_{I_m, Q_m}\rangle$ where $\mathbf{I}_{pp}|\Psi_{I_m, Q_m}\rangle = I_m|\Psi_{I_m, Q_m}\rangle$ and $\mathbf{Q}_{pp}|\Psi_{I_m, Q_m}\rangle = Q_m|\Psi_{I_m, Q_m}\rangle$. The back-action of phase-preserving amplification in both the ideal and non-idea case was explicitly calculated in [11]. The Kraus map for this type of amplification is given by

$$M_{I_m, Q_m} = \begin{pmatrix} \langle \Psi_{I_m, Q_m} | \alpha_g, 0 \rangle & 0 \\ 0 & \langle \Psi_{I_m, Q_m} | \alpha_e, 0 \rangle \end{pmatrix} \quad (4.18)$$

$$= \frac{1}{\sqrt{\pi}} e^{-\frac{(Q_m - \bar{Q}_m)^2}{4\sigma_I^2}} \begin{pmatrix} e^{-\frac{(I_m + \bar{I}_m)^2}{4\sigma_I^2}} e^{\frac{i\bar{I}_m Q_m}{2\sigma_I^2}} & 0 \\ 0 & e^{-\frac{(I_m - \bar{I}_m)^2}{4\sigma_I^2}} e^{-\frac{i\bar{I}_m Q_m}{2\sigma_I^2}} \end{pmatrix} \quad (4.19)$$

where here $\sigma_I^2 = \sigma_{\text{Heis}}^2 = 1/2$. If we start from the same initial qubit Bloch vector $(x_i, y_i, z_i) = (0, 1, 0)$, and assume our measurement adds no additional non-Heisenberg noise, we calculate the final qubit Bloch vector to be

$$\begin{aligned} x_f(I_m, Q_m) &= \text{sech}\left(\frac{I_m \bar{I}_m}{\sigma_I^2}\right) \sin\left(\frac{Q_m \bar{I}_m}{\sigma_I^2}\right) \\ y_f(I_m, Q_m) &= \text{sech}\left(\frac{I_m \bar{I}_m}{\sigma_I^2}\right) \cos\left(\frac{Q_m \bar{I}_m}{\sigma_I^2}\right) \\ z_f(I_m) &= \tanh\left(\frac{I_m \bar{I}_m}{\sigma_I^2}\right) \end{aligned} \quad (4.20)$$

This shows all the hallmarks of phase-sensitive amplification along both quadratures simultaneously as expected. For strong measurements, the sech terms in x_f and y_f will go to zero and the tanh in y_f will again to go ± 1 with the sign dependent on the sign of the measurement result I_m . This is exactly what we expect from a textbook strong projective measurement. For weaker measurements, we see a combination of the stochastic Ramsey rotation around lines of latitude given by the sin and cos terms in x_f and y_f , and the stochastic kick toward the poles given from the tanh term in z_f and the sech terms in x_f and y_f . Also as with the phase-sensitive case, the magnitude of the stochastic Ramsey rotation is encoded in Q_m while the magnitude of the stochastic kick toward the poles is encoded in I_m . Here we can also see that despite the extra half-photon of noise added by phase-preserving amplification, the final Bloch vector $x_f^2 + y_f^2 + z_f^2 = 1$ meaning the qubit

remains in a pure state.

Calculating the effects of non-Heisenberg noise on the final state of the qubit yields

$$\begin{aligned}
 x_f(I_m, Q_m) &= \operatorname{sech}\left(\frac{I_m \bar{I}_m}{\sigma_I^2}\right) \sin\left(\frac{Q_m \bar{I}_m}{\sigma_I^2} + \frac{\bar{Q}_m \bar{I}_m}{\sigma_I^2} \left(\frac{1-\eta}{\eta}\right)\right) e^{-\frac{\bar{I}_m^2}{\sigma_I^2} \left(\frac{1-\eta}{\eta}\right)} \\
 y_f(I_m, Q_m) &= \operatorname{sech}\left(\frac{I_m \bar{I}_m}{\sigma_I^2}\right) \cos\left(\frac{Q_m \bar{I}_m}{\sigma_I^2} + \frac{\bar{Q}_m \bar{I}_m}{\sigma_I^2} \left(\frac{1-\eta}{\eta}\right)\right) e^{-\frac{\bar{I}_m^2}{\sigma_I^2} \left(\frac{1-\eta}{\eta}\right)} \\
 z_f(I_m) &= \tanh\left(\frac{I_m \bar{I}_m}{\sigma_I^2}\right)
 \end{aligned} \tag{4.21}$$

The effects of imperfect measurement are also very analogous to the phase-sensitive case. The measurement becomes less strongly projective, the magnitude of the stochastic Ramsey fringes decreases, and the final state may no longer be pure.

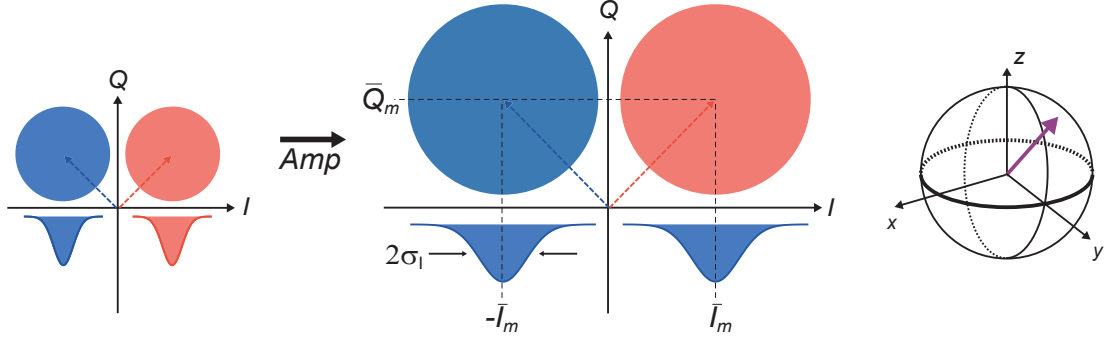


Figure 4.2: Heisenberg back-action of phase-preserving amplification. Fresnel lollipop representation of the coherent state before and after phase-preserving amplification. The back-action resulting on the qubit from this unitary applied to the coherent state is in general the combination of a stochastic kick along lines of longitude and lines of latitude, with the magnitude of the kick encoded in I_m and Q_m respectively.

4.4 Measurement of the Heisenberg Back-Action

4.4.1 Experimental Setup

We choose to perform phase-sensitive amplification with a DP-JBA and phase-preserving amplification with a JPC. The experiment was originally done with the JPC and the data published in [11], and the experiment with the DP-JBA was conducted later. The setup is very similar to the one shown in Fig. 3.9, but with the directional coupler and the JBA switched out for a JPC for the investigation of phase-preserving amplification. The same

DP-JBA and qubit that were used to characterize the non-Heisenberg back-action were used to measure the Heisenberg back-action, and the details of the devices can be found in section 3.5. The JPC used to perform phase-preserving amplification was composed of two $\lambda/2$ transmission line resonators, one at the signal frequency $\omega_a/(2\pi) = 7.4794$ and the other at the idler frequency $\omega_b/(2\pi) = 9.161$, and a JRM with four outer junctions with $I_0 = 2\mu$ critical currents and four inner junctions with $I_0 = 4\mu$ A critical currents. The qubit that was measured by the JPC was also a transmon qubit with frequency $\omega_q/(2\pi) = 5.1038$ GHz and longitudinal decay and Ramsey decay times $T_1 = 60 \mu\text{s}$ and $T_{2R} = 7 \mu\text{s}$, respectively. It is placed in a 3D high purity aluminum cavity with waveguide Purcell filter and resonant frequency $\omega_c^g = 7.4813$ GHz when the qubit is in the ground state, and with input quality factor, $Q_{in}^c = 540000$ resulting in a dispersive shift $(\omega_c^g - \omega_c^e)/(2\pi) = \chi/2\pi = 3.8$ MHz. It is asymmetrically coupled to input and output transmission lines resulting in a decay rate of the readout mode of $\kappa/2\pi = 4.9$ MHz.

The protocol for measuring the Heisenberg back-action is the same regardless of the type of amplification being performed. First the amplifier is biased to have 20 dB of gain, and, in the case of phase-sensitive amplification, the appropriate quadrature is chosen. The pulse sequence for determining the Heisenberg back-action (shown in Fig. 4.3) consists of three steps: state preparation, variable strength measurement, and qubit state tomography. During the first step, we perform a $R_x(\pi/2)$ pulse on the qubit and then read it out with a strong measurement pulse ($\bar{I}_m/\sigma_I = 1.75$), which lets us discriminate between the qubit initially being in the ground or excited state. We post-select based on the results of this measurement, analyzing only the trials where the qubit is found to be in the ground state. During the next step, another $R_x(\pi/2)$ pulse is applied to the qubit preparing it along the $+y$ direction, $(x_i, y_i, z_i) = (0, 1, 0)$. Then, a measurement pulse is applied with strength \bar{I}_m/σ_I varied from 0 to 1.75 by changing the cavity drive amplitude. In the last step, qubit state tomography is performed by applying pre-rotation pulses $(R_y(\pi/2), -R_x(\pi/2), Id)$ followed by a strong measurement to determine the final qubit Bloch vector components (x_f, y_f, z_f) , respectively. The entire protocol is repeated 10^6 times for each measurement strength and choice of amplified quadrature.

In the case of phase-sensitive amplification the relative phase between the cavity drive

and effective pump of the DP-JBA is calibrated via a slight variation of the pulse sequence that is used for investigating the back-action (Fig. 4.4 A.). The qubit is still prepared via post selection, but the strength of the middle measurement is fixed at $\bar{I}_m/\sigma_I = 1.5$ and the relative phase between the effective pump of the DP-JBA and the cavity drive, ϕ_{rel} is varied over more than 200 degrees. The distance between the centers of the ground state and excited state distributions in the resulting histograms are extracted and plotted against the relative phase angle (Fig. 4.4 B). The phase corresponding to the maximal distance between the centers ($\phi_{rel} = 7.0^\circ$) is used for amplification along the I quadrature and the phase where the distance between the centers goes to zero ($\phi_{rel} = 100.5^\circ$) is used for amplification along the Q quadrature. Two example measured histograms, one corresponding to amplification along the I quadrature and the other corresponding to amplification along the Q quadrature are show in Fig. 4.4.1.

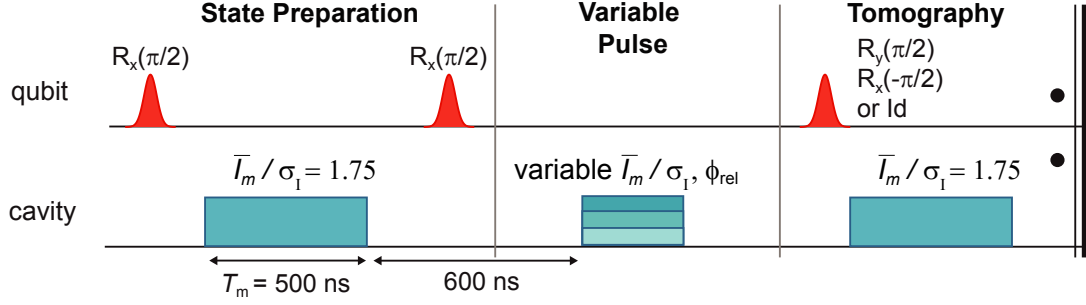


Figure 4.3: Back-action experimental determination: Pulse sequence: First a strong measurement pulse ($\bar{I}_m/\sigma_I = 1.75$) is applied and later used to post-select for trials where the qubit is projected to the ground state. Then a $R_x(\pi/2)$ pulse is used to rotate the qubit to the $+y$ axis. A measurement pulse of variable strength ($\bar{I}_m/\sigma_I = 0$ to $\bar{I}_m/\sigma_I = 1.75$) is applied. We are measuring the back-action of this measurement pulse so the type of amplification, here represented by ϕ_{rel} is explicitly included in the pulse description. Finally tomography is performed.

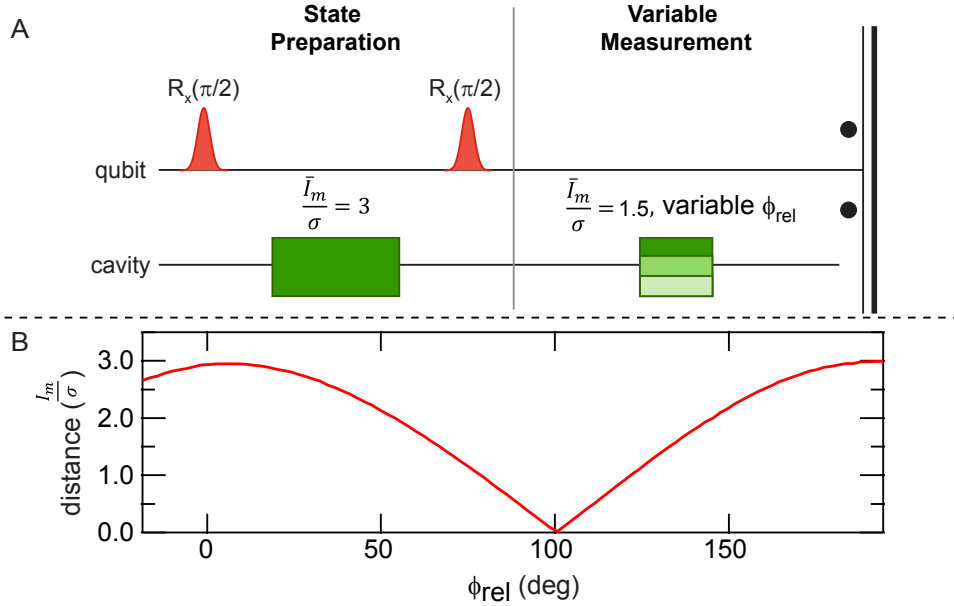


Figure 4.4: Phase calibration for the phase-sensitive amplification. A) Pulse sequence for the measurement. The qubit is prepared along the $+y$ axis and then measured with a strong cavity pulse. B) Measured separation between the center of the ground and excited state qubit histograms as a function of relative phase angle between the cavity drive generator and the effective JBA pump. The relative phase is swept over 200 degrees, leading to a different amount of separation in the resulting qubit histograms (B). The angle of maximum separation corresponds to amplification along the I -quadrature while the angle of minimum separation corresponds to amplification along the Q -quadrature.

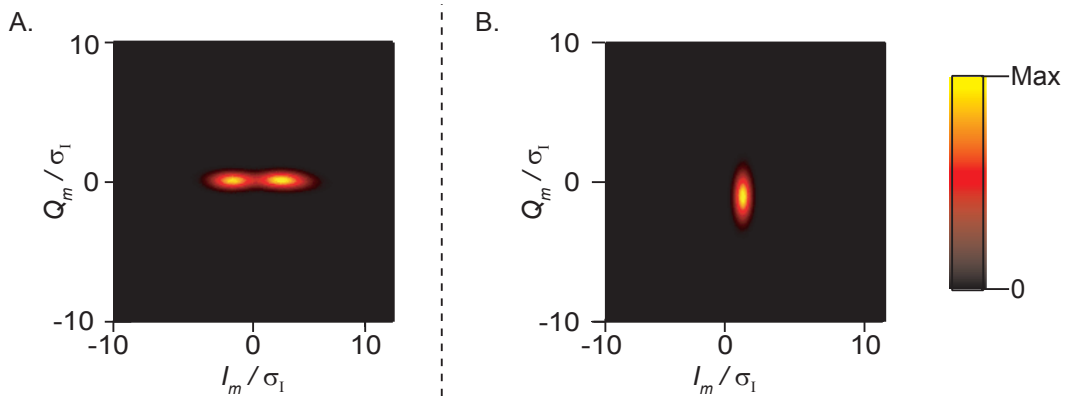


Figure 4.5: Measured histograms of a qubit prepared along the $+y$ axis and then measured with a double-pumped JBA amplifying along the I axis (A), and along the Q axis (B).

4.4.2 Results of Measurement of Phase-Sensitive Back-Action

Fig. 4.6 demonstrates the results of phase-sensitive amplification of the I -quadrature for three different measurement strengths. The left panels show a histogram of the outcomes, while the right three panels show the conditional tomograms of the final qubit Bloch vector $(\langle X \rangle_c, \langle Y \rangle_c, \langle Z \rangle_c)$ which are obtained by plotting the averaged tomography result versus measurement outcome for each (I_m, Q_m) of the 201x201 bins in the histogram. The I -quadrature of the input coherent states is entangled with the z -projection of the qubit, the back-action corresponds to motion along a line of longitude on the Bloch sphere with the amplitude of the back-action encoded in the I -component of the measurement outcome. This is consistent with the conditional tomograms showing progression away from the initial state $(0, 1, 0)$ toward $(0, 0, 1)$ or $(0, 0, -1)$, and is exactly what is expected from Eqn. 4.12. $\langle X \rangle_c$ remains close to 0 for all measurement strengths, which is consistent with the evolution occurring in the y - z plane. In the limit of large \bar{I}_m/σ_I , the operation is a projective measurement along the z -axis.

In contrast, Fig. 4.7 demonstrates the results of phase-sensitive amplification of the Q -quadrature. The input state to the DP-JBA is unchanged, but the I -component is de-amplified resulting in a single peak in the distribution of outcomes. The Q -quadrature encodes back-action orthogonal to the qubit z -axis, and that we should expect the back-action (encoded in the Q_m -component of the outcome) to correspond to evolution along lines of latitude on the Bloch sphere. As expected from Eqn. 4.17, for no measurement the qubit remains in the initial state $(0, 1, 0)$, and as the measurement strength increases we see fringes in $\langle X \rangle_c$ and $\langle Y \rangle_c$. For high measurement strengths, ($\bar{I}_m/\sigma_I = 1.75$), the exponential suppression of the fringe amplitude due to finite measurement efficiency causes all three conditional tomograms to appear white.

As the back-action never results in projection toward the poles, and hence never purifies the qubit state, this operation does not result in a measurement of the qubit despite the fact that a pulse has been entangled with a qubit state, left the cavity, been amplified and recorded. Contrasting the results in Fig. 4.6 illustrates that the choice of amplification mode affects not just the classical outcome but also the quantum back-action. Since the

choice of amplified quadrature can, in principle, be made on the fly, the type of operation performed is not determined at the time when the qubit interacts with the cavity, but is rather determined only after the coherent pulse is measured projectively. In this experiment this mostly takes place after the DP-JBA, and demonstrates a wonderful fact. Because the entangled qubit-pulse state is a fully quantum resource, the action of phase-sensitive amplification on the flying half of this heterogeneous Bell pair can be used to produce novel evolution on the standing half, of which measurement of the qubit along the z-axis is only one possibility.

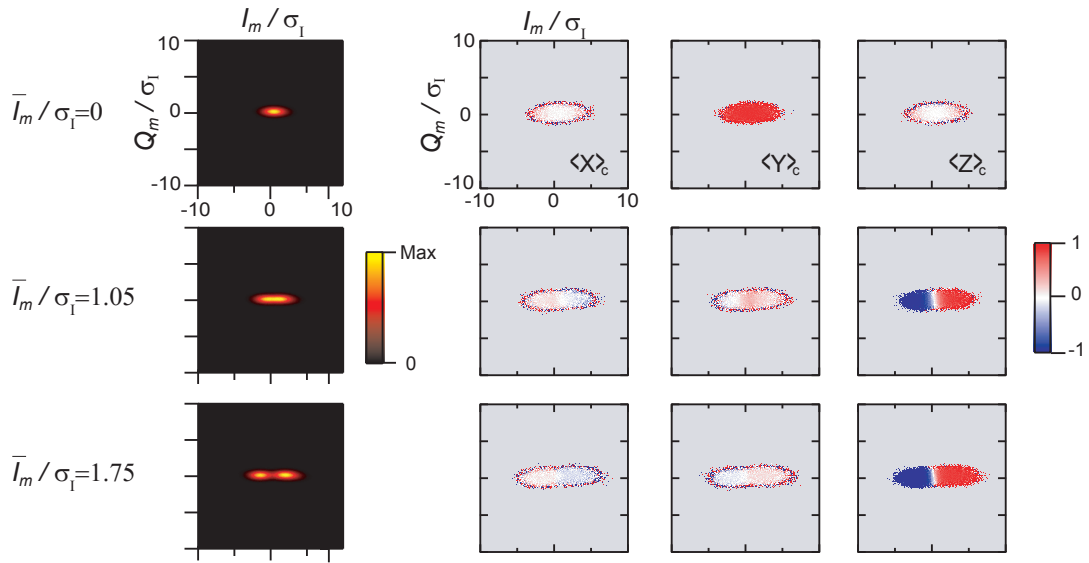


Figure 4.6: Experimental outcomes for amplification along the I quadrature. The left column shows (I_m, Q_m) histograms, with the color plotted on a log scale for visibility, for three different measurement strengths (\bar{I}_m/σ_I) . The right three columns are tomograms showing, for the same measurement strengths, conditional maps of $\langle X \rangle_c$, $\langle Y \rangle_c$, $\langle Z \rangle_c$ versus (I_m, Q_m) . The static value of the $\langle X \rangle_c$ measurement tomograms, as well as the decay in the $\langle Y \rangle_c$ tomograms and the color gradient that develops in the $\langle Z \rangle_c$ tomograms is consistent with qubit evolution along lines of longitude.

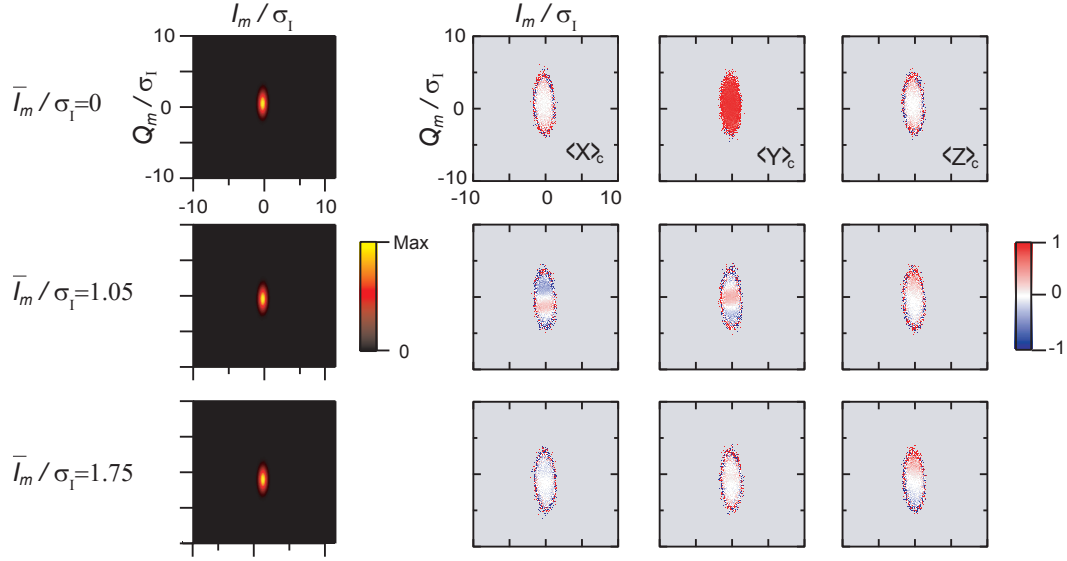


Figure 4.7: Experimental outcomes for amplification along the Q quadrature. The stochastic Ramsey fringes in the $\langle X \rangle_c$ and $\langle Y \rangle_c$ tomograms, along with no evidence of projection in the $\langle Z \rangle_c$ tomograms for even the highest measurement strengths, indicate an operation is being performed that is fundamentally not a measurement. These results are consistent with the qubit evolving along lines of latitude. Due to finite measurement efficiency, the contrast of the fringes is reduced, leading to the lack of visible fringes at $\bar{I}_m/\sigma_I = 1.75$.

4.4.3 Results of Measurement of Phase-Preserving Back-Action

Fig. 4.8 shows the results for phase-preserving amplification with the JPC. Since phase-preserving amplification gives information about both quadratures, we see both types of back-action. As expected from Eqn. 4.20, motion along longitudes of the Bloch sphere is still encoded in the I_m value and motion along the equator is still encoded in Q_m , but the rate of diffusion is slower compared the phase-sensitive amplification where only one process is happening at a time. For zero strength measurement the qubit once again starts pointing along the $+y$ direction, but as the measurement strength is increased we see the histograms separate and simultaneously see fringes develop in $\langle X \rangle_c$ and $\langle Y \rangle_c$ whose angle is dependent on the measurement result Q_m along with differentiation in $\langle Z \rangle_c$ depending on the measurement result I_m . Again, all results are possible but their relative probability is given by the measurement strength. For high measurement strengths the measurement becomes a standard projective measurement.

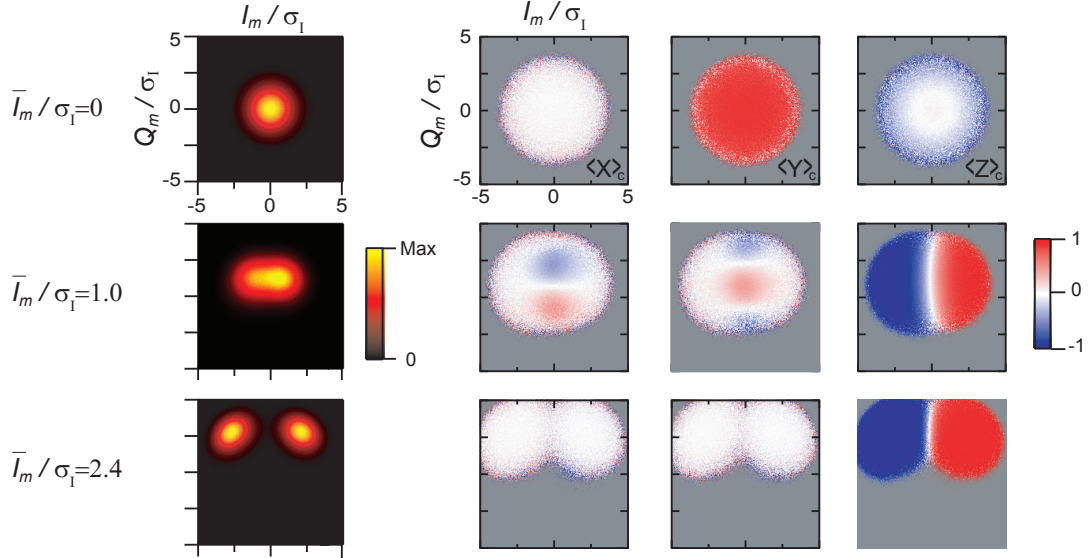


Figure 4.8: A. Experimental outcomes for phase-preserving amplification. The right three columns are tomograms showing, for the same measurement strengths, conditional maps of $\langle X \rangle_c$, $\langle Y \rangle_c$, $\langle Z \rangle_c$ versus (I_m, Q_m) . Because phase-preserving amplification treats equally both quadratures of the coherent pulse, the back-action is a simultaneous finite-strength measurement (encoded in I_m) and stochastic Ramsey evolution (encoded in Q_m). As shown in the last set of tomograms, as the measurement strength increases, we get closer to an ideal projective measurement.

One can extend these ideas to investigate what happens to the state of a quantum system during a measurement pulse. The Siddiqi group has performed a similar measurement [19] where instead of making a phase-sensitive measurement with one long pulse and obtaining a single result (I_m, Q_m) as described above, they treat their measurement pulse as a string of much shorter measurements, each of which provided a result (I_m, Q_m) from which they could calculate the state of their system. This let them reconstruct the trajectory along the Bloch sphere that their quantum system had taken during the measurement. The Huard group has made similar measurements of quantum trajectories of a quantum system undergoing phase-preserving amplification [24]. These types of measurements allow for much greater control of quantum systems, both because they hint at ways to use measurement to steer quantum systems around the Bloch sphere, and because decoherence is lessened due to the continuous monitoring of the fluctuations of the environment.

4.5 Characterizing Measurement Efficiency by the Measurement of Heisenberg Back-Action

As seen in Eqns. 4.21 and 4.17, the amplitude of the stochastic Ramsey oscillations is exponentially suppressed for $\eta < 1$. Thus, the ability to see such oscillations in an experiment is a direct indication of an efficient measurement chain. The fringes shown in Fig. 4.9 were extracted from the $\langle X \rangle_c$ and $\langle Y \rangle_c$ tomograms for $\bar{I}_m/\sigma_I = 1$ for phase-preserving and $\bar{I}_m/\sigma_I = 1.05$ for phase-sensitive amplification along the Q quadrature. We collapse the results down to a single fringe amplitude for each value of Q_m by $\langle X \rangle_c = \sum_{I_m} P(I_m, Q_m)(x)_f$ and $\langle Y \rangle_c = \sum_{I_m} P(I_m, Q_m)(y)_f$ where $P(I_m, Q_m)$ is the probability of measuring that particular result as extracted from the measured histogram. For phase-sensitive amplification along the Q quadrature, all values of I_m are summed over. For phase-preserving amplification, only outcomes around $I_m = 0$ are used as others are projected towards the poles, reducing the fringe contrast. By fitting the amplitude of the fringes for both phase-sensitive amplification along the Q quadrature and phase-preserving amplification we can very accurately extract our measurement efficiency, yielding $\eta = 0.32$ for the experimental setup with the DP-JBA and $\eta = 0.54$ for the setup with the JPC (Fig. 4.9). Because this procedure does not require any additional calibration experiments or hardware, it serves as a robust self-calibrated procedure to extract η .

The length of the Bloch vector as a function of measurement strength both serves as an illustrative summary of the measurement process and gives us a separate way to extract η . Fig. 4.10 plots the measured length of the Bloch vector conditioned on the result of the measurement outcome defined by $\langle R \rangle_c = \sqrt{\langle X \rangle_c^2 + \langle Y \rangle_c^2 + \langle Z \rangle_c^2}$, the length of the unconditional Bloch vector (i.e. averaged over the result of the measurement) defined by $\langle R \rangle = \sqrt{\langle X \rangle^2 + \langle Y \rangle^2 + \langle Z \rangle^2}$, and the conditional length of the z-Bloch vector $\langle |Z_c| \rangle$. In an ideal measurement, $\langle R \rangle_c$ would start at 1 and stay at one for all measurement strengths and for all amplification processes. What we see instead is that $\langle R \rangle_c$ starts at slightly below 1 due primarily to the effects of finite T_1 and T_{2R} and finite readout fidelity, and then begins to dip for both amplification processes. This is due to a direct loss of information linked to reduced measurement efficiency. Then in the case of phase-preserving and phase-

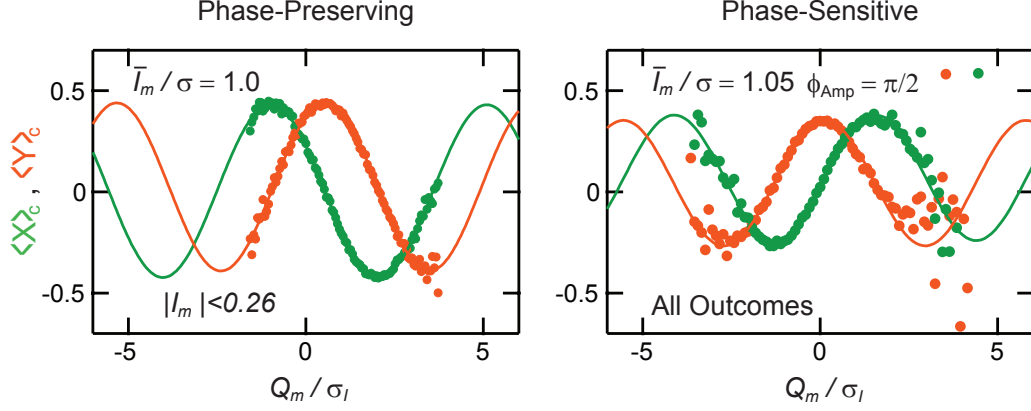


Figure 4.9: Qubit state x and y Bloch vector components for $I_m/\sigma_I = 1.0(1.05)$ versus Q_m/σ_I for phase-preserving amplification (left) and phase-sensitive amplification along $\phi_{\text{Amp}} = \pi/2$ (right). For phase-preserving amplification, only outcomes around $I_m = 0$ are included as others are projected towards the poles, reducing the fringe contrast. The data (filled circles in green and orange for $\langle X \rangle_c$ and $\langle Y \rangle_c$, respectively) are fit to an unconstrained sine wave (fit lines shown as solid lines). From the amplitude of the fringes, we extract the measurement efficiencies of $\eta = 0.54(0.32)$ for phase-preserving (sensitive) amplification.

sensitive amplification along the I axis, we see $\langle R \rangle_c$ start to recover due to the projective nature of the measurement. This can be seen from the fact that in these two cases for high measurement strengths $\langle R \rangle_c$ tracks with $\langle |Z_c| \rangle$, and from the fact that in the case of phase-sensitive amplification along the Q axis, which is not projective for any measurement strength, $\langle R \rangle_c$ continues to fall. Superimposed for all $\langle R \rangle_c$ lines are the calculated values of the conditional purity expected from theory. The unconditioned Bloch vector lengths can be thought of as representing measurement induced dephasing which would occur if the final measurement result (I_m, Q_m) were not known. Fitting to $Ae^{-(\bar{I}_m/\sigma_I)^{21}/\eta}$ also can be used to extract η , giving $\eta = 0.33$ for the DP-JBA and $\eta = 0.54$ for the JPC, in good agreement with the Ramsey fringe data.

This method of determining η has certain advantages to other commonly used alternatives. For example, one such method replaces the cavity with a calibrated noise source to determine the noise temperature of the measurement chain from which the efficiency of the detector can be calculated. However, this calibration must be performed on a separate occasion or with a switch between the two whose impedances are identical and losses are well known. In either case there is potential for differences in losses between the calibration and the experiment leading to an unfaithful extraction of η . Another method consists of mea-

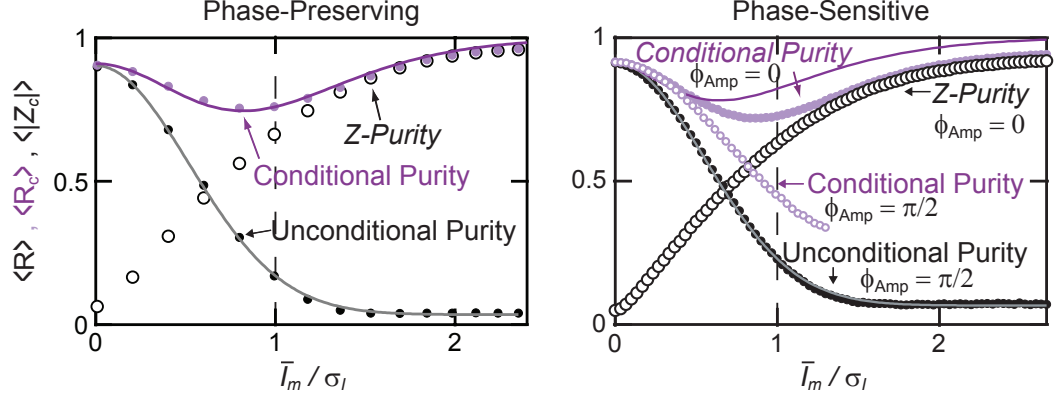


Figure 4.10: Summary of the measurement process for phase-preserving (left) and phase-sensitive (right) amplification. First, consider the purity of the final state vs. pulse strength (closed black circles) when the outcome of the middle measurement is ignored, which we term the unconditional purity ($\langle R \rangle$). This serves as a calibration of the total information content in the coherent pulse. Fits to theory, from which we extract a separate estimate of $\eta = 0.54(0.33)$ are shown as gray curves. For phase-sensitive amplification the total information lost does not depend on the choice of amplified quadrature, for clarity only $\phi_{Amp} = \pi/2$ is shown. Next, we calculate the average of the absolute value of $\langle Z \rangle_c$ when the operation outcome when is used to condition our estimate of the final qubit state (data as open black circles), which we term the Z-purity ($\langle |Z| \rangle_c$). This represents the average effective projectiveness of the measurement for a given coherent pulse amplitude, and as such is only plotted for phase-sensitive amplification ($\phi_{Amp} = 0$). Finally, we calculate the weighted average of the full Bloch vector length (lavender circles), termed the conditional purity ($\langle R \rangle_c$). This demonstrates the competition between measurement-induced dephasing due to lost information in our finite-efficiency quantum operations and purification due to projection towards $z = \pm 1$. Theory curves for the measurement operations are shown as purple lines, using $\eta = 0.54(0.33)$ and matching the non-unity initial length which we attribute to decay during the operation and finite readout fidelity.

asuring the ratio of the separation between the ground and excited state histograms to their standard deviations ($2\bar{I}_m/\sigma_I$) and calculating η from $\bar{I}_m/\sigma_I = \sqrt{2\bar{n}\eta\kappa}T_m \sin(\theta/2)$ where T_m is the length of the recorded measurement pulse and $\theta = 2 \arctan(\chi/\kappa)$. This method is vulnerable to errors in the required separate calibrations of the system bandwidth, cavity drive in photon units, and measurement duration and pulse shape. Our present method avoids both the need for additional hardware and separate calibration experiments, and is therefore more robust. This protocol will be valuable in tracking down the remaining sources of inefficiencies in our experimental protocols.

The ability to achieve an efficiency greater than 50 % in the case of phase-preserving amplification provides direct confirmation of the essential quantum nature of efficient am-

plification. The data cannot be explained by the idler contributing uncorrelated classical fluctuations to the amplifier output, instead the signal and idler are squeezed into a two-mode state. Another experiment [89] has shown evidence of such correlations in a pair of back-to-back amplifiers. The data shown here extend that result by using an external qubit as a quantum witness to the action of the JPC. While phase-sensitive amplification did not achieve this goal in this experiment, largely due to the greater difficulty in extremely stable bias of the amplifier, we are confident that with improved performance of next generation amplifiers [90] they will also achieve extremely high quantum efficiencies. More recent experiments using phase-sensitive amplification with a DP-JBA are approaching this 50 % threshold [19].

Chapter 5

Josephson Circulator

Measurement efficiencies from 0.40 to 0.67 are among the highest reported values for dispersive qubit readout schemes based on a variety of different parametric amplifiers [11, 19–22]. One of the largest contributions to the reduction of measurement efficiency are losses between the cavity and the parametric amplifier. Experiments typically include about 1.5 dB of loss between the cavity and the parametric amplifier [19, 22], which directly limits the measurement efficiency to $\eta \sim 0.7$. This chapter will focus on the microwave circulator, which is the main source of the loss between the cavity and the amplifier, and will present an alternative based upon a new method of pumping the JPC [58] to achieve better efficiency.

5.1 Microwave Circulators

Microwave circulators are the main non-reciprocal element in superconducting qubit experiments. They are essential both for minimizing the back-action from excess photons in the cavity arising from higher temperature stages or reflected tones off parametric amplifiers, and for allowing the routing of signals in more complicated experimental protocols (as an example see [23]). They are three port devices, which pass signals from port 1 to port 2 to port 3 while blocking anything traveling in the reverse direction [91]. This behavior is

encapsulated by the scattering matrix for the ideal circulator

$$s = \begin{bmatrix} 0 & 0 & 1 \\ 1 & 0 & 0 \\ 0 & 1 & 0 \end{bmatrix} \quad (5.1)$$

Commercial microwave circulators are based on the Faraday effect, i.e. the non-reciprocal interaction between magnetic fields and light. They typically provide around 18 dB of reverse isolation over a 4 GHz bandwidth, and around 0.4 dB of insertion loss [92]. In practice, the effective insertion loss of the devices is much higher since the strong magnetic field of the circulator mandates that it be physically separated from the qubit and cavity, and this in turn means that additional cables and connectors, all with their own losses, must be included.

We would like a microwave circulator that is loss-less, noiseless, and completely compatible with superconducting qubit fabrication and operation. This last requirement would allow for the ‘on-chip’ integration of qubits, cavities, and circulators which would minimize the loss from the connecting elements. Moreover it also points toward a device based upon a completely different source of non-reciprocity. It should also be minimal in terms of implementation and hardware, meaning it should be a strictly three-port device.

5.2 Non-Reciprocity with the JPC

To create a more efficient microwave circulator we must first identify a source of non-reciprocity that is not based on strong magnetic fields. We have already met another source of non-reciprocity which is highly compatible with superconducting qubits, the non-reciprocal phase shift that arises in parametric processes. For example, if we examine at the scattering matrix for the single non-degenerate three-wave mixing gain process

$$\begin{bmatrix} a_{out}[\omega_1] \\ b_{out}^\dagger[-\omega_2] \end{bmatrix} = \begin{bmatrix} \sqrt{G} & \sqrt{G_T}e^{-i\phi_p} \\ \sqrt{G_T}e^{i\phi_p} & \sqrt{G} \end{bmatrix} \begin{bmatrix} a_{in}[\omega_1] \\ b_{in}^\dagger[-\omega_2] \end{bmatrix} \quad (5.2)$$

or the conversion process

$$\begin{bmatrix} a_{out}[\omega_1] \\ b_{out}[\omega_2] \end{bmatrix} = \begin{bmatrix} \sqrt{1-C} & \sqrt{C}e^{-i\phi_p} \\ \sqrt{C}e^{i\phi_p} & \sqrt{1-C} \end{bmatrix} \begin{bmatrix} a_{in}[\omega_1] \\ b_{in}[\omega_2] \end{bmatrix} \quad (5.3)$$

then we find that both the trans-gain and the trans-conversion exhibit a non-reciprocal phase shift which depends on the phase of the pump. Regrettably this feature alone is not enough. The scattering matrices are symmetric in magnitude, meaning that several parametric processes need to be interfered in order to generate interactions that are non-reciprocal in magnitude.

One way to achieve this is to create a device with two symmetric interfering paths, and then insert the non-reciprocal parametric device into one of the paths [93]. For example, if two JPCs are physically coupled together at the resonators with resonant frequency \mathbf{b} , and a conversion processes is implemented on each between modes \mathbf{a} and \mathbf{b} , then the resulting device is a frequency preserving block that implements a non-reciprocal phase shift whose value depends on the phases of the two applied pumps [94] (see Fig. 5.1). This type of device is known as a gyrator. If the gyrator is then placed between two microwave hybrids, four-port devices which equally split an incoming signal in power but may impart an unequal phase shift [91], one can build a four-port microwave circulator. For example, in Fig. 5.1 B there are two paths that signals can take from port 1 to port 2, and each path imparts a $\pi/2$ phase shift. Thus, the net effect is signal transmission from port 1 to port 2. There are also two paths signals can take from port 2 back to port 1, but one of these paths has a $\pi/2$ phase shift and the other has a $3\pi/2$ phase shift leading to destructive interference and thus no transmission from port 2 to port 1. This was the first approach taken at Yale to realize a non-Faraday circulator. Although this configuration does result in directionality, it relies on interference spread over multiple microwave elements, meaning that it achieves directionality at the expense of minimality. The device not only involves four separate elements, but also has an extra port. Additionally, optimal device performance relies upon the ability to fabricate and match two JPCs and two different types of on-chip microwave hybrids which was challenging in practice.

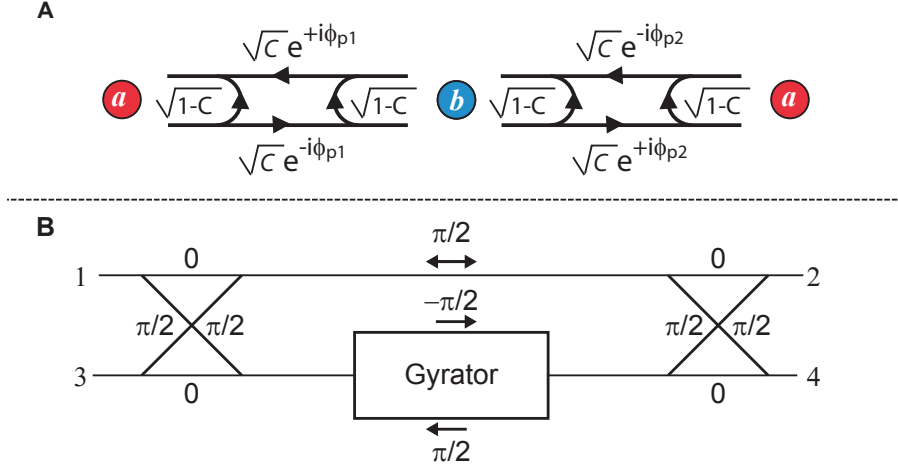


Figure 5.1: Schematic of a microwave gyrator and four-port circulator. A) A gyrator would be composed of two physical JPCs coupled at the port for mode **b**. Both JPCs are pumped to couple modes **a** and **b** via a conversion process, which we supposed to be $C = 1$. This results in a matched frequency preserving block which gives a non-reciprocal phase shift given by $\phi_{p2} - \phi_{p1} + \pi$. The desired phase shift is acquired for $\phi_{p2} - \phi_{p1} = \pm\pi/2$. B) The four port circulator consists of a gyrator, with a 90 deg hybrid on both sides. A 90 deg hybrid takes signals incident on one port, say 1, and produces two outputs which have equal magnitudes but different phase shifts represented by the different labels on the different arms of the device. This configuration sets up two interfering paths such that signals are transferred from port 1 to port 2, from port 2 to port 3, from port 3 to port 4, and from port 4 to port 1 with signals blocked from transferring in the opposite direction.

It is also possible achieve directionality via interfering multiple parametric processes within a single parametric device [57, 95, 96]. We were particularly inspired by the work in [57], which theoretically treats coupled parametric processes in three mode three port a system which is very similar to the JPC. Although traditionally the JPC has coupled modes **a** and **b** via off-resonant pumping of mode **c**, any pair of modes can be coupled via either type of parametric process. In fact, as shown in Fig. 5.2, the three modes of the JPC can be connected with up to six simultaneous gain and conversion processes. As an additional complication, gain and conversion processes do not treat off-resonant signals in the same way. This can be seen directly from the scattering matrices, since gain processes translate between positive and negative frequencies while conversion processes translate between two positive frequencies. If two modes are connected via a gain process, and an incident signal is slightly positively detuned from resonance, then the resulting trans-gain will be slightly negatively detuned from that mode frequency. This can also be

directly seen from conservation of energy. If we have an incident slightly off-resonant tone at frequency $\omega_s + \delta_\omega$, then the frequency of the created idler tone is given by $\omega_p - (\omega_s + \delta_\omega) = \omega_s + \omega_i - (\omega_s + \delta_\omega) = \omega_i - \delta_\omega$. In contrast, if two modes are connected via parametric conversion processes both incident signal and created idler tones will maintain the same sense of detuning. This can be seen either from the fact that the scattering matrix directly connects positive frequency components or from conservation of energy. The frequency of the converted tone will be $(\omega_s + \delta_\omega) - \omega_p = (\omega_s + \delta_\omega) - (\omega_s - \omega_i) = \omega_i + \delta_\omega$. Since the goal is to build devices which achieve non-reciprocity via interference between multiple simultaneous parametric processes, it is perhaps easier to start by picking combinations of processes which return off-resonant tones to the same starting frequency (see Fig. 5.2). We will also start by restricting ourselves to coupling each pair of modes via only one type of parametric process at a time. These restrictions yield two different sets of mode couplings, one which connects all three pairs of modes via conversion processes which will be analyzed in this chapter, and another which connects two pairs of mode via gain processes and the third via a conversion processes which will be analyzed in the next chapter.

We next need a way to analyze the response of the JPC to multiple simultaneous couplings. This requires simultaneously solving multiple coupled Langevin equations. We do this following the method introduced in Ranzani et al in [57] which demonstrates that solving this set of coupled equations is equivalent to simply calculating $i\frac{1}{\gamma_M}KM^{-1}K - 1$ where $\gamma_M = (\kappa_a\kappa_b\kappa_c)^{\frac{1}{3}}$, K is the environmental coupling matrix defined by

$$K = \begin{bmatrix} \sqrt{\kappa_a} & 0 & 0 \\ 0 & \sqrt{\kappa_b} & 0 \\ 0 & 0 & \sqrt{\kappa_c} \end{bmatrix} \quad (5.4)$$

and M is the mode coupling matrix, which for three simultaneous conversion processes is given by

$$M = \begin{bmatrix} \delta_{aa} & \beta_{ab} & \beta_{ac} \\ \beta_{ab}^\dagger & \delta_{bb} & \beta_{bc} \\ \beta_{ac}^\dagger & \beta_{bc}^\dagger & \delta_{cc} \end{bmatrix} \quad (5.5)$$

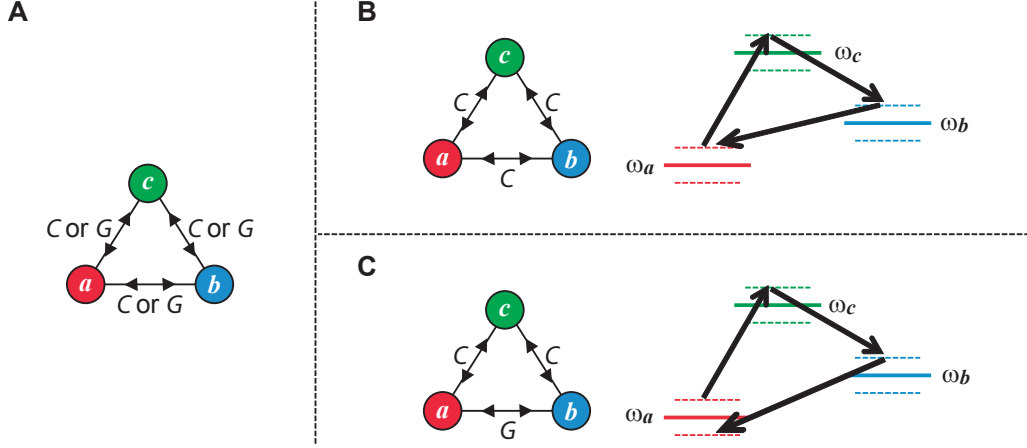


Figure 5.2: Schematic of mode coupling options in the JPC. A) Each pair of modes in the JPC can be connected by either a parametric gain or a parametric conversion process. Both of these processes couple signals on resonance, but they do not treat off resonant signals in the same way. Parametric gain processes take tones that are negatively detuned from resonance to frequencies that are positively detuned. In contrast, parametric conversion processes preserve the sign of the detuning. Therefore, when interfering groups of parametric processes there are combinations, such as shown in (B), with three pairs of conversion processes, which start and stop at the same frequency. In this case the process is phase-preserving. There are also combinations of processes, such as shown in (C), with two conversion processes and one gain process, which do not return to the same frequency upon completion of a cycle. These lead to phase-sensitive processes.

$\delta_{ii} = \frac{\kappa_i}{\gamma_M} \left(\frac{\omega - \omega_i}{2\pi\kappa_i} + i \right)$ where ω_i is the resonant frequency of mode i , κ_i is the decay rate of mode i , and $\beta_{ij} = \frac{|g_{ij}|}{2\gamma_M} e^{i\phi_p^{ij}}$ where g_{ij} is the pump dependent coupling between modes i and j . Recall $C = (4|g_{ij}|^2/\kappa_i\kappa_j)/(1 + |g_{ij}|^2/\kappa_i\kappa_j)^2$, where C ranges from 0 (no-conversion) to 1 (full-conversion when $|g_{ij}| = \sqrt{\kappa_i\kappa_j}$). To simplify the notation we let $|g_{ij}| = \mu_{ij}\sqrt{\kappa_i\kappa_j}$ where μ_{ij} runs from 0 to 1 and serves as a stand-in for the more complicated full expression for C . Making this substitution, and looking at the behavior for each mode on resonance, we get diagonal terms of the form:

$$|s_{i,i}|^2 = \frac{(-1 + \mu_{ij}^2 + \mu_{ik}^2 - \mu_{jk}^2)^2 + 4\mu_{ij}^2\mu_{jk}^2\mu_{ik}^2 \cos(\phi_p^{ab} - \phi_p^{ac} + \phi_p^{bc})}{(1 + \mu_{ij}^2 + \mu_{jk}^2 + \mu_{ik}^2)^2 + 4\mu_{ij}^2\mu_{jk}^2\mu_{ik}^2 \cos(\phi_p^{ab} - \phi_p^{ac} + \phi_p^{bc})^2} \quad (5.6)$$

and off-diagonal terms of the form

$$|s_{i,j}|^2 = \frac{4(\mu_{ij}^2 + \mu_{ik}^2\mu_{jk}^2 \pm 2\mu_{ij}\mu_{jk}\mu_{ik} \sin(\phi_p^{ab} - \phi_p^{ac} + \phi_p^{bc}))}{(1 + \mu_{ij}^2 + \mu_{jk}^2 + \mu_{ik}^2)^2 + 4 \cos(\phi_p^{ab} - \phi_p^{ac} + \phi_p^{bc})^2} \quad (5.7)$$

with $-$ is in terms s_{ac} , s_{ba} , and s_{cb} and the $+$ is in terms s_{ca} , s_{ab} , and s_{bc} . There are a

few important things to note about these expressions. Despite the somewhat complicated dependence on pump phase, they only depend on the total pump phase $\phi_{tot}^{circ} = \phi_p^{ab} - \phi_p^{ac} + \phi_p^{bc}$. Notice also that the + terms all correspond to traveling between the modes in one particular direction, from **c** to **a** to **b** and the – terms correspond to traveling between the modes in the opposite direction. This difference in sign for the two different directions in travel is what will result in non-reciprocal circulation in the device. These expressions get even simpler for $\phi_{tot}^{circ} = n\pi/2$ where n is an odd integer. Looking for example at $\phi_{tot}^{circ} = \pi/2$ the scattering matrix reduces to

$$|s| = \begin{bmatrix} -1 + \frac{2(1+\mu_{bc}^2)}{1+\mu_{ab}^2+\mu_{bc}^2+\mu_{ac}^2} & \frac{2(\mu_{ab}+\mu_{bc}\mu_{ac})}{1+\mu_{ab}^2+\mu_{bc}^2+\mu_{ac}^2} & \frac{2(\mu_{ac}-\mu_{ab}\mu_{bc})}{1+\mu_{ab}^2+\mu_{bc}^2+\mu_{ac}^2} \\ \frac{2(\mu_{ab}-\mu_{ac}\mu_{bc})}{1+\mu_{ab}^2+\mu_{bc}^2+\mu_{ac}^2} & -1 + \frac{2(1+\mu_{ac}^2)}{1+\mu_{ab}^2+\mu_{bc}^2+\mu_{ac}^2} & \frac{2(\mu_{bc}+\mu_{ab}\mu_{ac})}{1+\mu_{ab}^2+\mu_{bc}^2+\mu_{ac}^2} \\ \frac{2(\mu_{ac}+\mu_{ab}\mu_{bc})}{1+\mu_{ab}^2+\mu_{bc}^2+\mu_{ac}^2} & \frac{2(\mu_{bc}-\mu_{ab}\mu_{ac})}{1+\mu_{ab}^2+\mu_{bc}^2+\mu_{ac}^2} & -1 + \frac{2(1+\mu_{ab}^2)}{1+\mu_{ab}^2+\mu_{bc}^2+\mu_{ac}^2} \end{bmatrix} \quad (5.8)$$

For all $\mu_{ij} = 1$, which is equivalent to taking all of our conversion coefficients being 1, the scattering matrix further reduces to

$$|s| = \begin{bmatrix} 0 & 1 & 0 \\ 0 & 0 & 1 \\ 1 & 0 & 0 \end{bmatrix} \quad (5.9)$$

which is equivalent to an ideal circulator. Keeping all of our conversion coefficients as 1 and flipping our total pump phase by π to $\phi_{tot}^{circ} = -\pi/2$ we find

$$|s| = \begin{bmatrix} 0 & 0 & 1 \\ 1 & 0 & 0 \\ 0 & 1 & 0 \end{bmatrix} \quad (5.10)$$

which is just a circulator circulating in the other direction.

We can also look at the effect of mismatched conversion coefficients on the performance of the device. For the sake of simplicity we will take two of the μ_{ij} terms to be one, and let one vary continuously from 0 to 1. Returning to Eqn. 5.8, it is easy to see that provided only one μ_{ij} is varied, every element of the scattering matrix is insensitive to which μ_{ij} is chosen.

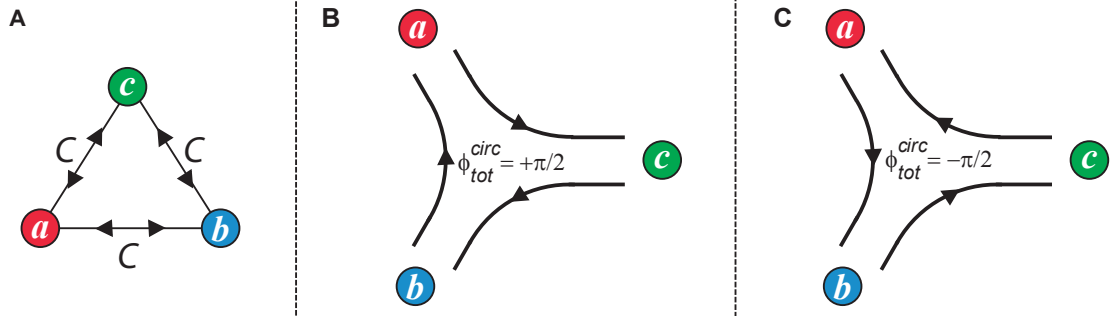


Figure 5.3: Schematic of the Josephson circulator A) Pump configuration for the circulator. All three pairs of modes are connected via conversion processes. B) and C) Graphical scattering matrix for the resulting device. A total pump phase of $\phi_{total}^{circ} = \pi/2$ yields a clockwise circulator while a total phase of $\phi_{total}^{circ} = -\pi/2$ yields a counterclockwise circulator.

Also, if we identify the diagonal elements as representing the input matches of the ports, the off-diagonal terms with a + in the numerator as representing the insertion losses, and the off-diagonal terms with a - in the numerator as representing the reverse isolation then each role responds to single term mismatches in exactly the same way. Fig. 5.4 therefore plots a representative input match, insertion loss, and reverse isolation term as a function of a single mismatched μ_{ij} here taken to be μ_{ab} . Device performance degrades as the mismatch in effective conversion coefficient increases, but the function of each port remains the same.

This proposal is simpler than the original, as it only requires one JPC and does not require the additional microwave hybrids. It also is a three port device like the original circulator proposal.

There have been other Josephson circulator proposals that do not rely upon the Faraday effect. One such proposal [97] uses passive DC electric and magnetic fields to bias a ring of three Josephson Junctions to realize non-reciprocal behavior, but such a system is very susceptible to additional noise from offset charges. Another proposal [96] based around modulating the inductance of several SQUIDS also can yield a four-port microwave circulator.

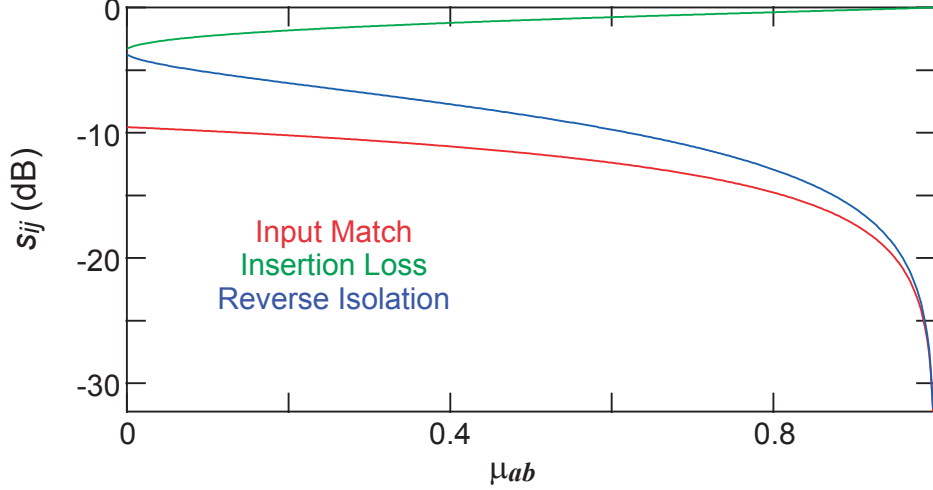


Figure 5.4: Effect of mode mismatch on the Josephson circulator (theory). On resonance response of the input match, insertion loss, and reverse isolation calculated for two conversion coefficients being 1, and the third, here μ_{ab} swept from 0 to 1. Although the performance of the device degrades for mismatches in conversion coefficient, the function of each port remains the same.

5.3 Experimental implementation

The JPC used for this experiment was composed of an eight-junction ring fabricated on $300 \mu\text{m}$ silicon using the conventional Dolan bridge technique [98] defined using electron beam lithography followed by double-angle aluminum deposition. It consists of two perpendicular $300 \mu\text{m}$ wide $\lambda/2$ microstrip resonators of lengths 4.68 mm and 9 mm , each terminated by microstrip gap coupling capacitors (28 fF for mode \mathbf{a} and 32 fF for mode \mathbf{b}). These coupling capacitors resulted in energy decay rates $\kappa_{\mathbf{a}}/2\pi = 44 \text{ MHz}$, $\kappa_{\mathbf{b}}/2\pi = 19 \text{ MHz}$, and $\kappa_{\mathbf{c}}/2\pi = 50 \text{ MHz}$. An external flux was applied by applying a current to a wound superconducting magnet, and set such that the modes had frequencies $\omega_{\mathbf{a}}/2\pi = 9.167 \text{ GHz}$, $\omega_{\mathbf{b}}/2\pi = 5.241 \text{ GHz}$, and $\omega_{\mathbf{c}}/2\pi = 7.174 \text{ GHz}$.

To realize a true microwave circulator, where incident signals are directionally transferred between physical ports of the device, we need a way to couple each of the three modes of the JPC to a different physical port. Recall that the three normal modes of the JPC correspond to a differential excitation of the signal resonator alone, a differential excitation of the idler resonator alone, and a common mode excitation of both resonators. All three modes can be individually addressed if we connect the JPC to a cascade of 180° hybrids as seen in

Fig. 5.5. The delta port of the lower left hybrid will apply a differential drive \mathbf{b} , and the delta port of the lower right hybrid will apply a differential drive to \mathbf{a} . The delta port of the top hybrid will produce a differential drive at the output of the top hybrid. One of those outputs is directed into the sigma port of the the lower left hybrid which will produce a common mode drive on the idler resonator, while the other out of phase output from the top hybrid is directed toward the sigma port on the lower right hybrid creating a common mode drive on the signal resonator which is out of phase with the common drive on the idler. This is exactly the spatial mode pattern of \mathbf{c} as desired.

Now that we have determined our three spatial ports, we need a way to apply pump and probe signals to each mode and a way to separate incoming signals from outgoing signals. Both of these roles are achieved with a directional coupler connected to the delta port of each of the hybrids. Incoming pump and probe tones are generated and combined at room temperature before traveling down a line in our dilution refrigerator and entering the weakly coupled port of the appropriate directional coupler. All pumps were generated by physically separate generators at room temperature, which were all locked to a common 10 MHz rubidium frequency standard. The probe tone was generated via one port of a VNA and directed toward one one mode at a time via a self-terminating microwave switch. Output signals reflected signals off the JPC are directed to the strongly coupled port of the directional coupler and then to an output line of the fridge and then back to the other port of the VNA where they are measured. Since we will be looking at both diagonal and off-diagonal scattering matrix components the input and output signals may not be commensurate. In these cases the output is directed toward and additional mixer which simply translates the output frequency back to that of the input.

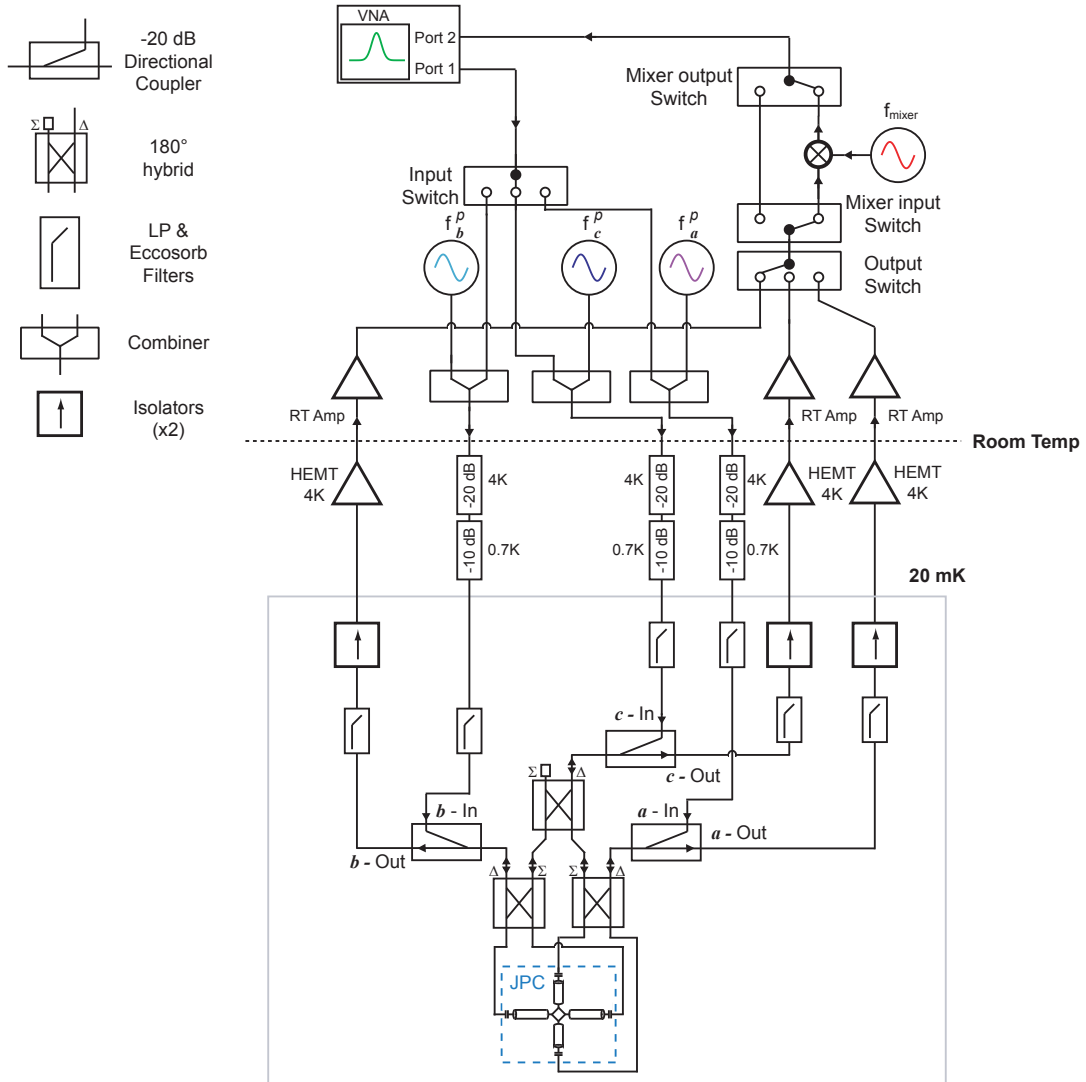


Figure 5.5: Experimental setup for characterizing the Josephson circulator and directional amplifier. The Josephson Parametric Converter (JPC) is connected to a cascade of 180° hybrids, the lower two of which address modes a and b , and the upper which addresses mode c . Each hybrid is connected to a directional coupler which separates input from output. A directional coupler was chosen for this purpose instead of a circulator due its large operating frequency bandwidth (4-20 GHz). At room temperature, pumps are applied to each input port via separate generators locked to the same 10 MHz rubidium atomic clock. The probe tone is sourced from a VNA, and a switch is used to pick which input port is addressed. After the switch, the probe is combined with the appropriate pump tone and travels down the fridge through filters and attenuators to the weakly coupled port of the appropriate directional coupler. The output of each port of the JPC travels out of the fridge through a standard set of filters, isolators, and higher stages of amplification. The choice of which output is measured is controlled by a switch at room temperature. If the VNA probe tone and the measured output tone are at different frequencies, the output is directed to a mixer where the output frequency is mixed back to that of the input. If the input and output tones are at the same frequency, the mixer is bypassed. We note all the switches used are specially chosen to terminate the unconnected ports to 50Ω .

We bias the Josephson circulator by first looking at the individual pairwise conversion processes, and looking for sets of parameters where the conversion coefficients of the various pair-wise modes were both large and well-matched in frequency. Once the circulator was fully biased, the individual pump powers were fine-tuned by finding the values that minimized the input match and the reverse isolation of each port. This resulted in the final experimental pump frequencies and powers (as measured at the output of the individual generators) of $\omega_{ab}^p/2\pi = 3.928$ GHz, $P_{ab}^p = -29.92$ dBm, $\omega_{bc}^p/2\pi = 1.9291$ GHz, $P_{bc}^p = -7.42$ dBm, and $\omega_{ac}^p/2\pi = 1.9989$ GHz, $P_{ac}^p = 1.9$ dBm, corresponding to conversion coefficients C of 0.97, 0.98, and 0.99, respectively. These pairwise conversion processes are shown in Fig. 6.3. The response for signals entering the mode c is smaller than expected. This can be understood by going back to the experimental setup. These signals must go through all three hybrids, as well as all the nominally matched cable pairs at the output of each hybrid. Although care was taken to match the amplitude and phase response at room temperature, some residual mismatches remain. This could be due to the phase lengths of individual components changing as they cool.

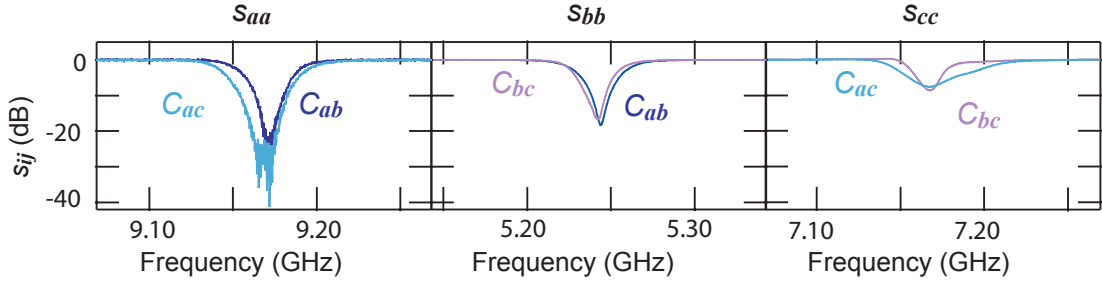


Figure 5.6: The measured pairwise conversion curves for all three processes used in the circulator. The symbol C_{ij} indicates a conversion process linking modes i and j . For each port (a b c), the pump parameters are chosen to match the conversion coefficient and center frequency for both processes involving that mode. We attribute the smaller than expected response of s_{cc} for both pumps to mismatches in the cascaded hybrid structure.

Once all three pumps are simultaneously turned on, the next step is to identify the offset in the total pump phase and find the point where $\phi_{tot}^{circ} = \pm\pi/2$. We tune the total pump phase by tuning the physical phase of the generator addressing mode c , and finding the points where s_{bb} is minimized. Following the convention in the theory section, we assign $\phi_{tot}^{circ} = \pi/2$ to clockwise circulation.

Figure 5.7 shows the complete set of measured scattering parameters (s_{ij} , $i, j = \mathbf{a}, \mathbf{b}, \mathbf{c}$) for the circulator as a function of probe frequency as taken with a vector network analyzer (VNA). The probe power at the VNA output was -55 dBm, corresponding to the power right before saturation effects began to appear. On resonance we have a matched device (with reflection better than -10 dB) exhibiting more than 18.5 dB reverse isolation, and less than 0.5 dB of insertion loss. The insertion loss is calibrated relative to the three individual conversion processes, which have been previously demonstrated to be efficient to within 0.1 dB [35]. Off resonance, the bandwidth of the individual conversion processes which comprise the circulator combine to give an 11 MHz bandwidth over which the input match of all ports is better than -10 dB and the insertion loss is better than 1 dB. Superimposed are the theoretical scattering parameters (from Eqn. 5.8), calculated using the measured single-mode conversion coefficients and the measured mode bandwidths.

Simply flipping the pump phase by π to $\phi_{tot}^{circ} = -\pi/2$, without any other variation of pump parameters, switches the direction of circulation, as shown. We see no degradation in overall device performance compared to $\phi_{tot}^{circ} = \pi/2$. We have good agreement with theoretical calculations for the scattering parameters in both directions, given that theory assumes only three-wave mixing (no higher order terms), and that the calculation uses only the three measured mode bandwidths and the conversion coefficients of the three individual conversion processes. We note that most deviations are associated with signals input to mode \mathbf{c} . We attribute these to the degradation in the spatial mode matching due to phase mismatches in the three cascaded hybrids versus \mathbf{a} and \mathbf{b} which each pass through a single hybrid. The mode matching could easily be improved by substituting in cables or hybrids which have a better amplitude and phase match when cold. This may involve some more iterations of the experiment, but is simple to implement. Other asymmetries seen in the data, particular in the reverse isolation scattering parameters, are attributed to drifts in the total pump phase. Stabilizing the total pump phase through the use of interferometric techniques and the ability to achieve higher single-mode conversion coefficients would yield better device performance. An explicit example of such a setup is given in the next chapter for a similar device.

Returning to the theoretical scattering parameters, although the device only functions

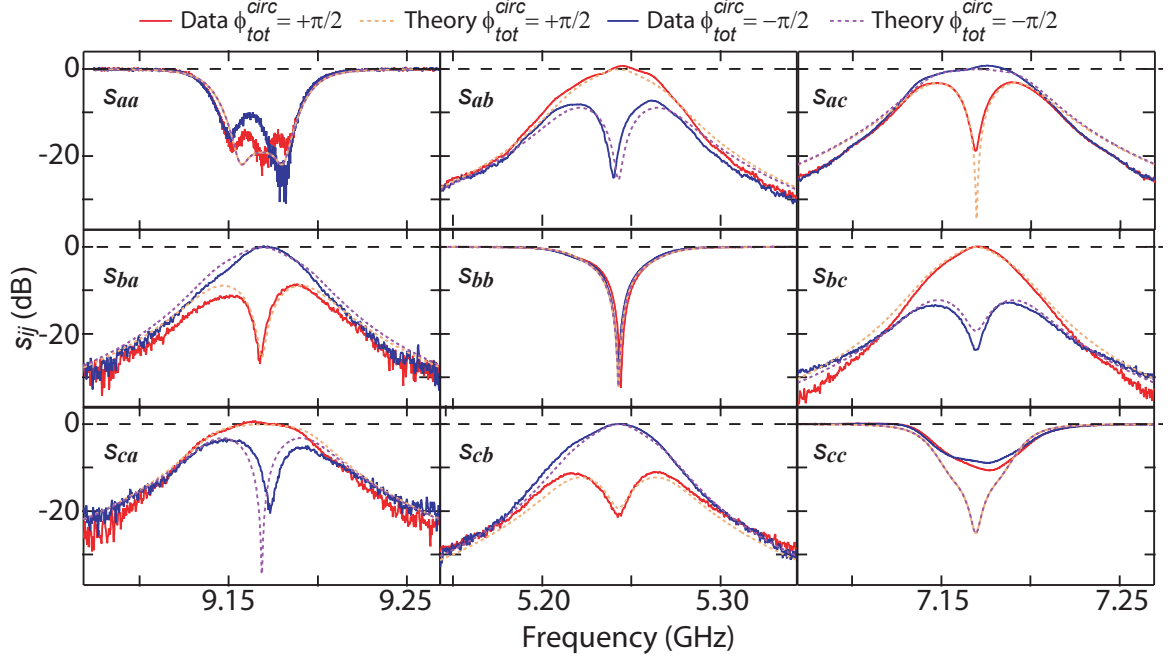


Figure 5.7: Measured scattering parameters for the Josephson circulator. Scattering parameters are plotted versus frequency for the clockwise (red) and counter-clockwise (black) circulator. The device displays 1 dB insertion loss and -10.5 dB isolation over an 11 MHz bandwidth. Theory curves for the clockwise (dashed yellow) and counter-clockwise (dashed violet) circulator are superimposed.

as a circulator at particular values of the total pump phase, it should display a smooth transition between those points. We experimentally verify this by measuring two representative scattering parameters, s_{bb} and s_{cb} , as a continuous function of pump phase (Fig. 5.8) and compare it with theory. The two are in excellent agreement, showing three working points with alternating circulation directions at points separated by π in phase ($-3\pi/2, -\pi/2, \pi/2$), with smooth transitions in the scattering parameters versus frequencies in between. Further experimental and theoretical work are required to predict and characterize the effect of higher order nonlinearities on the fine details of the device performance. This is especially vital for determining how many probe photons the device can process without degradation of performance.

We can also experimentally characterize the effect of mismatched conversion coefficients by looking at a set of representative scattering parameters and intentionally changing only one of the conversion coefficients. Returning to Fig. 6.2, we expect the performance of the device to degrade, but for the function of each port to remain the same. Fig. 5.9 shows

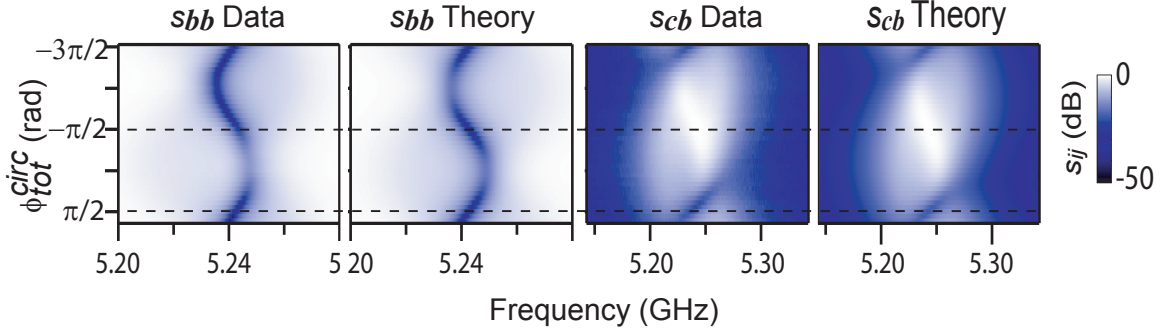


Figure 5.8: Representative scattering parameters (one reflected scattering parameter and one off-diagonal scattering parameter) as a function of phase. Cuts at $\pi/2$ and $-\pi/2$ give the two working points explicitly plotted above, and we see a smooth and symmetric transition between the points. The data and theory are in excellent qualitative agreement.

the measured set of scattering parameters for signals entering mode b when C_{bc} and C_{ac} were held constant, and C_{ac} was set to 0.91, 0.61, and 0.25. Even for the lowest value of C_{ac} , the input still shows an on-resonance match of 9 dB, a reverse isolation 6.5 dB, and an insertion loss of only 1.4 dB. A mismatch in conversion coefficients does degrade device performance, but does not change the function of each port, as expected. This robustness to conversion mismatches means is very advantageous as a practical device.

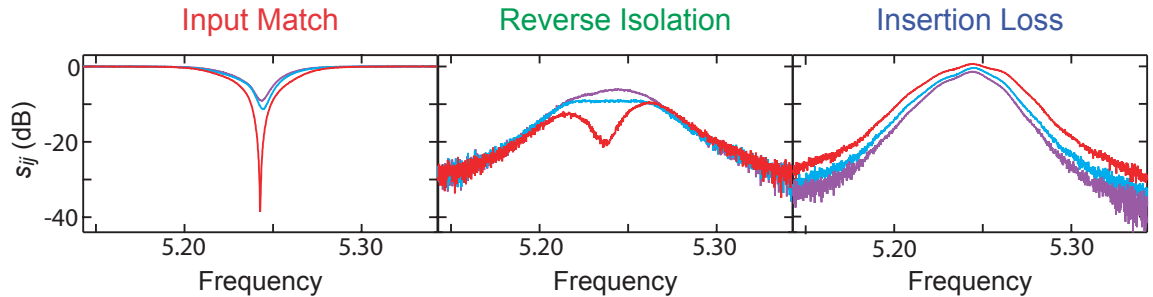


Figure 5.9: Effect of mode mismatch on signals entering mode b . C_{bc} and C_{ac} were held at 0.98 and 0.99 as before, and C_{ab} was taken to be 0.91 (red), 0.61 (blue), and 0.25 (purple). We see that as the conversion coefficients are mismatched the device performance does degrade, but the function of each port remains the same.

Although the measured device parameters are comparable with those of a traditional Faraday-based microwave circulator on resonance, performance could be improved by achieving higher single mode conversion and by improving the impedance match between mode c and the cascaded hybrid structure. Achieving higher conversion coefficients was challenging due to the effect of higher order terms in the JPC. These terms are not currently accounted

for in the theory, but they could be included in the future. It may also be possible to change the parameters of the JRM in order to further minimize the effect of these terms. Another limitation in the performance of the device is drifts in the relative phases of the three independent generators used to source the three pumps. These drifts lead to drifts in the total pump phase, and thus in the bias point for the circulator. This could be improved by more cleverly sourcing the pumps from a shared set of generators in a way that cancels pump drifts similar to what was done with the double-pump JBA. Even with comparable device performance the Josephson circulator could result in higher measurement efficiencies simply because it needs less isolation from the cavity and qubit. To first order, simply moving the two closer removes some cable and connector loss. In order to achieve on-chip integration between the two, the magnetic flux threading the JPC would also need to be provided via an on-chip flux line as opposed to the physically separate coil based superconducting magnet currently used.

Chapter 6

Josephson Directional Amplifier

The last chapter presented a Josephson circulator, a directional device which could replace the lossy commercial microwave circulators which are required in our current measurement architectures. Another approach to eliminating these circulators is to use a directional parametric amplifier. This is a device which performs quantum-limited amplification between an input port and an output port, and does not transmit any amplified signals from the input port back toward the qubit. Further, if this amplifier could be fabricated using the same materials and processes used for superconducting qubits and cavities, and all three could be fabricated on the same chip, we would further increase our measurement efficiency, η , by removing unnecessary cable and connector loss.

6.1 Overview of Low-Noise Directional Parametric Amplifiers

Low-noise directional parametric amplification has been an active area of research in the superconducting qubit community. Microwave SQUID amplifiers such as the microstrip SQUID amplifier (MSA) [59–61] and the superconducting low-inductance undulatory galvanometer microwave amplifier (SLUG) [62, 63] are directional amplifiers based upon DC-biasing a SQUID into the voltage regime such that a small change in flux in the SQUID will result in a large change in the output voltage [60]. One can think about the evolution of the phase across the junction in such a system as an effective pump composed of sev-

eral Josephson harmonics. The interference of the mixing processes generated by different harmonics gives rise to directionality [99]. Microwave SQUID amplifiers can achieve high gains, and have been used to measure superconducting qubits [100, 101], although they are not quite quantum-limited for high gain points at high frequencies [99] and may have out-of-band back-action, which might still require circulators to be included [100].

Another class of directional amplifiers, known as traveling wave parametric amplifiers (TWPAs), achieve directional gain by chaining several parametric gain stages together. These amplifiers are different from traditional Josephson parametric amplifiers because they are not based on resonant structures. This means they can achieve higher bandwidths than traditional paramps, but they can suffer from limited gain unless great care is taken to match the phase of the signal and the pump over the length of the device [67, 68]. TWPAs based on the non-linearity of optical fiber have been widely used in the optical domain [102]. TWPAs based upon the non-linearity thin superconducting wire [65], and chains of Josephson junctions [22, 64, 68] have been realized in the microwave domain, although until recently either phase-matching issues or heating due to large pump tone were limiting. A Josephson junction based TWPA has also been recently used to measure a superconducting qubit [22], although this experiment still included a circulator.

Directional amplification can also be achieved through interfering multiple parametric processes in resonant devices. This interference can take place spatially between different signal paths spread over multiple elements, or between multiple processes coupled within a single device. In a scheme very similar to the four port circulator discussed in the last chapter, a four port directional amplifier can be realized by coupling two JPCs, operated as parametric amplifiers, via microwave hybrids [33, 103]. This was the first approach we took at Yale to realize directional amplification. The corresponding device was used to measure a qubit without any circulators between the cavity and the amplifier [69], but displayed limited gain due to the difficulty of fabricating and biasing identical JPCs and integrating several components together. It also added slightly more noise than the quantum limit. Some of these difficulties can be alleviated if the interference occurs within a single device instead of spread between multiple physical devices. There have been several theoretical proposals for achieving directional gain through coupling multiple types of parametric processes in a

single device [57, 95, 104]. This chapter implements the scheme proposed in [57], resulting in a Josephson directional amplifier (JDA) based on parametrically coupling of all three modes of the JPC [58].

6.2 Derivation of Gain in the JDA

As originally proposed in [57], in a three mode system directional gain can arise from coupling two pairs of modes via gain processes and the third via a conversion process. This is the other set of non-frequency translating mode couplings alluded to in the last chapter. Reproduced here is a more detailed derivation of the gain of such a directional amplifier, which was originally done in [57]. Using the formalism as in the last chapter to compute the scattering matrix, where we now couple modes \mathbf{a} and \mathbf{c} , and \mathbf{b} and \mathbf{c} , by gain processes and modes \mathbf{a} and \mathbf{b} via a conversion process. The coupling matrix for such a configuration is given by

$$M = \begin{bmatrix} \delta_{aa} & \beta_{ab}^\dagger & -\beta_{ac}^\dagger \\ \beta_{ab} & \delta_{bb} & -\beta_{bc}^\dagger \\ \beta_{ac} & \beta_{bc} & -\delta_{cc}^\dagger \end{bmatrix} \quad (6.1)$$

where $\beta_{c,a} = -\beta_{a,c}^\dagger$, $\beta_{c,b} = -\beta_{b,c}^\dagger$, and δ_{cc} is negative and conjugated because parametric amplification processes effectively couple positive and negative frequency components as seen in chapter 2. Recall that for conversion processes $C = (4|g_{i,j}|^2/\kappa_i\kappa_j)/(1+|g_{ij}|^2/\kappa_i\kappa_j)^2$, ranging from 0 (no-conversion) to 1 (full-conversion when $|g_{ij}| = \sqrt{\kappa_i\kappa_j}$). For parametric gain processes $\sqrt{G} = (1+|g_{ij}|^2/\kappa_i\kappa_j)/(1-|g_{ij}|^2/\kappa_i\kappa_j)$, ranging from no amplification ($\sqrt{G} = 1$) for $|g_{ij}|^2 = 0$ and arbitrarily large gain for $|g_{ij}|^2 \rightarrow \kappa_i\kappa_j$. Thus as in the last section we take $|g_{ij}| = \mu_{ij}\sqrt{\kappa_i\kappa_j}$ for both the gain and the conversion coupling coefficients where μ_{ij} goes from 0 to 1. We can then explicitly calculate some representative scattering parameters on resonance and find terms of the form

$$|s_{c,b}|^2 = \frac{4(\mu_{bc}^2 + \mu_{ab}^2\mu_{ac}^2 + \mu_{ab}\mu_{bc}\mu_{ac} \sin(\phi_p^{ab} - \phi_p^{ac} + \phi_p^{bc}))}{(-1 - \mu_{ab}^2 + \mu_{ac}^2 + \mu_{bc}^2)^2 + 4\mu_{ab}^2\mu_{bc}^2\mu_{ac}^2 \cos(\phi_p^{ab} - \phi_p^{ac} + \phi_p^{bc})^2} \quad (6.2)$$

$$|s_{b,c}|^2 = \frac{4(\mu_{bc}^2 + \mu_{ab}^2 \mu_{ac}^2 - \mu_{ab} \mu_{bc} \mu_{ac} \sin(\phi_p^{ab} - \phi_p^{ac} + \phi_p^{bc}))}{(-1 - \mu_{ab}^2 + \mu_{ac}^2 + \mu_{bc}^2)^2 + 4\mu_{ab}^2 \mu_{bc}^2 \mu_{ac}^2 \cos(\phi_p^{ab} - \phi_p^{ac} + \phi_p^{bc})^2} \quad (6.3)$$

$$|s_{b,b}|^2 = \frac{(-1 + \mu_{ab}^2 + \mu_{ac}^2 - \mu_{bc}^2)^2 + 4\mu_{ab}^2 \mu_{ac}^2 \mu_{bc}^2 \cos(\phi_p^{ab} - \phi_p^{ac} + \phi_p^{bc})}{(-1 - \mu_{ab}^2 + \mu_{ac}^2 + \mu_{bc}^2)^2 + 4\mu_{ab}^2 \mu_{bc}^2 \mu_{ac}^2 \cos(\phi_p^{ab} - \phi_p^{ac} + \phi_p^{bc})^2} \quad (6.4)$$

These terms look very similar to what we found for the circulator except, the denominator is not necessarily greater than 1. We can then take $\phi_{tot}^{d-a} = \phi_p^{ab} - \phi_p^{ac} + \phi_p^{bc}$, and explicitly calculate the entire scattering matrix for two special values, $\phi_{tot}^{d-a} = \pm\pi/2$. For $\phi_{tot}^{d-a} = \pi/2$ we get the following

$$|s_{da}| = \begin{bmatrix} -1 + \frac{2(\mu_{bc}^2 - 1)}{-1 - \mu_{ab}^2 + \mu_{ac}^2 + \mu_{bc}^2} & \frac{2\mu_{ab} + 2\mu_{ac}\mu_{bc}}{-1 - \mu_{ab}^2 + \mu_{ac}^2 + \mu_{bc}^2} & \frac{2\mu_{ac} + 2\mu_{ab}\mu_{bc}}{-1 - \mu_{ab}^2 + \mu_{ac}^2 + \mu_{bc}^2} \\ \frac{2\mu_{ab} - 2\mu_{ac}\mu_{bc}}{-1 - \mu_{ab}^2 + \mu_{ac}^2 + \mu_{bc}^2} & -1 + \frac{2(\mu_{ac}^2 - 1)}{-1 - \mu_{ab}^2 + \mu_{ac}^2 + \mu_{bc}^2} & \frac{2\mu_{bc} - 2\mu_{ab}\mu_{ac}}{-1 - \mu_{ab}^2 + \mu_{ac}^2 + \mu_{bc}^2} \\ \frac{2\mu_{ac} - 2\mu_{ab}\mu_{bc}}{-1 - \mu_{ab}^2 + \mu_{ac}^2 + \mu_{bc}^2} & \frac{2\mu_{bc} + 2\mu_{ab}\mu_{ac}}{-1 - \mu_{ab}^2 + \mu_{ac}^2 + \mu_{bc}^2} & -1 + \frac{2(\mu_{ab}^2 - 1)}{-1 - \mu_{ab}^2 + \mu_{ac}^2 + \mu_{bc}^2} \end{bmatrix} \quad (6.5)$$

Unlike with the circulator, we cannot take all of our $\mu_{ij} \rightarrow 1$ since that will lead to nulling of the denominators due to diverging gains. Instead for the two gain processes we take $\mu_{bc}^2 = (\sqrt{G_{bc}} - 1)/(\sqrt{G_{bc}} + 1)$ and $\mu_{ac}^2 = (\sqrt{G_{ac}} - 1)/(\sqrt{G_{ac}} + 1)$ where G_{bc} is the power gain originating from the pump on mode **a** and G_{ac} is the power gain from the pump on mode **b**. Furthermore, in we assume the ideal case where the gain from the two processes are the same $G_{bc} = G_{ac} = G$. We once again assume perfect conversion and take $\mu_{ab} = 1$. This simplifies the scattering matrix to

$$|s_{da}| = \begin{bmatrix} 0 & \sqrt{G} & \sqrt{G-1} \\ 1 & 0 & 0 \\ 0 & \sqrt{G-1} & \sqrt{G} \end{bmatrix} \quad (6.6)$$

This looks a lot like a parametric amplifier, in that there are gain terms given by G and trans gain terms $G_T = \sqrt{G-1}$, but with an asymmetric flow of signals through the device and an extra port. Changing the total pump phase $\phi_{tot}^{d-a} = -\pi/2$ changes the locations of

the different scattering parameters and thus the direction of signal flow flow.

$$|s_{da}| = \begin{bmatrix} 0 & 1 & 0 \\ \sqrt{G} & 0 & \sqrt{G-1} \\ \sqrt{G-1} & 0 & \sqrt{G} \end{bmatrix} \quad (6.7)$$

Looking deeper into the asymmetry of the scattering matrix, we find ports in this device each play a unique role which we label as the Signal (S) input, Idler (I) input, and Vacuum (V) input. Signals incident on S correspond to the directional amplifier input, while signals exiting I form its output. The S port is matched (no power reflects), and incident power is instead transmitted with gain to the I and V ports. Vacuum fluctuations incident on I are responsible for the additional half-photon of added quantum noise necessarily associated with quantum-limited phase-preserving amplification. Signals incident on the V port are noiselessly and directionally transmitted through the device to the S port with unity photon gain. When $\phi_{tot}^{d-a} = \pi/2$, \mathbf{a} is mapped to V, \mathbf{b} is mapped to S, and \mathbf{c} is mapped to I. When the total pump phase is changed to $\phi_{tot}^{d-a} = -\pi/2$ the roles of \mathbf{a} and \mathbf{b} are flipped (see Fig. 6.1). The roles can also be remapped by changing with modes are connected by the conversion process. \mathbf{c} always plays the role of the idler since in this implementation it is only connected to other modes by gain processes.

This device serves as a minimal implementation of exactly the type of directional amplifier we wanted. It contains an input port (S) and an output port (I), where there signals incident on the input port are amplified at the output port, but signals incident on the output port are attenuated at the input port. A device must necessarily reflect, at a minimum, vacuum fluctuations back to the upstream signal source. In our implementation the source of these fluctuations would be provided by the cold 50 Ω load terminating the V port. Furthermore, the unity-gain transmission of signals from the V to the S port follows from the combined requirements of quantum-limited amplification.

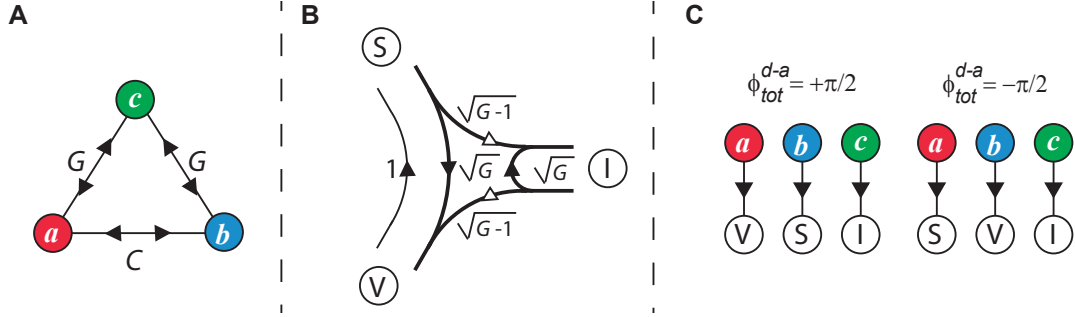


Figure 6.1: Pumping schematic and graphical scattering matrix for the Josephson directional amplifier. A) Pump configuration for the JDA: two pairs of modes are coupled pairwise via gain processes and the third via unity-gain photon conversion. B) Graphical representation of the scattering matrix: the three ports are named for the roles they perform in the amplification process. The signal (S) port serves as the directional amplifier input and is combined via phase-preserving amplification with the idler (I) port, which corresponds to the directional amplifier output. The vacuum (V) port does not participate in amplification but instead is transmitted with unity gain back to the signal port. For clarity, all zero amplitude scattering parameters are omitted. The unfilled arrows denote transmission of signals with phase conjugation. C) Map between physical ports and their roles. The pump phase and the choice of which modes are coupled via gain/conversion processes, controls how the physical ports of the JPC are mapped onto the conceptual ports of the directional amplifier. The explicit mapping for the gain and conversion couplings used in the experiment for $\phi_{tot}^{d-a} = \pi/2$ and $\phi_{tot}^{d-a} = -\pi/2$ are shown.

6.2.1 Effects of Mismatched Parametric Processes

The above analysis assumed perfectly matched gain processes and a perfect conversion process. We can easily examine the effects of mismatches by relaxing our assumptions and looking at some representative scattering parameters. If the two individual gain processes have different magnitudes but the conversion is still complete then the input match will go as

$$|s_{bb}| = \frac{\sqrt{G_{ac}} - \sqrt{G_{bc}}}{2 + \sqrt{G_{ac}} + \sqrt{G_{bc}}} \quad (6.8)$$

Gain is an intrinsically positive quantity, so combination of G_{ac} and G_{bc} will result in some degree of input match although the match will degrade as the difference between the two gains grows.

The reverse isolation will go as

$$|s_{bc}| = \frac{\sqrt{G_{ac} - 1}(1 + \sqrt{G_{bc}}) - \sqrt{G_{bc} - 1}(1 + \sqrt{G_{ac}})}{2 + \sqrt{G_{ac}} + \sqrt{G_{bc}}} \quad (6.9)$$

which, given the symmetry will still tend toward zero for $G_{ij} \gg 1$.

The forward gain will have a similar form to the reverse isolation, except with addition instead of subtraction,

$$|s_{cb}| = \frac{\sqrt{G_{ac}-1}(1+\sqrt{G_{bc}}) + \sqrt{G_{bc}-1}(1+\sqrt{G_{ac}})}{2 + \sqrt{G_{ac}} + \sqrt{G_{bc}}} \quad (6.10)$$

Thus the forward gain will stay positive for all $G_{ij} > 1$ despite the mismatch. Thus, mismatches in the two parametric gain processes will degrade performance, but will not fundamentally change the directional nature of the device.

The more interesting non-ideality arises from matching gains but imperfect conversion. If we take our two gains to be equal $G_{ac} = G_{bc} = G$, and allow our conversion to vary then the input match will go as

$$|s_{bb}| = -1 + \frac{4}{3 + \mu_{ab}^2 + \sqrt{G}(\mu_{ab}^2 - 1)} \quad (6.11)$$

If $|s_{bb}| > 1$, not only will the device not be matched, but it will exhibit reflection gain and the amplifier will fundamentally become non-directional. The requirement that $|s_{bb}| < 1$ means that $\mu_{ab} > \sqrt{\frac{-1+\sqrt{G}}{1+\sqrt{G}}}$. Translating from μ_{ab} back to the conversion coefficient C , this requires that $1 - C < 1/G$.

As with all parametric amplifiers, we need high gain in order to minimize the noise of the following HEMT. This necessitates that we have a very high conversion coefficient to maintain directionality. This is demonstrated in Fig. 6.2 where the two single-mode gains have been set to a modest value of 12 dB, and the forward gain and input match are calculated as a function of conversion coefficient. For perfect conversion $C = 1$ the directional gain matches that of the two single mode gains and the input shows a high degree of match. As the conversion coefficient begins to fall, the forward gain slowly increase and the input match rapidly degrades. Once $C < 0.95$ the input match vanishes entirely and device exhibits both forward and reflection gain. Experimentally it is relatively easy to get similar single-pump gains, but much more difficult to reach full conversion.

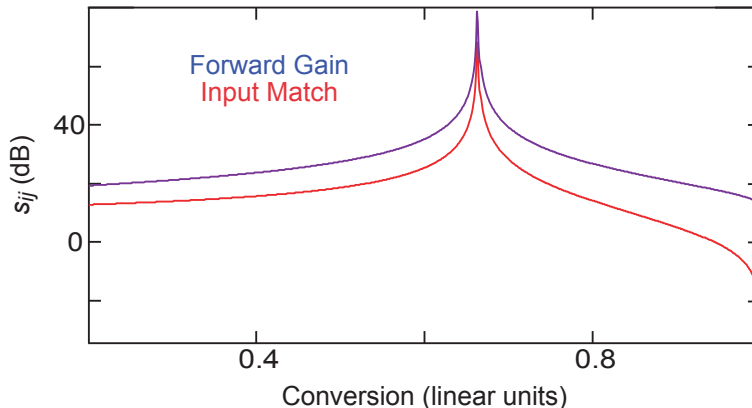


Figure 6.2: Effect of mismatched conversion in the Josephson directional amplifier (theory). Calculated scattering parameters for the forward gain s_{cb} and one of the absorptive input ports s_{bb} are plotted as a function of conversion with the two single-pump gains $G_{bc} = 12$ dB and $G_{ac} = 13$ dB. For high conversion we see the desired directional gain and input match. As the conversion falls, the match degrades, crossing a threshold at $C = 0.95$ past which there is gain on the reflected port. This degradation of directionality (despite the corresponding increase in the forward gain) demonstrates the necessity of high conversion.

6.3 Experimental Implementation and Characterization

The JPC and experimental setup are identical to the one presented for the Josephson circulator (see Fig 5.5). The only difference is in the frequency and powers of the pumps addressing the three modes. We decided to couple modes a and b via conversion, modes a and c via a gain process, and modes b and c via gain processes. Changing which modes are coupled via which type of process will just change how the physical ports map onto the conceptual ports of the directional amplifier. The biasing procedure is also very similar to that of the circulator in that we first tune up the individual single pump processes, and then fine tune the values to optimize device performance. Unlike the circulator, a particular premium is placed on approaching perfect conversion while still minimizing frequency offsets in the single pump mode responses because that ultimately sets how much directional gain we will be able to achieve. The final pump values were $\omega_c^p/2\pi = 3.927$ GHz with a power of $P_c^p = -28.95$ dBm at the generator output resulting in $C = 0.998$, $\omega_b^p/2\pi = 16.339$ GHz with $P_b^p = -11.77$ dBm resulting in $G = 13$ dB, and $\omega_a^p/2\pi = 12.412$ GHz with $P_a^p = -18.53$ dBm resulting in $G = 12$ dB. These individual parametric processes are shown superimposed in Fig. 6.3. The slight double-dip seen in s_{aa} illustrates the effect of higher order terms that

get excited via our attempts to convert as strongly as possible, and the value of the pairwise gain processes are only around 12 dB as to not overwhelm C_{ab} .

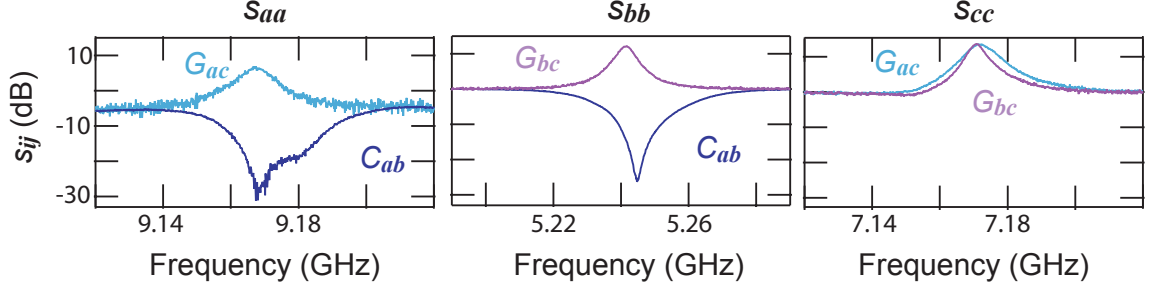


Figure 6.3: The measured pairwise conversion curves for all three processes used in the directional amplifier. The symbol G_{ij} indicates a gain process linking modes i and j , while the symbol C_{ij} indicates a conversion process linking modes i and j . For each port ($\mathbf{a} \ \mathbf{b} \ \mathbf{c}$), the pump parameters are chosen to match the conversion coefficient and center frequency for both processes involving that mode.

As with the circulator the total pump phase ϕ_{tot}^{d-a} can be swept by fixing the generator phase of two of the pump, and only sweeping the phase of the third. We calibrate the ϕ_{tot}^{d-a} to the physical generator phases by finding a point where s_{cc} is minimized. We then verify the choice of phase by adding π to the physical generator phase and verifying the frequency of maximum response for s_{cc} remains fixed. We again define $\phi_{tot}^{d-a} = \pm\pi/2$ based on the observed direction of amplification.

A measured set of scattering parameters are shown in Fig. 6.4. The probe power at the VNA output was -75 dBm, which was found to be just outside of the saturation regime. Given our pump frequency configuration, when we set $\phi_{tot}^{d-a} = -\pi/2$, mode \mathbf{a} is the signal port S, mode \mathbf{b} the vacuum port V, and mode \mathbf{c} the idler port I. The measured scattering parameters show all the hallmarks of directional amplification. First, the input port and the vacuum port both show a reflection coefficient of -16 dB or greater, indicating the device is matched. The output port I also shows the expected reflection gain. Next, signals input at S are amplified and transmitted to I and V (gain of 14 dB). Third, signals incident on I are isolated from S (with isolation of 8 dB), and are instead reflected from I and transmitted to V with gain. Finally, signals incident on V are transmitted with near unity photon gain to S ($s_{ab} = 0.2$ dB). In normal operation, port V will be terminated in a cold $50 \ \Omega$ load and can be seen as providing the necessary vacuum fluctuations which must be emitted from S.

The directional gain falls off with probe frequency as a Lorentzian line shape with a 3-dB bandwidth of 11 MHz, although other bandwidths can be defined based on the required input match or reverse isolation.

Changing the total pump phase to $\phi_{tot}^{d-a} = \pi/2$ switches the roles of mode **a** and mode **b**. This is most directly seen by comparing s_{ab} and s_{ba} , in which the direction of the gain reverses. As with the circulator, the offset between the generator phase and the total pump phase was not re-calculated between these two bias points, a phase shift of π was just added to one generator and the scattering parameters re-measured. Superimposed are the theoretical scattering parameters calculated from Eqn. 6.7 with the measured single-mode gains and conversion coefficients, as well as the measured bandwidths of the three modes taken as inputs. In general, the agreement is not as good as for the circulator which we attribute to the fact that there is now gain in the system and therefore misalignments of the pairwise processes and phase drifts can more drastically affect the amplifier performance. As with the circulator, some of the disagreement comes from imperfect mode matching in the hybrid stack. The theory also does not currently account for higher order terms. This omission is particularly important for the directional amplifier, as some effects of higher order terms can already be seen in the single-mode conversion processes. Some of the disagreement, particularly in asymmetries seen in the off-resonance scattering parameters, comes from drifts in the total pump phase. In practical implementations, interferometric techniques would be needed to stabilize ϕ_{tot}^{d-a} . This can be relatively easily implemented in future iterations, if the pump tones are generated via mixing from generators set at the frequencies of modes **a**, **b**, and **c**. Then the pump frequency relationship of the various processes ($\omega_b^p/2\pi = \omega_c^p/2\pi + \omega_a^p/2\pi$) naturally leads to the cancellation of drifts in the phase of individual generators.

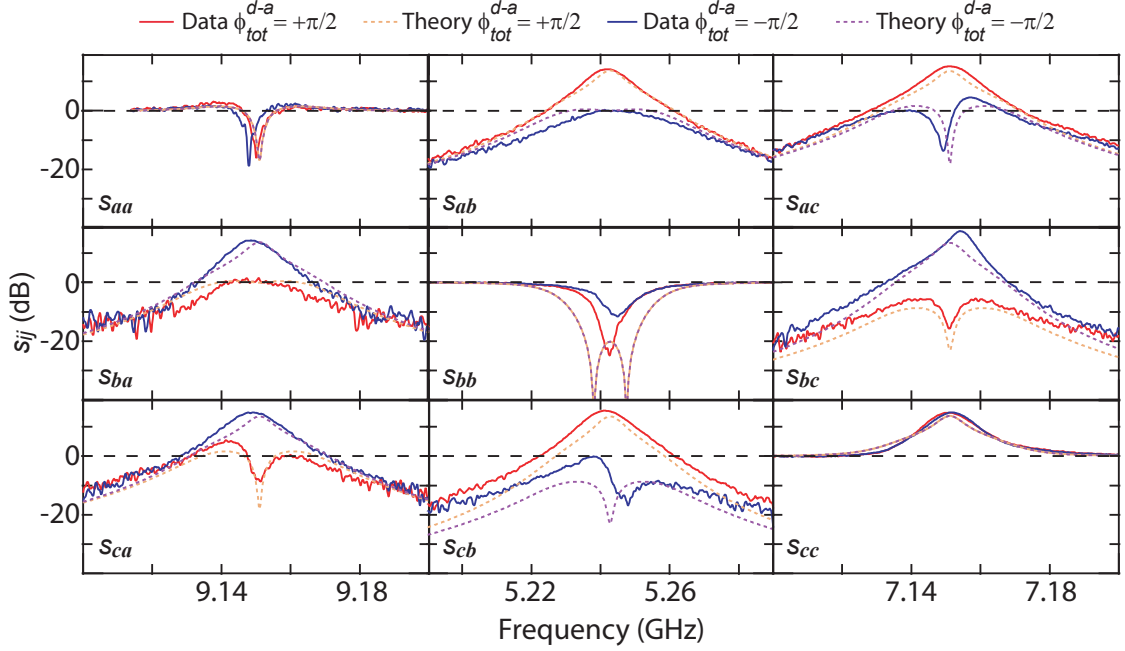


Figure 6.4: Measured Scattering parameters versus frequency for both the $\phi_{tot}^{d-a} = \pi/2$ (red) and $\phi_{tot}^{d-a} = -\pi/2$ (black) directional amplifier. Superimposed are the theoretically expected scattering parameters (dashed yellow and violet). The amplifier shows 14 dB of gain and an 11 MHz bandwidth.

6.3.1 Added Noise

To characterize the added noise of the Josephson directional amplifier we use the Noise Visibility Ratio measurement as introduced in section (DP-JBA). Fig. 6.5 shows the NVR for output of the two coupled modes of the JPC when biased with the two individual single-pump gain processes, as well as the NVR for all three modes when biased as a directional amplifier. If the JPC is biased with only one gain process, say between modes **b** and **c** then the NVR for both modes **b** and **c** show a peak corresponding to amplified quantum fluctuations from both the reflection and the trans gain. The NVR for the directional amplifier is a little more complicated. The NVR for the mode corresponding to port V should show a peak coming from the amplification between ports S and V as well as the amplification between ports I and V. Similarly, the NVR for I should also show a peak arising from both the reflected gain off port I and the forward gain between ports S and I. There are no amplification processes between V and S or between I and S, so the NVR for S should not show a peak. When $\phi_{tot}^{d-a} = \pi/2$ mode **a** acts as V, **b** acts as S and **c** acts as I

and, as expected, we see peaks in the NVR of modes **a** and **c** and no peak in the NVR or mode **b**. When $\phi_{tot}^{d-a} = -\pi/2$ the roles of **a** and **b** are exchanged, and the peak in the NVR also appears in the response of mode **b** as expected.

The relative heights NVR for the single-pump gain processes and the directional amplifier also puts a bound on the added noise of the directional amplifier. The JPC has been shown to be nearly-quantum limited [11], and the heights of the NVR for the directional amplifier agree to within 1 dB with the associated single pairwise coupling with the same gain. This indicates that the noise performance of the directional amplifier is essentially as quantum-limited as the conventional non-directional phase-preserving amplifier mode of the JPC. A better measure of the added noise, could be made by integrating the Josephson directional amplifier with a qubit. Unfortunately in the current implementation the instability of the total pump phase has prevented this measurement.

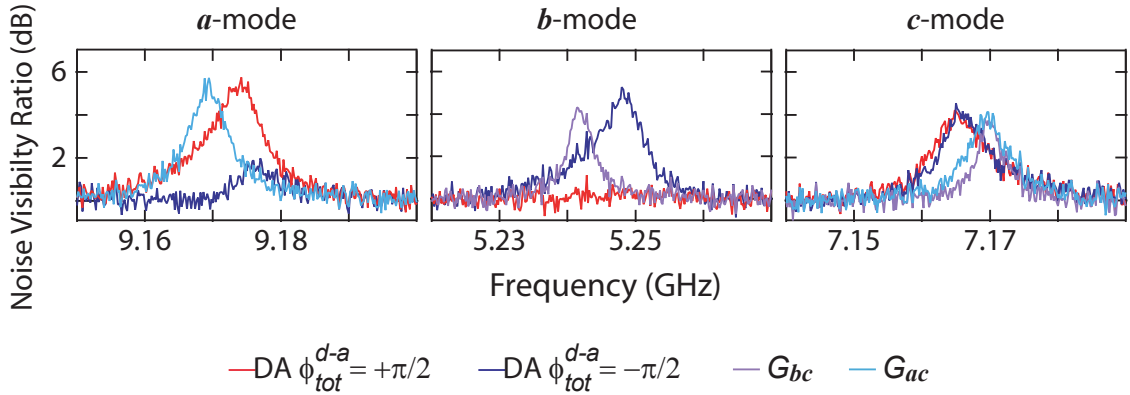


Figure 6.5: Noise visibility ratios in the Josephson directional amplifier. Noise visibility ratios for the three ports of the directional amplifier are plotted for both $\phi_{tot}^{d-a} = \pi/2$ (red) and $\phi_{tot}^{d-a} = -\pi/2$ (black). They are compared to the noise seen from the individual gain processes between modes **a** and **c** (light blue) and modes **b** and **c** (violet). The noise visibility ratios agree for all ports to within 1 dB.

6.3.2 Performance vs Conversion Coefficient

Finally, we examine the measured behavior of the device as a function of the conversion coefficient. As detailed in the theory section, the conversion process must dominate for the amplifier to be directional. The dependence of two representative scattering parameters s_{bb} and s_{ab} corresponding to input match and directional gain, respectively, are plotted in

Fig. 6.6 for selected conversion coefficients. As expected, the magnitude of all scattering parameters rises as the conversion coefficient decreases, with complete loss of input match and even reflection gain being observed once C falls below a certain threshold (here $C = 0.95$, matching the expected value described in the theory section). This threshold rises with the amplifier gain; we have chosen a directional gain of 14 dB in order to retain sufficient input match. In general, to achieve a single-stage directional amplifier with high forward gain while retaining a matched input, one requires, surprisingly, a nearly perfect converter as the key element. Although achieving higher a higher conversion coefficient was difficult due to the influence of higher order terms in the JRM, several matched, low-gain stages could also be cascaded to achieve high net gain without requiring extreme pump precision. By extending the theory to include these higher order terms, or by engineering a device in which the contributions of these terms is smaller we may also be able to realize higher directional gain.

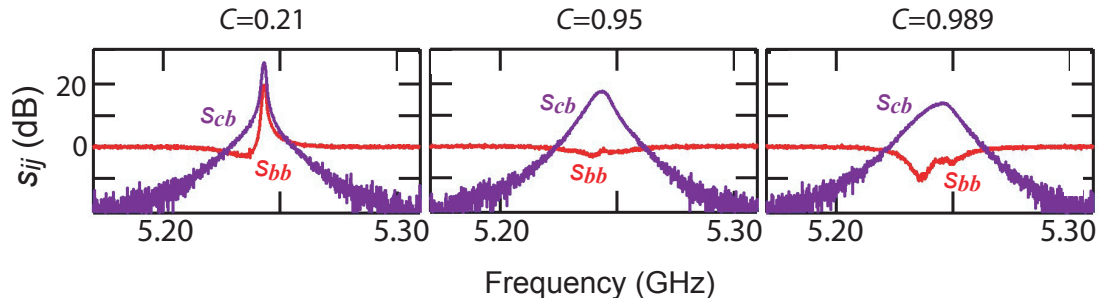


Figure 6.6: Measured scattering parameters at $C = 0.21, 0.95,$ and 0.989 . As expected, for high values of the conversion coefficient the device is directional as indicated by the dip in s_{bb} . The forward gain and input match are also plotted for the threshold of directionality $C = 0.95$, and for a point where the device exhibits both forward and reflection gain $C = 0.21$.

Chapter 7

Conclusions and Perspectives

This thesis has focused on reducing two of the primary effects limiting the manipulation of superconducting qubits by the Heisenberg back-action of measurements made with quantum-limited parametric amplifiers. Chapter 3 focused on the first effect, qubit dephasing due to excess photons in the cavity. This effect was particularly detrimental in measurements made with a Josephson bifurcation amplifier (JBA), where a large resonant pump tone is typically used to provide the energy for amplification. This chapter presented an alternative method of pumping the amplifier, which replaced the strong pump tone located at the frequency of maximum response with two pump tones which are spectrally well separated from that frequency. This greatly reduced the dephasing of the qubit due to excess photons in the cavity, and also increased the dynamic range of the amplifier. This improvement directly allowed for the observation of the Heisenberg back-action of phase-sensitive amplification using a JBA, as presented in chapter 4, and has become a standard mode of operation for experiments where this type of parametric amplifier is used to measure superconducting qubits [19,48,50,105]. Chapter 4 also presented a self-calibrated method of quantifying the second effect limiting control via Heisenberg back-action, reduced measurement efficiency.

Chapters 5 and 6 focused on ways to increase our measurement efficiency by reducing the microwave losses between the cavity and the parametric amplifier. Much of this loss is contributed by the microwave circulators, which are needed both to separate input from output in experiments using reflection parametric amplifiers, and to provide suffi-

cient reverse isolation between the reflected gain of the parametric amplifier and the cavity. Commercial circulators themselves are lossy, and they rely upon the Faraday effect in a medium under strong magnetic fields to achieve non-reciprocity. This means they must be physically isolated from the qubit and cavity, and extra cables and connectors, each with their own losses, will all further decrease the measurement efficiency. Chapter 5 presented a potentially loss-less Josephson circulator based on the Josephson parametric converter (JPC), where non-reciprocity is achieved through the interference of parametric processes instead of through the Faraday effect. Circulators could be omitted entirely if we replaced our reflection parametric amplifiers with a directional parametric amplifier. Chapter 6 presented such a amplifier, which is based on the interference of a different set of parametric processes in the same JPC. Although the gain of this device was limited by how large a conversion coefficient we were able to achieve, higher gains could easily be achieved by cascading multiple stages of amplification.

Both the Josephson circulator and directional amplifier were realized using different pumping schemes of a single standard JPC. The JPC is composed of the same materials, and fabricated using the same methods as superconducting qubits, making them fundamentally much more compatible with qubits than traditional microwave circulator and amplifiers. The JPC still does use a small magnetic field, Φ_{ext} to bias the JRM, but this could be achieved using on-chip flux bias lines, which are compatible with superconducting qubits. One extension of this work would be the integration of the qubit, cavity, and amplifier onto the same chip, which would eliminate the losses from the extra cables and connectors. There are other sources of loss which this thesis has not addressed. Other microwave components such as the normal metal hybrids used to excite the normal modes of the JPC will ultimately need to be eliminated as well.

Another important consequence of the dual nature of the Josephson circulator and directional amplifier is that the role a JPC is playing can be changed in-situ simply by changing the magnitude and frequency of the pumps applied at room temperature. This results in a flexible device, which can be used to build more complicated signal routing schemes. As an example, we believe these in-situ switchable directional elements could be the basis of a truly quantum switch matrix and gain medium, as pursued in some quantum

information architectures [106]

Although loss is the main source of measurement inefficiency, there are other sources which will ultimately need to be addressed as well. Some of our measurement inefficiency comes from temporal mismatches between the pulse leaving the cavity and the amplifier [26, 107]. Clever cavity pulse shaping will be needed to eliminate this source of inefficiency [28]. The finite internal quality factor of the resonators of these amplifiers may also become a limiting factor (as found for the silicon nitride dielectric used in the JBA [107, 108]), and may be improved from investigating new materials and fabrication procedures. By addressing all these inefficiencies, we may improve our systems enough to allow the Heisenberg back-action of measurement to be the essential tool in the manipulation of quantum information.

Bibliography

- [1] M. A. Nielsen and I. L.L. Chuang, *Quantum Computation and Quantum Information*, Cambridge University Press, 2004.
- [2] S. Haroche and J. M. Raimond, *Exploring the Quantum: Atoms, Cavities, and Photons*, Oxford University Press, 2006.
- [3] C. Cabrillo, J. I. Cirac, P. García-Fernández, and P. Zoller, *Creation of entangled states of distant atoms by interference*, Phys. Rev. A **59** (1999), 1025–1033.
- [4] C.W. Chou, H. de Riedmatten, D. Felinto, S.V. Polyakov, S.J. van Enk, and J. Kimble, *Measurement-induced entanglement for excitation stored in remote atomic ensembles*, Nature **438** (2005), 828–832.
- [5] H. A. Engel and D. Loss, *Fermionic Bell-state analyzer for spin qubits*, Science **309** (2005), 586–588.
- [6] M. Riebe, T. Monz, K. Kim, A.S. Villar, P. Schindler, M. Chwalla, Hennrich M., and R. Blatt, *Deterministic entanglement swapping with an ion-trap quantum computer*, Nature Physics **4** (2008), 839–842.
- [7] J. Kerckhoff, L. Bouten, A. Silberfarb, and H. Mabuchi, *Physical model of continuous two-qubit parity measurement in a cavity-QED network*, Phys. Rev. A **79** (2009), 024305.
- [8] W. Pfaff, H. Tim, H. Taminiau, L. Robledo, H. Bernien, M. Markham, D.J. Twitchen, and R. Hanson, *Demonstration of entanglement-by-measurement of solid-state qubits*, Nature Physics **9** (2013), 29–33.

- [9] D. Ristè, M. Dukalski, C. A. Watson, G. de Lange, M. J. Tiggelman, Ya. M. Blanter, K. W. Lehnert, R. N. Schouten, and L. DiCarlo, *Deterministic entanglement of superconducting qubits by parity measurement and feedback*, *Nature* **502** (2013), 350354.
- [10] R. Vijay, D. H. Slichter, and I. Siddiqi, *Observation of quantum jumps in a superconducting artificial atom*, *Phys. Rev. Lett.* **106** (2011), 110502.
- [11] M. Hatridge, S. Shankar, M. Mirrahimi, F. Schackert, K. Geerlings, T. Brecht, K. M. Sliwa, B. Abdo, L. Frunzio, S. M. Girvin, R. J. Schoelkopf, and M. H. Devoret, *Quantum back-action of an individual variable-strength measurement*, *Science* **339** (2013), 178.
- [12] M. Brune, E. Hagley, X. Maitre, G. Nogues, C. Wunderlich, J.M. Raimond, and S. Haroche, *Manipulating entanglement with atoms and photons in a cavity*, *Quantum Electronics Conference, 1998. IQEC 98. Technical Digest. Summaries of papers presented at the International, 1998.*
- [13] H. Mabuchi and A. C. Doherty, *Cavity quantum electrodynamics: Coherence in context*, *Science* **298** (2002), 1372–1377.
- [14] A. Blais, R. S. Huang, A. Wallraff, S. M. Girvin, and R. J. Schoelkopf, *Cavity quantum electrodynamics for superconducting electrical circuits: An architecture for quantum computation*, *Phys. Rev. A* **69** (2004), 62320.
- [15] A Wallraff, D I Schuster, A Blais, L Frunzio, R.-S. Huang, J Majer, S Kumar, S M Girvin, and R J Schoelkopf, *Strong coupling of a single photon to a superconducting qubit using circuit quantum electrodynamics*, *Nature* **431** (2004), 162–167.
- [16] J. Gambetta, A. Blais, D. I. Schuster, A. Wallraff, L. Frunzio, J. Majer, M. H. Devoret, S. M. Girvin, and R. J. Schoelkopf, *Qubit-photon interactions in a cavity: Measurement-induced dephasing and number splitting*, *Phys. Rev. A* **74** (2006), 42318.
- [17] A. P. Sears, A. Petrenko, G. Catelani, L. Sun, H. Paik, G. Kirchmair, L. Frunzio, L. I. Glazman, S. M. Girvin, and R. J. Schoelkopf, *Photon Shot Noise Dephasing in the Strong-Dispersive Limit of Circuit QED*, arXiv:1206.1265 (2012).

- [18] Carlton M Caves, *Quantum limits on noise in linear amplifiers*, Phys. Rev. D **26** (1982), 1817–1839.
- [19] K.W. Murch, S. J. Weber, C Macklin, and I Siddiqi, *Observing single quantum trajectories of a superconducting quantum bit*, Nature **502** (2013), 211–214.
- [20] P. Campagne-Ibarcq, E. Flurin, N. Roch, D. Darson, P. Morfin, M. Mirrahimi, M. H. Devoret, F. Mallet, and B. Huard, *Persistent control of a superconducting qubit by stroboscopic measurement feedback*, Phys. Rev. X **3** (2013), 021008.
- [21] S. J. Weber, A. Chantasri, J. Dressel, A. N. Jordan, K. W. Murch, and I. Siddiqi, *Mapping the optimal route between two quantum states*, Nature **511** (2014), 570–573.
- [22] C. Macklin, K. OBrien, D. Hover, M. E. Schwartz, V. Bolkhovskiy, X. Zhang, W. D. Oliver, and I. Siddiqi, *A near-quantum-limited Josephson traveling-wave parametric amplifier*, Science **350** (2015), 307–310.
- [23] N. Roch, M. E. Schwartz, F. Motzoi, C. Macklin, R. Vijay, A. W. Eddins, A. N. Korotkov, K. B. Whaley, M. Sarovar, and I. Siddiqi, *Observation of measurement-induced entanglement and quantum trajectories of remote superconducting qubits*, Phys. Rev. Lett. **112** (2014), 170501.
- [24] P. Campagne-Ibarcq, P. Six, L. Bretheau, M. Sarlette, M. Mirrahimi, P. Rouchan, and B Huard, *Observing quantum state diffusion by heterodyne detection of fluorescence*, arXiv:1511.01415 (2015).
- [25] R. Vijay, C. Macklin, D. H. Slichter, S. J. Weber, K. W. Murch, R Naik, A. N. Korotkov, and I. Siddiqi, *Quantum feedback control of a superconducting qubit: Persistent Rabi oscillations*, arXiv:1205.5591 (2012).
- [26] G. de Lange, D. Ristè, M. J. Tiggelman, C. Eichler, L. Tornberg, G. Johansson, A. Wallraff, R. N. Schouten, and L. DiCarlo, *Reversing quantum trajectories with analog feedback*, Phys. Rev. Lett. **112** (2014), 080501.

- [27] Y. Liu, S. Shankar, N. Ofek, M. Hatridge, A. Narla, K. M. Sliwa, L. Frunzio, R. J. Schoelkopf, and M. H. Devoret, *Comparing and combining measurement-based and driven-dissipative entanglement stabilization*, arXiv:1509.00860 (2015).
- [28] M. Silveri, E. Zalys-Geller, M. Hatridge, Z. Leghtas, M. H. Devoret, and S. M. Girvin, *Theory of remote entanglement via quantum-limited phase-preserving amplification*, arXiv:1507.00732 (2015).
- [29] N. Bergeal, R. Vijay, V. E. Manucharyan, I. Siddiqi, R. J. Schoelkopf, S. M. Girvin, and M. H. Devoret, *Analog information processing at the quantum limit with a Josephson ring modulator*, Nat. Phys. **6** (2010), 296–302.
- [30] N. Bergeal, F. Schackert, M. Metcalfe, R. Vijay, V. E. Manucharyan, L. Frunzio, D. E. Prober, R. J. Schoelkopf, S. M. Girvin, and M. H. Devoret, *Phase-preserving amplification near the quantum limit with a Josephson ring modulator*, Nature **465** (2010), 64–68.
- [31] N. Roch, E. Flurin, F. Nguyen, P. Morfin, P. Campagne-Ibarcq, M. H. Devoret, and B. Huard, *Widely tunable, nondegenerate three-wave mixing microwave device operating near the quantum limit*, Phys. Rev. Lett. **108** (2012), 147701.
- [32] J. D. Pillet, E. Flurin, F. Mallet, and B. Huard, *A compact design for the Josephson mixer: The lumped element circuit*, Applied Physics Letters **106** (2015).
- [33] B. Abdo, A. Kamal, and M H Devoret, *Non-degenerate, three-wave mixing with the Josephson ring modulator*, Phys. Rev. B **87** (2013), 014508.
- [34] F. Schackert, *A Practical Quantum-Limited Parametric Amplifier Based on the Josephson Ring Modulator*, Ph.D. thesis, Yale University, 2013.
- [35] B. Abdo, K. M. Sliwa, F. Schackert, N. Bergeal, M. Hatridge, L. Frunzio, D. A. Stone, and M. H. Devoret, *Full coherent frequency conversion between two propagating microwave modes*, Phys. Rev. Lett. **110** (2013), 173902.

- [36] S. Shankar, M. Hatridge, Z. Leghtas, K. M. Sliwa, A. Narla, U. Vool, S. M. Girvin, L. Frunzio, M. Mirrahimi, and M. H. Devoret, *Autonomously stabilized entanglement between two superconducting quantum bits*, Nature **504** (2013), 419–422.
- [37] U. Vool, I. M. Pop, K. Sliwa, B. Abdo, C. Wang, T. Brecht, Y. Y. Gao, S. Shankar, M. Hatridge, G. Catelani, M. Mirrahimi, L. Frunzio, R. J. Schoelkopf, L. I. Glazman, and M. H. Devoret, *Non-poissonian quantum jumps of a fluxonium qubit due to quasiparticle excitations*, Phys. Rev. Lett. **113** (2014), 247001.
- [38] P. Campagne-Ibarcq, L. Bretheau, E. Flurin, A. Auffèves, F. Mallet, and B. Huard, *Observing interferences between past and future quantum states in resonance fluorescence*, Phys. Rev. Lett. **112** (2014), 180402.
- [39] Z. Leghtas, S. Touzard, I. M. Pop, A. Kou, B. Vlastakis, A. Petrenko, K. M. Sliwa, A. Narla, M. Hatridge, M. Reagor, L. Frunzio, R. J. Schoelkopf, M. Mirrahimi, and M. H. Devoret, *Confining the state of light to a quantum manifold by engineered two-photon loss*, Science **347** (2015), 853–857.
- [40] M. Reagor, W. Pfaff, C. Axline, R. W. Heeres, N. Ofek, K. M. Sliwa, E. Holland, C. Wang, J. Blumoff, C. Chou, M. Hatridge, L. Frunzio, M. H. Devoret, L. Jiang, and R. J. Schoelkopf, *A quantum memory with near millisecond coherence in circuit QED*, arXiv:1508.05882 (2015).
- [41] Z.K. Mineev, K. Serniak, I. M. Pop, Z. Leghtas, K. M. Sliwa, M. Hatridge, L. Frunzio, R. J. Schoelkopf, and M.H. Devoret, *2.5d circuit quantum electrodynamics*, arXiv:1509.01619 (2015).
- [42] C. Wang, G. Y. Yvonne, P. Reinhold, R. W. Heeres, N. Ofek, C. Chou, C. Axline, M. Reagor, J. Blumoff, K. M. Sliwa, L. Frunzio, S. M. Girvin, L. Jiang, M. Mirrahimi, M. H. Devoret, and R. J. Schoelkopf, *A Schrödinger cat living in two boxes*, Manuscript in preparation (2016).
- [43] R. Vijay, *Josephson Bifurcation Amplifier: Amplifying Quantum Signals Using a Dynamical Bifurcation*, Ph.D. thesis, Yale University, 2008.

- [44] D Ristè, C C Bultink, K W Lehnert, and L DiCarlo, *Feedback control of a solid-State qubit using high-fidelity projective measurement*, Phys. Rev. Lett. **109** (2012), 240502.
- [45] K. W. Murch, U. Vool, D. Zhou, S. J. Weber, S. M. Girvin, and I. Siddiqi, *Cavity-assisted quantum bath engineering*, Phys. Rev. Lett. **109** (2012), 183602.
- [46] D Ristè, J G van Leeuwen, H.-S. Ku, K W Lehnert, and L DiCarlo, *Initialization by measurement of a superconducting quantum bit circuit*, Phys. Rev. Lett. **109** (2012), 50507.
- [47] D. Ristè, C. C. Bultink, M. J. Tiggelman, R. N. Schouten, K. W. Lehnert, and L. DiCarlo, *Millisecond charge-parity fluctuations and induced decoherence in a superconducting transmon qubit*, Nat. Commun. **4** (2013), 1913.
- [48] L. Sun, A. Petrenko, Z. Leghtas, Z. Leghtas, G. Kirchmair, K. M. Sliwa, A. Narla, M. Hatridge, S. Shankar, J. Blumoff, L. Frunzio, M. Mirrahimi, M. H. Devoret, and R. J. Schoelkopf, *Tracking photon jumps with repeated quantum non-demolition parity measurements*, Nature **511** (2014), 444–448.
- [49] W.F. Kindel, M.D. Schroer, and K. W. Lehnert, *Generation and efficient measurement of single photons from fixed frequency superconducting qubits*, arXiv:1510.00663 (2015).
- [50] B. Vlastakis, A. Petrenko, N. Ofek, L. Sun, K. M. Sliwa, M. Hatridge, J. Blumoff, L. Frunzio, M. Mirrahimi, L. Jiang, M. H. Devoret, and R. J. Schoelkopf, *Violating Bell's inequality with an artificial atom and a cat state in a cavity*, Manuscript in preparation.
- [51] J.D. Teufel, T. Donner, M. A. Castellanos-Beltran, J.W. Harlow, and K. W. Lehnert, *Nanomechanical motion measured with an imprecision below that at the standard quantum limit*, Nature nanotechnology **4** (2009), 820–823.
- [52] J.D. Teufel, T. Donner, D. Li, J.W. Harlow, M.S. Allman, K. Cicak, A.J. Sirois, J.D. Whittaker, K.W. Lehnert, and R.W. Simmonds, *Sideband cooling of micromechanical motion to the quantum ground state*, Nature **475** (2011), 359–363.

- [53] M Hatridge, R Vijay, D H Slichter, John Clarke, and I Siddiqi, *Dispersive magnetometry with a quantum limited SQUID parametric amplifier*, Phys. Rev. B **83** (2011), 134501.
- [54] N. Antler, E. M. Levenson-Falk, R. Naik, Y.-D. Sun, A. Narla, R. Vijay, and I. Siddiqi, *In-plane magnetic field tolerance of a dispersive aluminum nanobridge SQUID magnetometer*, Applied Physics Letters **102** (2013), 232602.
- [55] E. M. Levenson-Falk, R. Vijay, N. Antler, and I. Siddiqi, *A dispersive nanoSQUID magnetometer for ultra-low noise, high bandwidth flux detection*, Superconductor Science and Technology **26** (2013), 055015.
- [56] A. Kamal, A. Roy, J. Clarke, and M. H. Devoret, *Asymmetric frequency conversion in nonlinear systems driven by a biharmonic pump*, Phys. Rev. Lett. **113** (2014), 247003.
- [57] L. Ranzani and J. Aumentado, *Graph-based analysis of nonreciprocity in coupled-mode systems*, New Journal of Physics **17** (2015), 023024.
- [58] K. M. Sliwa, M. Hatridge, A. Narla, S. Shankar, L. Frunzio, R. J. Schoelkopf, and M. H. Devoret, *Reconfigurable Josephson circulator/directional amplifier*, Phys. Rev. X **5** (2015), 041020.
- [59] L. Spietz, K. Irwin, and J. Aumentado, *Input impedance and gain of a gigahertz amplifier using a dc superconducting quantum interference device in a quarter wave resonator*, Applied Physics Letters **93** (2008), 082506.
- [60] M. Mück and R. McDermott, *Radio-frequency amplifiers based on dc SQUIDs*, Supercond. Sci. Technol. **23** (2010), 93001.
- [61] D. Kinion and J. Clarke, *Superconducting quantum interference device as a near-quantum-limited amplifier for the axion dark-matter experiment*, Applied Physics Letters **98** (2011), 202503.
- [62] G. J. Ribeill, D. Hover, Y.-F. Chen, S. Zhu, and R. McDermott, *Superconducting low-inductance undulatory galvanometer microwave amplifier: Theory*, Journal of Applied Physics **110** (2011), 103901.

- [63] D. Hover, Y.-F. Chen, G. J. Ribeill, S. Zhu, S. Sendelbach, and R. McDermott, *Superconducting low-inductance undulatory galvanometer microwave amplifier*, Applied Physics Letters **100** (2012), 063503.
- [64] B. Yurke, M. L. Roukes, R. Movshovich, and A. N. Pargellis, *A low-noise series-array Josephson junction parametric amplifier*, Applied Physics Letters **69** (1996), 3078–3080.
- [65] H.E. Byeong, P. K. Day, H. G. LeDuc, and J. Zmuidzinas, *A wideband, low-noise superconducting amplifier with high dynamic range*, Nature Physics **8** (2012), 623–627.
- [66] C. Bockstiegel, J. Gao, M. R. Vissers, M. Sandberg, S. Chaudhuri, A. Sanders, L. R. Vale, K. D. Irwin, and D. P. Pappas, *Development of a broadband NbTiN traveling wave parametric amplifier for MKID readout*, Journal of Low Temperature Physics **176** (2014), 476–482.
- [67] K. O'Brien, C. Macklin, I. Siddiqi, and X. Zhang, *Resonant phase matching of josephson junction traveling wave parametric amplifiers*, Phys. Rev. Lett. **113** (2014), 157001.
- [68] T.C. White, M.T. Mutus, I.C. Hoi, R. Barends, B. Campbell, Yu Chen, Z. Chen, B. Chairo, A. Dunsworth, E. Jeffery, J. Kelly, A. Megrant, C. Neill, P.J.J. O'Malley, P. Rouchan, D. Sank, Vainsencher A., J. Wenner, S. Chaudhuri, J. Gao, and J. M. Martinis, *Traveling wave parametric amplifier with Josephson junction using minimal resonator phase matching*, arXiv:1503.04364 (2015).
- [69] B. Abdo, K. M. Sliwa, S. Shankar, M. Hatridge, L. Frunzio, R. Schoelkopf, and M. H. Devoret, *Josephson directional amplifier for quantum measurement of superconducting circuits*, Phys. Rev. Lett. **112** (2014), 167701.
- [70] S. K. Choi, R. D. Li, C. Kim, and P. Kumar, *Traveling-wave optical parametric amplifier: investigation of its phase-sensitive and phase-insensitive gain response*, J. Opt. Soc. Am. B **14** (1997), 1564–1575.

- [71] V. M. Eguíluz, M. Ospeck, Y. Choe, A. J. Hudspeth, and M. O. Magnasco, *Essential nonlinearities in hearing*, Phys. Rev. Lett. **84** (2000), 5232–5235.
- [72] J. Kakande, C. Lundström, P. A. Andrekson, Z. Tong, M. Karlsson, P. Petropoulos, F. Parmigiani, and D. J. Richardson, *Detailed characterization of a fiber-optic parametric amplifier in phase-sensitive and phase-insensitive operation*, Opt. Express **18** (2010), 4130–4137.
- [73] R. Vijay, M. H. Devoret, and I. Siddiqi, *Invited review article: The Josephson bifurcation amplifier*, Review of Scientific Instruments **80** (2009), 111101.
- [74] T. Yamamoto, K. Inomata, M. Watanabe, K. Matsuba, T. Miyazaki, W. D. Oliver, Y. Nakamura, and J. S. Tsai, *Flux-driven Josephson parametric amplifier*, Applied Physics Letters **93** (2008), 042510.
- [75] M. H. Devoret and A. Roy, *Introduction to quantum-limited parametric amplification of quantum signals with Josephson circuits*, Manuscript in preparation (2015).
- [76] M. A. Castellanos-Beltran, K. D. Irwin, G. C. Hilton, L. R. Vale, and K. W. Lehnert, *Amplification and squeezing of quantum noise with a tunable Josephson metamaterial*, Nat. Phys. **4** (2008), 929–931.
- [77] J. Y. Mutus, T. C. White, E. Jeffrey, D. Sank, R. Barends, J. Bochmann, Yu Chen, Z. Chen, B. Chiaro, A. Dunsworth, J. Kelly, A. Megrant, C. Neill, P. J. J. O’Malley, P. Roushan, A. Vainsencher, J. Wenner, I. Siddiqi, R. Vijay, A. N. Cleland, and John M. Martinis, *Design and characterization of a lumped element single-ended superconducting microwave parametric amplifier with on-chip flux bias line*, Applied Physics Letters **103** (2013), 122602.
- [78] C. M. Wilson, G. Johansson, A. Pourkabirian, Simoen M., J. R. Johansson, Duty T., Nori F., and R. Delsing, *Observation of the dynamical Casimir effect in a superconducting circuit*, Nature **479** (2011), 376–379.

- [79] X. Zhou, V. Schmitt, P. Bertet, D. Vion, W. Wustmann, V. Shumeiko, and D. Esteve, *High-gain weakly nonlinear flux-modulated Josephson parametric amplifier using a SQUID array*, Phys. Rev. B **89** (2014), 214517.
- [80] S. Mallet, *A Wavelet Tour of Signal Processing*, Academic Press, 1999.
- [81] E. Flurin, *The Josephson Mixer: A Swiss Army Knife for Microwave Quantum Optics*, Ph.D. thesis, Ecole Normale Supérieure, 2014.
- [82] C. Gardiner and P. Zoller, *Quantum Noise*, Springer, 2004.
- [83] M. A. Castellanos-Beltrán, *Development of a Josephson Parametric Amplifier for the Preparation and Detection of Nonclassical States of Microwave Fields*, Ph.D. thesis, University of Colorado, 2010.
- [84] F. Schackert, A. Roy, M. Hatridge, M. H. Devoret, and D. A. Stone, *Three-wave mixing with three incoming waves: signal-idler coherent attenuation and gain enhancement in a parametric amplifier*, Phys. Rev. Lett. **111** (2013), 073903.
- [85] J. Koch, T. M. Yu, J. Gambetta, A. A. Houck, D. I. Schuster, J. Majer, A. Blais, M. H. Devoret, S. M. Girvin, and R. J. Schoelkopf, *Charge-insensitive qubit design derived from the Cooper pair box*, Phys. Rev. A **76** (2007), 42319.
- [86] H. Paik, D. I. Schuster, L. S. Bishop, G. Kirchmair, G. Catelani, A. P. Sears, B. R. Johnson, M. J. Reagor, L. Frunzio, L. I. Glazman, S. M. Girvin, M. H. Devoret, and R. J. Schoelkopf, *Observation of high coherence in Josephson junction qubits measured in a three-dimensional circuit QED architecture*, Phys. Rev. Lett. **107** (2011), 240501.
- [87] Rusko Ruskov and Alexander N. Korotkov, *Entanglement of solid-state qubits by measurement*, Phys. Rev. B **67** (2003), 241305.
- [88] S. Barnett and P. Radmore, *Methods in Theoretical Quantum Optics*, Oxford University Press, 2002.
- [89] E. Flurin, N. Roch, F. Mallet, M. H. Devoret, and B. Huard, *Generating entangled microwave radiation over two transmission lines*, Phys. Rev. Lett. **109** (2012), 183901.

- [90] A. Narla, K. M. Sliwa, M. Hatridge, S. Shankar, L. Frunzio, R. J. Schoelkopf, and M. H. Devoret, *Wireless josephson amplifier*, Applied Physics Letters **104** (2014), 232605.
- [91] D. M. Pozar, *Microwave engineering, 3rd ed.*, John Wiley & Sons, 2005.
- [92] Pamtech Inc., *Cryogenic components*. <http://pamtechinc.com/cryogenic-components/>, January 2015.
- [93] A. Kamal, J. Clarke, and M. H. Devoret, *Noiseless nonreciprocity in a parametric active device*, Nat. Phys. **7** (2010), 17.
- [94] B. Abdo, K M. Sliwa, A. Kamal, F Schackert, M Hatridge, L Frunzio, and M H Devoret, *Measurement of the phase non-reciprocity of the Josephson parametric converter*, Bulletin of the American Physical Society, 2012.
- [95] A. Metelmann and A. A. Clerk, *Nonreciprocal photon transmission and amplification via reservoir engineering*, Phys. Rev. X **5** (2015), 021025.
- [96] K. Kerckhoff, J. and Lalumière, B. J. Chapman, A. Blais, and K. W. Lehnert, *On-chip superconducting microwave circulator from synthetic rotation*, Phys. Rev. Applied **4** (2015), 034002.
- [97] J. Koch, A A Houck, K.L. Hur, and S M Girvin, *Time-reversal-symmetry breaking in circuit-QED-based photon lattices*, Phys. Rev. A **82** (2010), 043811.
- [98] G. J. Dolan, *Offset masks for lift-off photoprocessing*, Applied Physics Letters **31** (1977), 337–339.
- [99] Archana Kamal, John Clarke, and Michel H. Devoret, *Gain, directionality, and noise in microwave SQUID amplifiers: Input-output approach*, Phys. Rev. B **86** (2012), 144510.
- [100] J. E. Johnson, E. M. Hoskinson, C. MacKlin, D. H. Slichter, I. Siddiqi, and John Clarke, *Dispersive readout of a flux qubit at the single-photon level*, Phys. Rev. B **84** (2011), 220503.

- [101] D. Hover, S. Zhu, T. Thorbeck, G. J. Ribeill, D. Sank, J. Kelly, R. Barends, John M. Martinis, and R. McDermott, *High fidelity qubit readout with the superconducting low-inductance undulatory galvanometer microwave amplifier*, Appl. Phys. Lett. **104** (2014), 152601.
- [102] J. Hansryd and Peter A. Andrekson, *Fiber-based optical parametric amplifiers and their applications*, IEEE Journal of Selected Topics in Quantum Electronics **8** (2002), 506–520.
- [103] A. Kamal, *”nonreciprocity in active josephson junction circuits”*, Ph.D. thesis, Yale University, 2013.
- [104] A. Metelmann and A. A. Clerk, *Quantum-limited amplification via reservoir engineering*, Phys. Rev. Lett. **112** (2014), 133904.
- [105] K. Murch, S. J. Weber, K.M. Beck, E. Ginossar, and I Siddiqi, *Reduction of the radiative decay of atomic coherence in squeezed vacuum*, Nature **499** (2013), 62–65.
- [106] D Hucul, I. V. Inlek, G. Vittorini, C. Crocker, S. Debnath, S. M. Clarke, and C. Monroe, *Modular entanglement of atomic qubits using photons and phonons*, Nature Physics **11** (2015), 37.
- [107] S. J. Weber, *Quantum Trajectories of a Superconductin Qubit*, Ph.D. thesis, University of California Berkeley, 2014.
- [108] E. M. Levenson-Falk, R. Vijay, and I. Siddiqi, *Nonlinear microwave response of aluminum weak-link Josephson oscillators*, Applied Physics Letters **98** (2011), 123115.